University of Nevada, Reno

Understanding the Tribocorrosion Behavior of Engineered Surfaces

A dissertation submitted in partial fulfillment of
the requirements for the degree of
Doctor of Philosophy in Mechanical Engineering

by

Arpith Siddaiah

Dr. Pradeep Menezes / Dissertation Advisor

August 2020

N

We recommend that the dissertation
prepared under our supervision by

Arpith Siddaiah

entitled

Understanding the Tribocorrosion Behavior of Engineered Surfaces

be accepted in partial fulfillment of the
requirements for the degree of

Doctor of Philosophy

Dr. Pradeep Menezes
Advisor

Dr. Yiliang Liao
Committee Member

Dr. Bin Li
Committee Member

Dr. Guoping Xiong
Committee Member

Dr. Rahul Ramachandran
Committee Member

Prof. Manoranjan Misra
Graduate School Representative

David W. Zeh, Ph.D., Dean
Graduate School

August, 2020

Abstract

Wear and corrosion are the most common forms of degradation in automobiles, ships, aircraft, biomedical implants, industrial machinery, and other mechanical systems. The dependence of these mechanical systems on tribological contacts accounts for a global economic wear loss of US$300 billion USD (2017) annually. The losses from fiction and wear are estimated to be 73% and 27%, respectively. Additionally, the global cost of corrosion is estimated to be US$2,505 billion, which is equivalent to 3.4% of the global Gross Domestic Product (GDP 2013). Today, with advanced manufacturing and surface processing techniques, it is possible to render a surface functionally resistant to wear or corrosion. A major drawback of such functionalization is that the processing specifically enhances resistance to either wear or corrosion, however, the action of wear and corrosion can lead to a wear-corrosion synergistic degradation, which has been scarcely understood. When functional surfaces are in relative sliding motion in a lubricated environment, they undergo wear and corrosion over extended periods of operation. The oxide layer formed as a result of corrosion is mechanically removed during sliding, thereby exposing a fresh layer of metal to degrade by wear and corrosion. The cycle of synergism between wear and corrosion is called tribocorrosion. The onset of tribocorrosion causes material degradation to occur faster than the action of either wear or corrosion alone. Understanding and characterizing the mechanism of tribocorrosion in various mechanical systems is complicated due to the variability in surface characteristics, lubricants, and tribo-interface conditions. This has also made it challenging to develop a stable wear-corrosion synergism monitoring system and tribocorrosion resistant surfaces for oil and aqueous environments.

In the present study, an experimental module to monitor tribocorrosion *in-situ* is designed and implemented to measure the tribocorrosion behavior of various surface characteristics, lubricants, and tribo-interface conditions. A focus is placed on understanding the mechanism of tribocorrosion and designing surfaces with enhanced tribocorrosion resistance. The effect of surface engineering methods, such as textures and coatings on tribocorrosion, are investigated. More specifically, the surface engineering methods include surface processing using laser shock peening (LSP) on steel and magnesium alloys, and nanocomposite coatings on surfaces using Nickel-Graphene. The environmental conditions include aqueous environments that simulate seawater conditions. The study investigates the mechanochemical and physicochemical behavior of surface characteristics after modification to understand the mechanism of tribocorrosion. The effect of LSP intensity on

wear, corrosion, tribocorrosion, surface roughness, and surface energy is discussed, and phenomenological models are proposed. The observed correlation between surface roughness, surface energy, and wear-corrosion synergism in defining the tribocorrosion mechanism is also discussed.

This study has enabled (1) understanding of the association between electrochemical and mechanical processes that affect the material and lubricant degradation, (2) application of innovative solutions to mitigate tribocorrosion in advanced manufacturing and material processing applications, and (3) design of material systems that are resistant to tribocorrosion. The study on the tribological behavior of LSP surfaces shows the coefficient of friction (COF) can be reduced by up to 83.25% depending on the applied laser intensity. From the results of this study, it was inferred that the surface roughening effects induced by the laser intensity plays a major role in defining the tribocorrosion behavior of LSP surfaces. The tribocorrosion studies that followed indicate that a change in surface roughness can drastically modify the wettability of the surface, more so in environments susceptible to corrosion. The wettability can be quantified into various components of surface energy. The surface energy was found to be the lowest at lower laser intensities. Lower interfacial surface energy showed decreased wettability, providing enhanced tribocorrosion resistance. However, higher laser intensities increased the surface roughening effect, causing an increase in the interfacial surface energy and wettability of the surfaces, and thereby decreasing the tribocorrosion resistance. Depending on the applied laser intensity, the surface roughness and the profile of the treated area can be precisely controlled, thereby providing a technique to tailor not just tribological properties, but also the tribocorrosion properties.

Tribocorrosion studies have also been conducted for electrodeposited nickel-graphene (Ni/GPL) nanocomposite films on steel to understand the wear accelerated corrosion in contaminated oil-lubricated mediums. It was observed that the wear-corrosion synergism for steel with and without the Ni/GPL film was negligible in an uncontaminated oil (synthetic transmission oil). However, when the oil was contaminated, the wear-corrosion synergy was higher on steel than on steel with Ni/GPL. The enhanced resistance to wear corrosion synergy was attributed to the Ni/GPL having refined grains that results in minimal transport of corrosive contaminants, water, and oxygen that inhibits corrosion cracking or pitting to the substrate. Further, the presence of GPL in the film minimized the effects of wear, which resulted in enhanced resistance of Ni/GPL films to tribocorrosion. This study provides insight into the role of surface characteristics,

lubricants, and tribo-interface conditions that define the synergism between wear and corrosion. The research will enable the effective utilization and design of a tribo-system that can maximize the tribological performance and inhibit tribocorrosion.

Dedication

To my mother, father, and gurus for their motivation to face all challenges head on and go through them.

To my brother and friends for always showing me the good things in life.

Acknowledgements

As I finish writing my dissertation, I reminisce on the five years I have spent at University of Nevada-Reno. These years have been more of a dream that has brought me the pleasure of meeting my advisor Dr. Pradeep Menezes who has guided and helped shape my professional career, mentors, friends who have been more of a family to me here 8000 miles from home. Most of all I am grateful to be at UNR that has stimulated my interests in every way, refresh my mind, and inspire wonderful ideas in my research. The completion of my thesis is accompanied with enormous help from all of them and huge motivation from my family.

I would like to first express my sincere gratitude, deepest respect and special thanks to my supervisor and advisor, Dr. Pradeep Menezes, for providing me the opportunity to conduct this research. His generous support, patient tutoring, and sustaining encouragement, has this dissertation possible and help me grow enormously. In addition to being a creative and insightful researcher, Dr. Menezes is also an excellent advisor and friend with whom I have shared so much joy of research. He has helped me gain an enormous depth of patience, knowledge, and character. I am grateful to know him and complete my doctoral degree under his guidance.

My sincere thanks also go to Dr. Yiliang Liao, for all the constructive discussion and guidance in research. His expert guidance and honest critics during our collaborative research helped me develop valuable knowledge and insight required to conduct good research. Dr. Liao's consistent guidance and motivation has always helped me accelerate my work efficiency and be productive. I would also like to thank Dr. Rahul Ramachandran for his support and guidance, from whom I have been able to learn troubleshooting, electrochemical experiments, and related theoretical work to name a few. My thanks also go to Dr. Bin Li, Dr. Guoping Xiong and Prof. Manoranjan Misra, for constant support and severing as my PhD committee members. I thank them for their valuable inputs and their good-natured support.

I would like to express my gratitude to all the group members at the Surface Engineering Tribology lab, and Composited & Additive Manufacturing lab – Ashish Kasar, Arjun Manoj, Allessandro Ralls, Soumya Sikdar, and Zach Montte, for the friendship and their help over the past five years. I would like to thank Mr. Tony Berendsen and Mr. Brain Nagy for their expertise and efforts in helping me with specimen machining work and lots of good times. I would like to give my deepest thanks to Bo Mao, Dr. Zac Karmiol, Dr. Joel DesOrmeau for his kindness of supporting me on many characterization and collaborative work.

Finally, my utmost acknowledgement goes to my beloved parents and brother. I owe enormous debts of gratitude to their sustainable support and encouragement. Their love and sacrifice deserve far more than what I can return. Thank you for being there for me.

TABLE OF CONTENTS

List of Tables

List to Figures

Chapter 1: Introduction

The field of tribocorrosion is the integration of tribology (the science of friction, lubrication, and wear) and corrosion (resulting from physiochemical interactions between materials and their environments), two significant areas of degradation in mechanical systems. The interaction between wear and corrosion in an aqueous environment can produce a synergistic effect that can degrade materials at a faster rate than wear or corrosion alone [1-3]. Wear can occur due to two-body or three-body contacts between sliding pairs. When corrosion initiates simultaneously with wear, a synergistic degradation process that involves wear accelerated corrosion or corrosion-accelerated wear begins. The primary wear mechanism for sliding metal pairs is oxidative wear in which the passive oxide film is mechanically removed when two surfaces are in mechanical sliding contact. The freshly exposed layer undergoes further oxidation, and the cycle continues. This mechanism of material and lubricant degradation is referred to as wear-corrosion synergism, or tribocorrosion.

Literature indicates that the mechanism of tribocorrosion has been well investigated for biomedical applications, such as dental and bone implants, micro-electro-mechanical systems (MEMS), and marine applications where the tribo-systems are exposed to electrochemically active environments. However, with the advent of new functional surfaces, materials, and lubricants for multifunctional mechanical applications, it has become a challenge to understand the mechanism of tribocorrosion in these systems. This is especially the case when most of the studies concerning tribocorrosion focus on understanding the role of surface characteristics or lubricant performance without considering the entire tribocorrosion system. The present study aims to investigate the various aspects of tribocorrosion, which include surface characteristics, lubricating medium, and tribo-interface conditions. An outline of the present study has been schematically presented in *Figure 1.1*. This study will provide a fundamental understanding of the tribocorrosion behavior of functional surfaces (surfaces processed using LSP and electrodeposition) under known lubricated/aqueous environments and tribo-interface conditions. The current section introduces various aspects related to the present study.
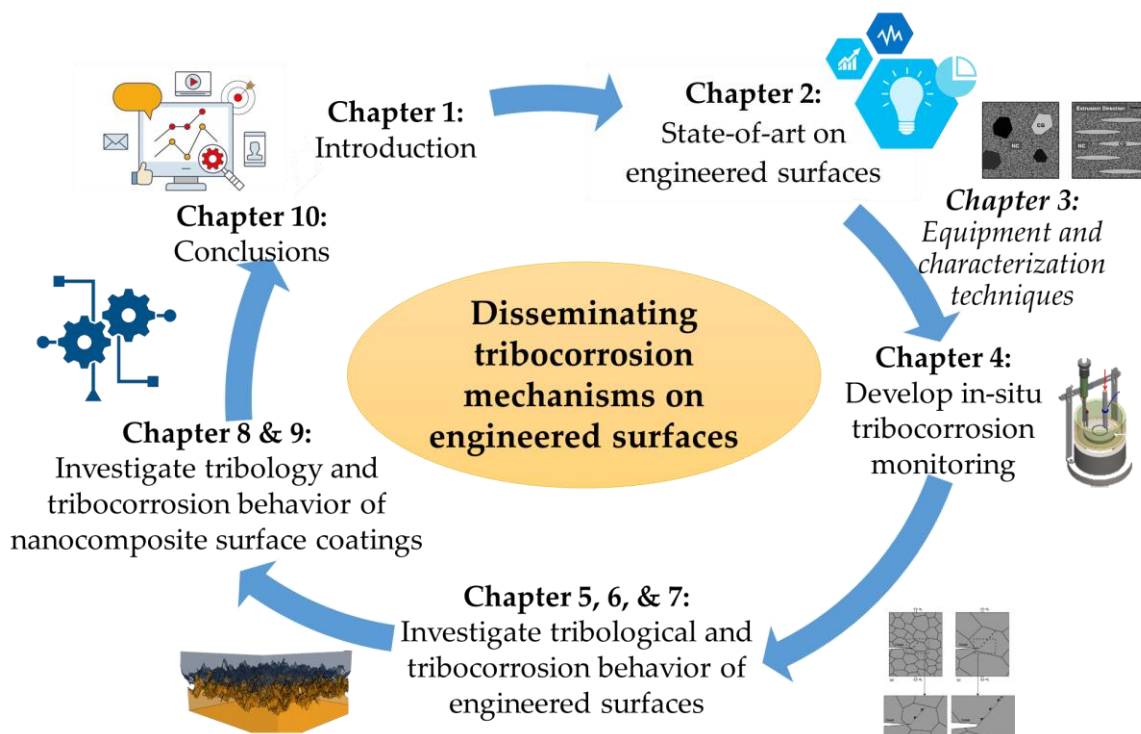
Figure 1.1: Schematic break down of the present study

1.1. Measurement and analysis of tribocorrosion

Degradation of a metallic surface in tribo-contact is a consequence of foreign contaminants introduced in the lubricant medium over its functioning period. Most of these contaminants are introduced to the lubricant through wear debris generated by one or more tribo-pairs in contact within the lubricant along with other process by-products such as water and soot [4-7]. The extent of degradation occurring is defined by the tribo-pair surface characteristic, lubricant, and tribo-interface conditions. As the contaminants enter the lubricant, they directly accelerate, or in many cases, exponentially accelerate the degradation process due to corrosion and reduced effectiveness of boundary lubrication [8-10]. The degradation process of material surfaces and lubricants within an enclosed mechanical system can be found to be directly correlated to the extent of tribocorrosion. Even though the degradation rate of a surface and lubricant can be predicted by monitoring the 'by-product effects' of tribocorrosion such as – lubricant temperature, cycle time, pressure, elapsed time since last lube change, and other such parameters, it is still not accurate enough to provide the actual effects of contaminants due to tribocorrosion [11, 12].

Today, the overall degradation of the material surface and lubricant are electronically monitored using the 'by-product effect' data. These estimations are complex and unreliable in many cases [13-19]. The latest developments in data processing and modeling techniques include elaborate and complex corrosion predictive models that enable efficient corrosive species detection [20-22]. A wide range of corrosion species such as pitting corrosion, crevice corrosion, stress corrosion cracking, and general forms of chemical-induced corrosion can be detected using these models. However, these models need to have an effective detection system that can provide in-situ data acquisition that is more accurate than those of sensor-based systems. Several commercial and scientific testing methods are also widely used for the same purpose, but most of these techniques are ex-situ and time intensive. Some of the sensors and sampling test methods in relation to their lubricant degradation features are shown in *Figure 1.2* [23].
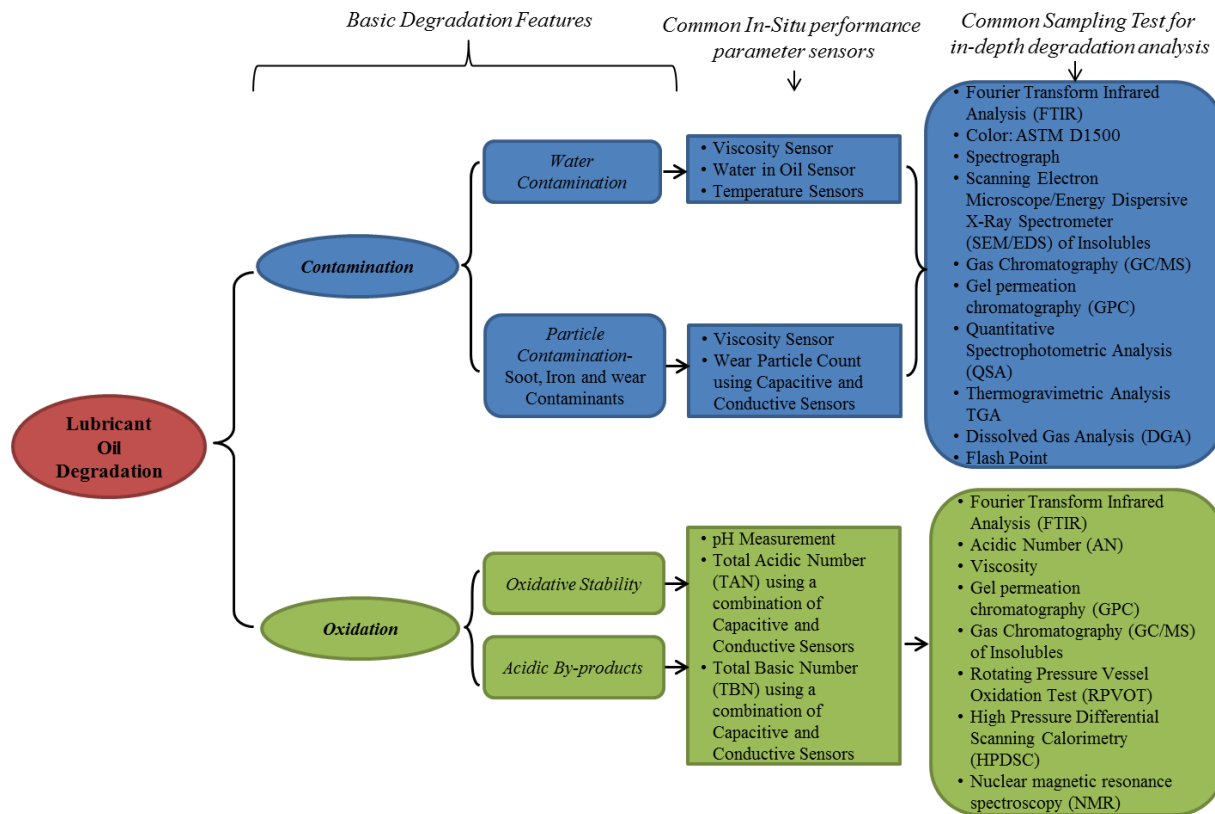
Figure 1.2: Lubricant degradation features and their common in-situ and sampling methods of testing

The technological gaps to be addressed in lubricant monitoring systems is to accurately and continuously monitor the *origins* of lubricant degradation that are due to wear and corrosion. If a monitoring system can monitor the wear rate of the tribo-pairs in contact along with the corrosion

rate in the lubricant arising due to the contaminants, this system can be expected to be more reliable than the multitude of electronic-based lubricant monitoring systems. This system can be further integrated with the latest corrosion and wear analysis models to provide condition-based predictive and prognostic outputs.

The standard procedure for determining the synergism between wear and corrosion was developed by Madsen [24]. It can be understood from the experimental techniques used to study tribocorrosion that the real contact area, also known as the active wear track area, is an essential factor in defining the wear-corrosion synergism [25-27]. There have been innovative approaches to determine the active wear track and understand the wear-corrosion synergy. Garcia et al. [28] calculated the active wear track area by assuming the occurrence of a depassivation - repassivation event between two successive contact events. Landolt et al. [26] developed a model to understand the effect of normal force on wear-accelerated corrosion. Vieira et al. [29] developed a galvanic cell model for tribocorrosion at open circuit potential (OCP). This galvanic cell approach provided a new perspective on the corrosion observed within a tribocorrosion system. It was shown that galvanic coupling could occur between mechanically depassivated areas (anode) and the surrounding passive areas (cathode). This galvanic corrosion is in addition to the active corrosion of the wear debris and wear track within the aqueous environment.

The current study addresses this technological gap, which has been very scarcely addressed for a dynamic lubricant medium [30-33]. The chapter details an original design of a 'modifiable' lubricant monitoring system (LMS) for the investigation of tribocorrosion. This LMS consists of a test rig that integrates the wear analysis of a tribo-pair in a lubricating medium with a three-electrode electrochemical cell set up. The test rig can monitor the in-situ corrosion rate of the lubricant while monitoring the wear rate between the tribo-pairs in contact. Further, this set-up is used to perform a series of tribocorrosion tests using industrial grade transmission oil under various contamination conditions. These tests provide an insight into the reliability of the test rig as an in-situ LMS for lubricants used in dynamic environments.

1.2. Surface engineering to modify tribology and tribocorrosion

A mechanical system consists of several moving and contacting surfaces which are designed to perform consistently with maximum efficiency and minimal energy losses. Whether the surfaces are engineered [34] and/or bio-mimicked [35], understanding the tribological behavior of these

surfaces plays a vital role in determining the retrograding process of the mechanical system as a whole. Hence, improving the tribological behavior of material surfaces along with their mechanical and metallurgical properties has become an integral part of manufacturing. The manufacturing processes studied are some of the most reliable forms of surface modification strategies, can be used to understand the potential of modifying the tribological and tribocorrosion behavior of surfaces.

1.2.1. Laser shock peening (LSP)

LSP is a laser-based surface engineering process, which has been used for widespread industrial applications [36-39]. LSP utilizes laser-induced shock waves that cause micro-yielding on the material surface by introducing compressive stresses with minimal cold working effects. The basic process of LSP is illustrated in *Figure 1.3*, where the target material is covered with an ablative coating such as a black tape or a metal foil [40].

During the LSP process, the laser-matter interaction results in the formation of laser-induced plasma whose expansion is constrained by transparent confinement. Due to this confinement, a laser-induced shockwave with a high peak pressure (in the order of GPa) propagates into the surface of the target material, leading to an ultrahigh strain rate plastic deformation (10^5/s ~ 10^6/s) [37]. As a result, near-surface compressive residual stresses and work-hardened layers are introduced. It has been observed that these residual stresses and work-hardened layers play an important role in defining the tribological properties of a surface [41]. The LSP process has been applied to a variety of alloys that have been used in aircraft engines, airframes and fittings, overhead power line connections in aluminum conductor steel-reinforced (ACSR) cables, electrical connectors involving aluminum connections with steel, damage tolerance enhancements on the leading edges of compressor blade, marine fittings and hardware, valves and valve parts [42-48]. The LSP process is more routinely applied to turbine engine blades in commercial and military engine components, and turbines used in electrical power generation where they are exposed to extreme working conditions. Currently, the usability of LSP has been limited due to the high equipment cost and intricate quality control set-up associated with the process.

The advantage of the LSP process can be attributed to the ability of LSP to produce compressive residual stresses that are ten to twenty times deeper than shot peening, resulting in resistance to crack initiation, fatigue, and wear [49]. However, the most important characteristics of LSP that has drawn attention are its high precision, adjustable process control, and applicability to complex

geometries [49, 50]. The LSP is a computer-controlled process using integrated robotics to manipulate the process. LSP process parameters, such as power density and laser pulse can be optimized and controlled precisely to tailor the required compressive residual stress profiles. These characteristics of the LSP process has encouraged tribologists to envision LSP as a sustainable surface engineering technique to control the tribological properties of metallic surfaces. Though many of the tribological studies on LSP have capitalized on the characteristics of the process, the tribological study of LSP treated surfaces have been limited to hardness and wear enhancement characterizations [45, 51-54]. This technological gap needs to be addressed by studying the effects of LSP on wear, corrosion, tribocorrosion, surface energy, surface roughness, and coefficient of friction (COF) of metallic surfaces.
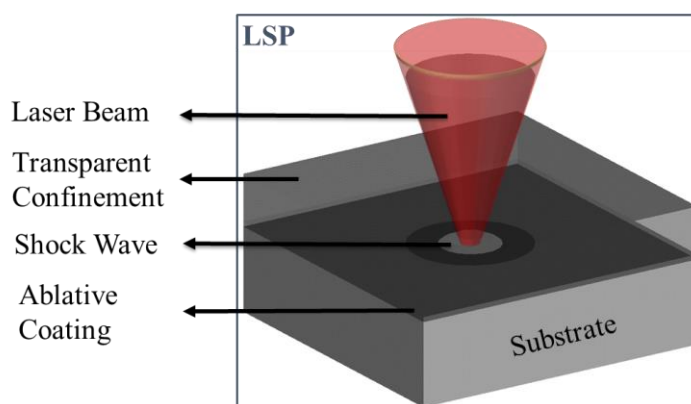
Figure 1.3: Schematic of Laser Shock Peening (LSP)

1.2.2. Electrodeposited nickel-graphene (Ni/GPL) coatings

Electrochemical composite coatings are widely investigated coatings due to its versatility in tailoring engineered surfaces with physio-mechanical and tribological properties. The effectiveness of these coatings for tribological applications is dependent on the solid–liquid interfaces. The application of composite coating is a state-of-the-art method that can produce highly durable and reliable novel materials at room temperature for advanced technological applications [55, 56]. A nanocomposite coating compared to other coating types provides excellent functional properties such as wear and corrosion resistance to the coated surface due to the introduction of nanoparticles in the coating metal matrix [57, 58]. Nanocomposite coatings play an important role in the development of a new generation of sustainable multifunctional materials with unique characteristics that include enhanced mechanical strength, and increased resistance to scratch, heat, wear, and corrosion. Compared to the traditional composite coatings, the superior

performance of their nanocomposite counterparts is attributed to the improved morphology with nanoscale phase-separated domains. Various nickel matrix nanocomposite coatings comprise of a diverse range of inert nanoparticles such as Al_2O_3, SiC, ZrO_2, graphene (GPL), TiO_2, and diamond, etc., have been electrodeposited using electrolytes with suspended nanoparticles [59-63].

Tribocorrosion in a lubricating medium is a complex mechanism that affects the performance of the substrate and its boundary lubrication mechanism in distinct ways. The substrate is affected by wear, corrosion, and corrosion products, while the lubricant medium is degraded by the wear particles and the corrosion products. Hence, for consistent performance, nanocomposite coatings are a feasible method of providing multi-functional properties to the substrate surface. The multi-functionality of the surface coatings will dictate the resistance of the surface to the synergistic effect of wear and corrosion. A controllable and versatile coating technique – pulsed electrochemical deposition – can be used to produce such coatings. The schematic of a pulse electrochemical deposition process is shown in *Figure 1.4*.
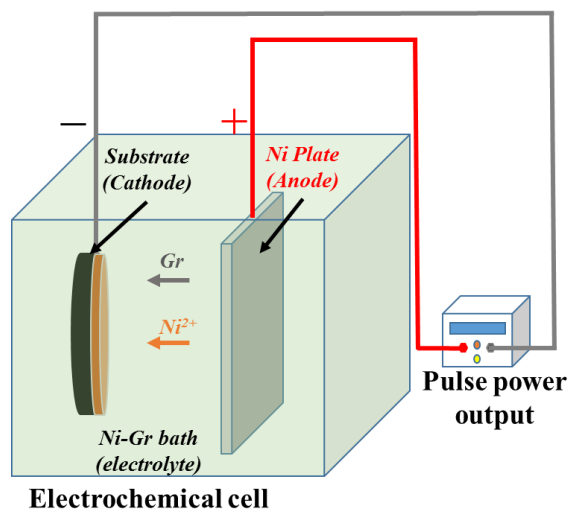
Figure 1.4: Schematic of pulse electrodeposition process for nickel-graphene nanocomposite coatings

Graphene is a lightweight, impermeable, atomically thin, wear-resistant, mechanically strong, and inert material that has become one of the most sought-after materials for a composite coating. Graphene nanosheets and platelets have been extensively used as nanomaterial additives in composites and lubricants to enhance the tribological properties due to their layered crystal structure [64-71]. In a composite surface coating, graphene has been shown to provide the substrate surface with enhanced wear, corrosion, and hardness properties, which are significant in improving

the tribological behavior [72-75]. Further, the presence of graphene in composite surface coatings provides high flexibility, which helps compensate micro curvatures or changes in surface roughness of the coated substrate while still providing a stable coating. This aspect of graphene composite coatings has made it suitable even for flexible electronics and other electrotechnical applications [76]. One of the most upcoming and innovative forms of graphene composite coating application involves embedding graphene nanoribbon-infused epoxy in a section of helicopter blades and aircraft wings to remove ice through Joule heating [77]. One of the significant scientific shortcomings of graphene-based composite coating is the lack of knowledge on its tribocorrosion behavior [78-84].

Recently, investigations have been conducted to fabricate graphene reinforced nickel metal matrix nanocomposite coatings for improving multiple functionalities that concern electrical, mechanical, and physical properties of the surface. This Ni/GPL film that is electrodeposited also has excellent tribological and anticorrosive properties with an excellent surface finish. This has increased its applicability to strategic industries such as automotive, aerospace, petroleum, and electronics. However, metallic films electrodeposited on the metal substrates are assumed to always show a favorable adhesive strength since the electrodeposited films bond with substrates metallically. The idea behind utilizing these specific combinations of coating materials is that they have been researched extensively and are reliable forms of composite coatings that are resistant to corrosion and wear [72, 73, 75, 85-93]. Since most of the published research on prior mentioned coatings was concentrated on discrete effects of wear and corrosion, there is a need to understand their synergistic effect. Hence, a detailed understanding of the wear-corrosion synergism in these coatings is necessary. This technological gap is also addressed in this dissertation, where the tribocorrosion behavior of Ni/GPL nanocomposite coatings is investigated.

1.3. Significance and Motivation

Tribocorrosion is a challenging phenomenon to investigate and to distinctly understand its influence on the performance of the tribo-system. This is due to the complexity of coaction between two distinct processes, namely wear and corrosion. For a given mechanical system, there can be multiple forms of wear-accelerated corrosion and corrosion-accelerated wear, which is simply referred to as wear-corrosion synergism. If the working conditions and variables of the tribo-system are well-defined, then the studies presented will be an effective guide to define

experimental methodologies and scientific investigative techniques to understand the degenerative effects of tribocorrosion. These degradation processes can have major impacts that can directly lead to physical injury or death, for example due to failure of biomedical implants, contamination of the environment, and financial losses from equipment, material, and lubricant that need to be replaced. The wear-corrosion synergism may be due to a combination of one or more forms of wear that synergistically accelerate the degradation process along with one or more forms of corrosion. The wear processes can occur as adhesive, abrasive, delamination, erosion, or fatigue wear, whereas the corrosion processes can occur in the form of a galvanic, crevice, pitting, fretting, or stress corrosion. These aspects of tribocorrosion have made it challenging to scientifically investigate and understand the accelerated degradation effects on materials in an electrochemically active environment.

Further, the study examined the tribocorrosion behavior for magnesium alloys. Magnesium alloys are lightweight materials with exceptional ductility and are now widely being used in the fields of automobiles, aerospace and manufacturing. Magnesium alloys possess unique features where they can be recycled while retaining their material and mechanical properties. Today, these alloys are being used as intelligent product solutions and commercial application solutions. More specifically, the tribological applications involve magnesium alloys subjected to sliding in automotive brakes, engine piston and cylinder bores where they contact other materials such as aluminum alloys. Further, friction and wear of magnesium alloys are also of interest in their processing using extrusion, forming and rolling. The potential of magnesium alloys has made it an extensively researched smart material for the future. The practical and theoretical knowledge on the tribological and tribocorrosion behavior of magnesium alloys can promote the applicability of these alloys for diverse and energy efficient causes.

The studies undertaken will provide a mechanical engineering perspective on the interdisciplinary aspects of tribocorrosion and its mitigation techniques, which will promote the application of magnesium alloys for automotive and biomedical industries. The results discussed in the present study is applicable to a wide spectrum of industries:

- *Lubricant industries*- lubricant monitoring systems, multifunctional lubricants, and extreme environment lubrication.
- *Petrochemical industries* - synthesis of multifunctional oils and additives, oil lifecycle enhancement.

- *Marine, Mining, Automotive, and Aerospace industries* - enhancement and degradation analysis of mechanical components and surfaces (for example, rock cutters, drill bits, propellers, earth moving equipment etc.) in aqueous, lubricated, and extreme environments.

- *Food, and Biomedical sectors* - enhancement and degradation analysis of food processing machineries, dental and biological implants (e.g. hip implants) exposed to chemically active environments.

1.4. Research objectives and outline

With the research motivation discussed above, the present study aims to understand the effect of various surface characteristics on the tribocorrosion behavior of functional surfaces. The study investigates the related tribocorrosion mechanisms and the factors that influence tribocorrosion. The research has focused on the following main objectives to gain an understanding of the tribocorrosion mechanisms and its mitigation methods:

(a) Monitor tribocorrosion *in-situ* for various surface characteristics, lubricants/aqueous environments, and tribo-interface conditions. A focus is placed on understanding the mechanism of tribocorrosion and designing surfaces with enhanced tribocorrosion resistance.

(b) Study the effect of surface engineering methods, such as textures and coatings on tribocorrosion. The focused surface engineering methods include surface processing using LSP on steel and magnesium alloys, and coatings on surfaces using nickel-graphene nanocomposite. The environmental conditions include aqueous environments that simulate seawater conditions.

(c) Investigate the correlation between surface roughness, surface energy, wear, corrosion, and wear-corrosion synergy in defining the tribocorrosion mechanisms.

The intellectual merits of the research include (1) understanding the association between electrochemical and mechanical processes that affect the material and lubricant degradation; (2) innovating solutions to mitigate tribocorrosion in advanced manufacturing and material processing applications; and (3) designing materials resistant to tribocorrosion. The studies conducted to achieve these objectives are detailed in this dissertation, as outlined below:

- Chapter-2 discusses the tribological and tribocorrosion state-of-art for surface engineering techniques, specifically LSP and nanocomposite coatings with relevance to magnesium and steel alloy material systems.

- Chapter-3 details of the equipment and characterization techniques used in the present study.

- Chapter-4 details the design of a lubricant monitoring system to investigate and analyze tribocorrosion in dynamic lubricated environments. This chapter details the design and fabrication of a system to investigate tribocorrosion in-situ. The system and methodology are detailed for examining the in-situ tribocorrosion behavior of functional surfaces in the present research.

- Chapter-5 details the tribological and surface roughness studies conducted on engineered surfaces. The engineered surface studied were laser shock peened at various laser intensities to modify the surface characteristics and tribological properties in addition to the mechanical properties. This chapter provides a fundamental understanding of the tribological behavior of LSP surfaces and how surface roughness can be controlled using this process. The chapter also discusses phenomenological models developed to detail the effect of LSP on surface roughness, tribology, and tribocorrosion.

- Chapter-6 investigates the tribocorrosion behavior of LSP processed surfaces and the underlying mechanisms. The chapter uses the equipment and methodology detailed in Chapter 4 to investigate the tribocorrosion behavior of engineered surfaces such as those manufactured using LSP. The chapter details a phenomenological model describing the effect of surface roughness on the tribocorrosion behavior.

- Chapter-7 details the effect of surface energy change due to LSP on the tribocorrosion behavior of the surface. The influence of surface energy and roughness on the tribocorrosion of engineered surfaces is discussed in this chapter.

- Chapter-8 details the studies concerning the effect of nanocomposite coatings on tribology and surface energy behavior of the surface. The nickel graphene-based coatings are fabricated and studied.

- Chapter-9 Nanocomposite coatings are fabricated and the tribological and tribocorrosion behaviors are studied considering the surface energy behavior of nickel-graphene nanocomposite films.

- Chapter-10 summarizes the results and conclusions of the current research work.

Chapter 2: Literature review – Surface Engineering, tribology, and tribocorrosion

Surface engineering techniques have become an integral part of the manufacturing process to enhance and control the mechanical and tribological properties of surfaces. This chapter details the current state-of-the-art concerning the tribological implications of surface engineering techniques, such as laser shock peening (LSP), and Ni/GPL nanocomposite coatings. Further, the state-of-the-art concerning factors affecting tribocorrosion behavior for these engineered surfaces are discussed [40, 94].

2.1. Laser shock peened surfaces

2.1.1. Surface roughness and tribology

LSP is a laser-based surface engineering process, which has been used for widespread industrial applications [36-39]. LSP utilizes laser-induced shock wave to introduce compressive stresses as well as surface hardening effect on the target surface. The basic process of LSP is illustrated in *Figure 1.3*, where the target material is covered with an ablative coating to absorb laser energy. During the LSP process, the laser-matter interaction results in the formation of laser-induced plasma whose expansion is constrained by a transparent confinement. Due to this confinement, a laser-induced shockwave with a high peak pressure (in the order of GPa) propagates into the surface of the target material, leading to an ultrahigh strain rate plastic deformation (10^5/s ~ 10^6/s) [37]. As a result, near-surface compressive residual stresses and work-hardened layers are introduced. These surface alterations play an important role in defining the tribological properties of a surface [42-48].

As compared to other surface engineering techniques, such as shot peening [95, 96], ultrasonic impact treatment [97, 98], laser surface melting [99, 100], and surface coating deposition [101], LSP provides advantages such as higher flexibility and accuracy, deeper compressive residual stress, and less damage to the initial surface [50, 102]. These characteristics of LSP has encouraged tribologists to envision LSP as a sustainable surface engineering technique to control the tribological properties of metallic surfaces. LSP on the brass material surface was studied by Wang et al. [103], where it was shown to enhance the microhardness by 28.3% and reduce the wear mass loss by 31.78%. This enhanced microhardness and wear resistance was attributed to the laser beam overlapping ratio which defines a specific peak pressure during LSP. LSP on 7075-aluminum alloy

surface was studied by Wang et al. [104], where the authors concluded that LSP is an effective approach to decrease the depth and width of wear scars and to reduce the abrasion loss in a seawater environment. These observations were attributed to the grain refinement during LSP which increases the surfaces hardness and abrasion resistance. Similarly, LSP of duplex stainless steel surfaces was studied by Lim et al. [105], where it was shown that a high laser intensity of 10 GW/cm^2 could be used to reduce the wear volume and corrosion in seawater by 39% and 74.2%, respectively. These enhancements were achieved though optimization of LSP process parameters, which aided in reducing the number of corrosion pits on the wear track. In another study, the influence of LSP on the wear and degradation performance of AZ31B magnesium alloy surface was investigated by Zhang et al. [48]. Based on the observed changes in surface hardness, it was reported that LSP increased the yield strength of magnesium alloy surface from 128 to 152 MPa along with significant wear resistance enhancements.

Although most tribological studies on LSP have focused on the enhanced surface hardness and wear resistance [45, 51-54], the friction behavior and surface morphological changes due to LSP are not well explored. This might be attributed to the complexity of combined surface strengthening and roughening effects introduced by LSP. The investigations conducted by Petan et al. [106, 107] on the effects of laser intensity and spot size for LSP of maraging steel surface indicate that the LSP performed without an ablative coating can generate a relatively low surface roughness. An investigation conducted by Ren et al. [108] using Ti-6Al-4V alloy shows that LSP with a low laser intensity could reduce the surface roughness considerably. Similarly, Zhang et al. [48] showed that a low laser intensity treatment of AZ31B magnesium alloy surface produces dimple effects with a low average surface roughness as compared to the dimple effects observed at a high laser intensity. These reports have studied the effect of LSP on surface morphology, but there is insufficient use of surface roughness parameters to define the effect of LSP on surface morphology. Most of these studies consider 2D, and 3D surface roughness parameters of average roughness (R_a/S_a), the maximum height of the profile (R_z/S_z), and the root mean square roughness (R_q/S_q). However, tribological studies concerning surface roughness have shown that different textured surfaces with a similar average surface roughness (R_a) can exhibit varying tribological properties regarding the COF and the amount of transfer layer formation [109-111]. This indicates that one or two surface roughness parameters are insufficient to quantify the topographical changes observed on a given surface and to describe the functional characteristic like friction [112, 113].

Menezes et al. [112, 114] conducted a series of investigations concerning the influence of surface texture and surface roughness on the COF. In these studies, different surface textures were characterized by 25 roughness parameters, including hybrid and non-dimensional roughness parameters. These roughness parameters were then correlated to the friction behavior of the surface textures. It was shown that the variations in COF for different surface textures (with similar surface roughness) were due to the dominant influence of the plowing component of friction at the asperity contact [109, 114-116]. Since the asperity slope on the harder surface defines the plowing component, it is necessary to study the dominant surface roughness parameters affected by the LSP process and its influence on the friction behavior [40, 102, 117].

The tribological study presented in Chapter 5 aims to characterize the effect of LSP on surface morphology and friction behavior of metallic surfaces with a specific focus on the influence of laser intensity on surface roughness, coefficient of friction (COF), and transfer layer formation. As a result of this investigation, a surface behavior model describing the effect of laser intensity on surface morphology has been developed. The study also demonstrates the use of an effective surface modification technique to control the tribological properties of a surface.

2.1.2. *Tribocorrosion behavior of magnesium alloys*

Magnesium-based metallic materials and mechanical components have been developed as a new generation of load-bearing materials due to their lightweight and low-density (1.74-2.0 g/cm^3) properties. However, their low elastic modulus (41-45 GPa) and compressive yield strength (65-100 MPa) combined with poor wear and corrosion resistance have limited their applicability. Using LSP to enhance the tribological and electrochemical properties of the magnesium (Mg) alloy surfaces, especially AZ31B Mg alloy, is one of the engineering solutions which has aided in capitalizing on its unique material properties [48, 118]. Zhang et al. [119] have shown that when AZ31B surfaces are LSP processed, they can have friction and wear reduction by 4-5 times due to the surface strengthening effect of LSP. It was indicated that refined grains in the LSP processed surfaces lead to a deeper oxidation layer, which affects the wear behavior. Additionally, it has also been shown by Siddaiah et al. [40] that depending on the applied laser intensity, which affects the surface strengthening and the surface roughening effect, it is possible to modify and control the tribological behavior of the surfaces. In the present study, $Mg(OH)_2$ is expected to be the predominant oxide film on AZ31B during the wear process [120].

Further, it is evident from the corrosion potential of Mg in the standard galvanic series that its alloys will be easily susceptible to corrosion in the presence of an aqueous environment. The susceptibility of Mg to corrosion has relegated the use of Mg-alloys in areas that are unexposed to the atmosphere, including car seats and electronic boxes [121, 122]. The overall corrosion reaction at the corrosion potential of Mg is represented as below:

$$Mg + 2H_2O = Mg^{2+} + 2(OH)^- + H_2$$
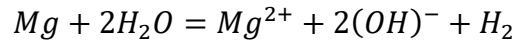
It can be seen that the corrosion of Mg usually leads to the evolution of hydrogen and the formation of hydroxides that can have an adverse effect in a tribo-system. The corrosion resistance of Mg-based alloys is usually considered inadequate due to their low standard corrosion potential of -2.37 V compared to a standard hydrogen electrode (SHE). This being one of the major drawbacks of Mg-based alloys, it is crucial to understand the corrosion mechanisms under various tribological and service conditions. The low corrosion resistance of these alloys is mainly due to the formation of imperfect and unprotective oxide films on the surface and the galvanic or bi-metallic corrosion caused by impurities and secondary phases [123]. When a tribocorrosion system is considered, the Mg alloys are expected to follow the latter mechanism of corrosion that involves a galvanic couple of worn and unworn areas of the same surface [124, 125]. When this galvanic couple interacts with the wear debris and corrosion products, it leads to the acceleration of corrosion by wear [126]. The conducted tribocorrosion studies are presented, which focus on investigating this behavior of AZ31B surfaces that have been processed with LSP. The study investigates the changes in surface roughness, microhardness, friction, wear, and tribocorrosion during sliding in 3.5% NaCl solution. The study provides qualitative insight into the wear-accelerated corrosion mechanism for LSP at various laser intensities.

2.1.3. *Influence of surface energy*

Considering the potential of Mg alloy, it is necessary to understand how surface processing and surface modification techniques affect not just the wear and corrosion properties but also the tribocorrosion properties. Recent studies on the tribological and tribocorrosive effects of LSP and other such surface engineering processes have provided significant insight into the role of surface roughness, hardness, and residual stresses in defining the wear, corrosion, and tribocorrosion mechanisms [40, 102, 127]. The application of AZ31B can be sustainable only if the tribological and tribocorrosive mechanisms are understood in various aqueous environments. In environments susceptible to corrosion, the surface roughness (SR) can drastically modify the wettability of the

surface by affecting the surface energy. The change in surface roughness is more drastic in the case of Mg alloys due to their high ductility [40, 117, 127, 128]. The change in surface energy and wettability alters how aqueous solutions interact with the surface and thus, results in altered wear, corrosion, and tribocorrosion behavior.

The work required in order to hold a unit surface area intact is defined as surface energy in solids and liquids. In liquids, the mobility of the molecules enables them to easily attain equilibrium, whereas in a solid, the molecules are not mobile enough to minimize the surface area and achieve equilibrium. The surface energy is a key parameter to define the wettability of the surface with a liquid of known surface tension. Even though it is possible to measure wetting in terms of contact angle, it does not provide qualitative and quantitative information regarding the interfacial forces between the solid and liquid, the solid and vapor, and the liquid and vapor interfaces. This makes it difficult to quantify the surface energy of the solids, especially when influenced by surface roughness. Currently, the most effective method to calculate surface energy is the approach based on Lewis acid-base surface interaction components. The three-component approach was developed by Van Oss et al. [129, 130] which can adequately separate the surface energy components and determine the interfacial surface energy as the indicator for solubility. It was shown that in polar systems the surface energy involves Lifshitz-van der Waals (LW) and polar acid-base (AB) interactions:

$$\gamma_s^{tot} = \gamma_s^{LW} + \gamma_s^{AB}$$

where γ_s^{tot} is the total surface energy of the solid (*s*). The acid-base component of surface energy is given by the geometric mean of γ_s^{AB+}, electron acceptor, and γ_s^{AB-}, electron donor given by:

$$\gamma_s^{AB} = 2\sqrt{\gamma_s^{AB-}\gamma_s^{AB+}}$$

The interfacial energy between the solid (*s*) and liquid (*l*), γ_{sl}, can be expressed as:

$$\gamma_{sl} = \gamma_s + \gamma_l - W_a$$

where W_a is work due to adhesion that defines the work necessary to pull apart two surfaces in contact and γ_l is the liquid surface tension. Using the above equations, W_a is:

$$W_a = 2\left(\sqrt{\gamma_s^{LW}\gamma_l^{LW}} + \sqrt{\gamma_s^{AB-}\gamma_l^{AB+}} + \sqrt{\gamma_l^{AB-}\gamma_s^{AB+}}\right)$$

Considering the experimentally determined contact angle with probe liquid (*θ*) with γ_l of the probe liquid and γ_{sl} we get the Young equation for determining S_E of the solid as:

$$\gamma_s = \gamma_l \cos\theta + \gamma_{sl}$$

Surface functionalization using laser-based techniques such as LSP has been studied to modify various properties such as surface hardness [45, 51, 104, 131], wear and corrosion resistance [47, 53, 100, 104], surface roughness [40, 106, 132-134], and wettability [135, 136]. Tailoring surfaces to have multiple functionalities requires experimental techniques to determine and optimize the process parameters based on the application [102, 137-140]. However, without understanding the interactions between surface functionalization via LSP, it is not possible to understand the full potential of LSP. The surface energy study presented, where the influence of LSP on the surface energy interactions at the interface of the AZ31B surface and three probe liquids (corrosive and non-corrosive) is investigated. The study furthers the understanding of surface functionalization using LSP by providing insight into the influence of surface energy on corrosion and tribocorrosion properties. The knowledge of surface energy changes due to LSP will allow better design of AZ31B surface properties for sustainable and diverse applications, including applications in aqueous environments.

2.2. Electrodeposited nanocomposite coating

2.2.1. Surface energy and tribology

Composite electrochemical coatings (CECs) are generating significant interest, both in research and in practical applications—particularly in transportation, electrotechnical, food, and textile industries [141-143]. CECs provide a unique technological edge to enhance the mechanical and tribological properties of the surface. Nickel (Ni) is one of the most common metal coatings used to synthesize CECs as it is characterized by superior corrosion resistance, and enhanced mechanical and tribological properties. Recently, graphene has been used in the electrodeposition of Ni composite coatings known as nickel-graphene (Ni-Gr) coatings for lubrication applications. Such coatings are superior in tribological properties as compared to other hard CECs that consist of chromium, boron nitride, zirconium dioxide, PTFE, etc. [143, 144]. Gr nanosheets and platelets, due to their layered crystal structure, have been extensively used as lubricant additives to enhance the tribological performance [64-71]. Gr being lightweight, impermeable, atomically thin, wear-resistant, mechanically strong, and inert, is one of the most sought-after materials for a composite coating. In addition, Gr in the form of nanosheets and platelets have been used as nanomaterial additives in composites and lubricants to enhance the tribological properties [79, 81-84, 145]. In a

composite surface coating, graphene has been shown to provide the substrate surface with enhanced wear, corrosion, and hardness properties, which are significant in defining the tribological behavior [72-75]. Further, the presence of graphene in composite surface coatings provides high flexibility, which helps compensate micro curvatures or changes in surface roughness of coated substrate while still providing a stable coating. This aspect of graphene composite coatings has also made it suitable for flexible electronics and other electrotechnical applications.

The coating thickness, surface morphology, and mechanical properties vary depending on the electrodeposition process parameters used in the synthesis of Ni-Gr composite coating [88, 90]. Additionally, these characteristics also affect the graphene particle distribution in Ni metal matrix, and hence, affect the tribological properties of the coating. The effect of coating characteristics on the mechanical and wear behavior of Ni-Gr composite coatings have been investigated [73, 75, 146]. Most of the focus was given in either wear resistance or corrosion resistance [88]. Coupling these will have a greater impact on understanding the performance of the coatings, given that most corrosion-resistant elements are not wear-resistant and vice versa [73, 75, 146]. The tribological and mechanical performance of coating has been related to the surface energy [76, 147, 148]. Fundamental understanding of surface energy on the coating performance is largely unknown [147, 149]. It is necessary to understand that these tribological and surface interactions of the coatings are affected by surface energy. The surface energy of the coatings has been known to vary with surface composition and topography [150, 151]. The tribological study presented in Chapter 6 investigates the effect of the surface energy of Ni and Ni-Gr composite coatings and correlates them to the dynamic friction (henceforth referred to as 'friction' in the text) and wear behaviors. The surface energy effect of Gr in correlation to the friction and wear behavior of the composite surface will also be studied in this research.

2.2.2. *Tribocorrosion*

The coating thickness, surface morphology, and mechanical properties vary depending on the electrodeposition process parameters used in the synthesis of Ni/GPL. These parameters affect the graphene particle distribution in Ni metal matrix, which in turn affects the coating thickness, surface morphology, and mechanical properties. Though the effect of these process parameters on the mechanical and wear behavior of Ni/GPL composite coatings have been investigated, there is a lack of fundamental understanding with respect to wear-corrosion synergism in these CECs.

Most experiments test existing coatings that have been developed for either wear resistance or corrosion resistance. Coupling this to the fact that most corrosion resistant elements are not wear resistant and vice versa, these coatings, therefore perform poorly when tested under combined wear corrosion conditions. The synergistic effect of wear and corrosion can cause accelerated material degradation. The tribocorrosion studies performed on Ni/GPL nanocomposite coating electrodeposited on 1020 steel substrate surface is presented in Chapter 6.

Chapter 3: Equipment and characterization techniques

The current chapter introduces various equipment and characterization techniques used to conduct the tribological, tribocorrosion, and surface energy experiments.

3.1. Tribometer and Tribocorrosion testing

The multifunction tribometer from Rtec Instruments shown in *Figure 3.1* was used for the tribological and tribocorrosion measurements. One of the most commonly performed tests on the tribometer is the scratch test. A pin or ball is scratched with a constant force against a fixed sample, and the opposing force in the x-direction is recorded. From this data, the coefficient of friction of the specific tribo-pair can be obtained. This test can be modified by changing the pin, ball, or sample material, the force applied, and the environment in which the test is done by including humidity and temperature controls. Additionally, the interface between the pin/ball and body can be modified by adding solid and liquid lubricants. Wear testing of tribo-pairs can also be performed with this machine. Both linear reciprocating and rotating tests can be done to test wear. In the linear reciprocating test, a pin or ball is scratched against a sample material in a cyclic fashion. The forces are recorded, and the wear value is calculated by 3D profiling the wear tracks. The studies discussed use one or more of these techniques to determine the wear properties of tribo-pairs. During these tests, various additions to the machine have been made that can be used to manipulate the environment and analyze complex tribocorrosion mechanisms. Here a corrosion testing is combined with any of the aforementioned tests. This is done by connecting a potentiostat to the testing materials, like the sample and pin or ball, and various electrochemical experiments can be performed during the tribo tests. The potentiostat is capable of doing potentiodynamic, potentiostatic, open circuit potential, and electrochemical impedance spectroscopy tests, among many others. This type of testing can show how corrosion has an effect on the friction and wear properties of materials and how these parameters can be controlled to obtain better corrosion and wear resistance. Additionally, the tribo-corrosion setup can be further modified by adding both temperature and humidity controls. Overall, the tribometer is the most important piece of equipment in the field of tribology. It allows friction, wear, and tribocorrosion studies to be performed in a variety of environments.
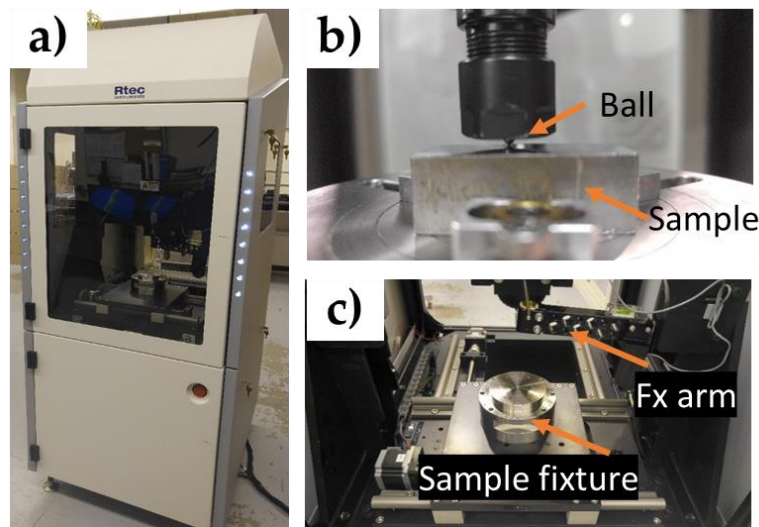
Figure 3.1: (a) Rtec multifunction tribometer, (b) Pin-on-disk scratch testing, and (c) view of the fixture table with Fx arm inside the tribometer.

3.2. Potentiostat and Potentiodynamic testing:

A Gamary Reference 3000 potentiostat (*Figure 3.2*) was used to vary the voltage difference between two connected electrodes, typically used for corrosion testing. The anode, cathode, and electrolyte are contained in an electrochemical cell. Typically, the working electrode (anode) the counter electrode (cathode), the auxiliary electrode, and electrolyte are all connected in a circuit to the potentiostat. Following this, the potentiostat can do a variety of tests, depending on what information is needed. These tests include potentiostatic, potentiodynamic, open circuit potential, and electrochemical impedance spectroscopy, among many others. In relation to tribology, the potentiostat can be combined with a tribometer to perform tribocorrosion testing.
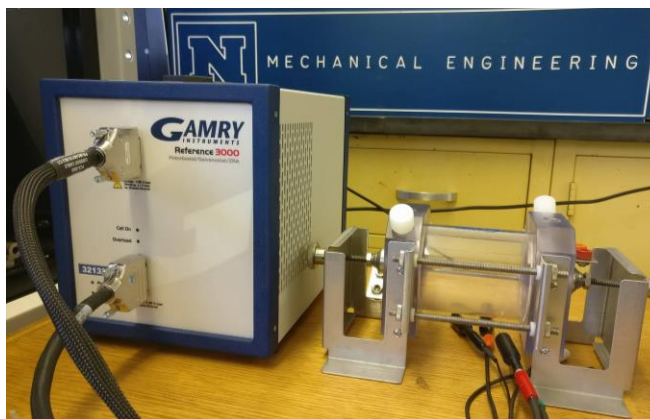
Figure 3.2: Gamry reference 3000 potentiostat alongside the electrochemical cell.

3.3. Goniometer and contact angle measurement

The rame-hart goniometer shown in *Figure 3.3* was used to measure the contact angle and contact angle hysteresis of various surfaces with a given fluid. A droplet in the range of 5-10 microliters is placed on the surface to be studied, and the contact angle is measured. The sample table is then tilted 90 degrees in either direction, which allows measurement of the contact angle hysteresis. The contact angle is directly related to the surface energy of a material, which can be manipulated to change the tribological properties of the surface. Furthermore, the surface energy of a material dictates how prone to or resistant to corrosion a material is. Thus, changing the contact angle can improve or worsen these properties.
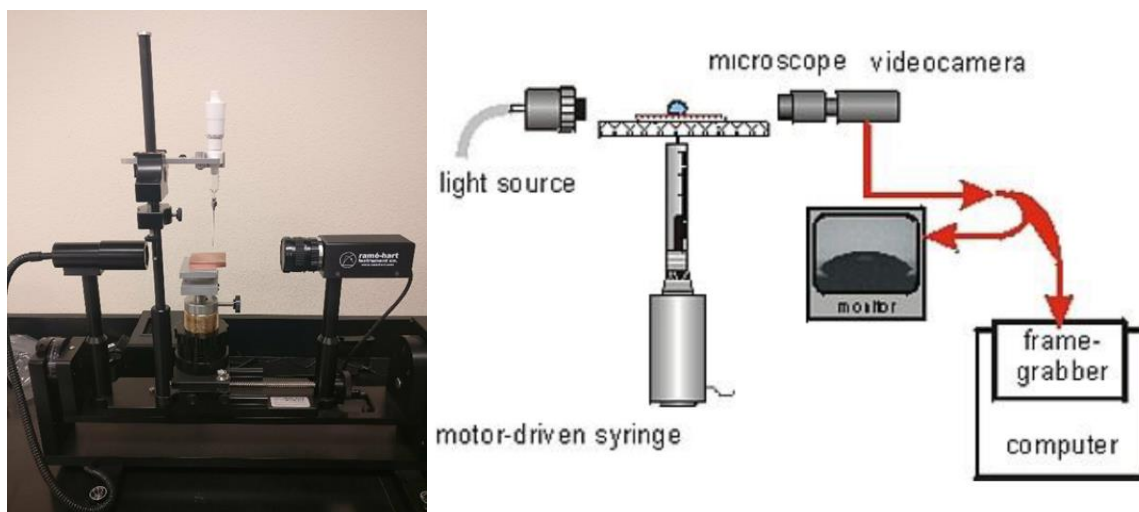
Figure 3.3: rame-hart goniometer/tensiometer with a sessile-drop test fixture.

3.4. Pulse power supply and electrodeposition

A Dynatronix pulse power supply shown in *Figure 3.4* was used for electrodeposition of nanocomposite coatings on various surfaces. A direct current is inputted to the bath in a series of pulses. The pulses can be varied to obtain different coating results. The frequency of the applied pulse can control the density, porosity, and overall distribution of the coating. Furthermore, electroplating can be done with many materials or substrates, including gold, silver, copper, and

nickel. The density, porosity, and coating thickness can all be varied, which will have an effect on the overall friction and wear properties.

Figure 3.4: Dynatronix pulse power supply used for electrodeposition process.

3.5. 3D Surface profiling and analysis

A Rtec Instrument 3D optical profilometer (*Figure 3.5*), which is integrated with a tribometer, has been used in the present study. It has been used to 3D profile surfaces to obtain detailed information regarding the surface morphology and roughness. It operates on the principle of light interferometry unlike an optical microscope. Images are captured by "scanning" over an area, and the light interference or "fringes" are recorded at each height. The acquired data gives detailed information regarding the peaks and valleys of a surface. From this data, additional image processing software, Gwyddion v2.53 was utilized to obtain amplitude, spacing, and hybrid parameters.
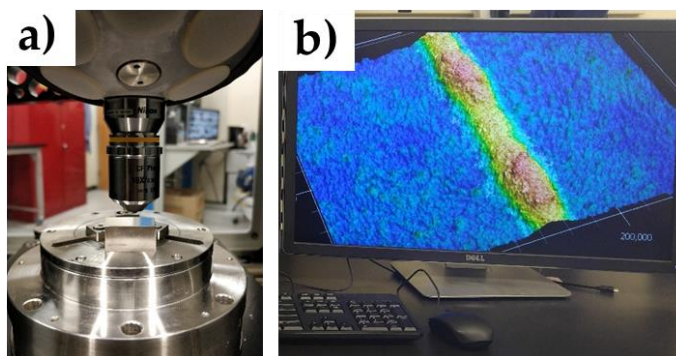
Figure 3.5: Measuring surface profile and roughness using (a)3D optical profiler, and (b) 3D data using image processing software.

3.6. Automated polisher and surface preparation

A Buehler AutoMet 300 automated polishing machine shown in *Figure 3.6* was used to prepare samples for the present study. This machine enabled surface polishing with a random pattern consistently over various samples to achieve the required surface roughness. The machine was used to achieve both high and low roughness values, and mirror-like finish as required for the studies.

Figure 3.6: Buehler AutoMet 300 polishing machine at the Surface Engineering and Tribology lab, UNR.

3.7. Hardness

A Wilson Hardness tester was used to assess the change in hardness due to surface processing. The Vickers hardness test method was used, where the surface of the test material is indented with a diamond indenter with a square based diamond pyramid having an angle of 136° between opposite faces that is subjected to a load of 1 to 100 kgf. The full load is normally applied for 10 to 15 seconds. The two diagonal lengths of the indentation left in the surface of the material after removal of the load are measured using a microscope and their average was calculated. The Vickers hardness is the quotient obtained by dividing the kgf load by the square mm area of indentation. In the present study, a load of 500 g was applied with dwell time of 10 s.

3.8. Scanning electron microscopy (SEM)

A higher resolution piece of equipment, SEM, JSM-7100 FESEM shown in *Figure 3.7*, was used in the studies to characterize surfaces and wear tracks. This SEM has optimum imaging with sub-nanometer resolution of less than 100nm and a magnification that ranges from 25-1,000,000X. The equipment provided insight into the transfer layer formation on the wear track and wear properties of specimens on the micro-level. By observing the surface texture in this detail and mapping specific materials, it was possible to understand various wear mechanisms and identify surface products.

Figure 3.7: JSM-7100 FESEM Scanning electron microscope at UNR.

Chapter 4: Performance analysis of lubricant monitoring system

A major drawback in the tribocorrosion study of functional surfaces is the lack of reliable methods to investigate wear-corrosion synergism in-situ in a dynamic lubricated environment. This chapter details the current state of lubricant monitoring systems and their applicability for in-situ tribocorrosion investigations. The chapter details the design and analysis of an in-situ lubrication monitoring system (LMS), which forms the core experimental technique for the subsequent tribocorrosion studies in this dissertation. All the results and discussions presented in this chapter have been published in a peer-reviewed journal [23].

4.1. Introduction

4.1.1. Lubricant monitoring systems (LMS)

A lubricant, once extracted after use, can hardly be reused and needs to be refurbished or discarded in most cases. Mechanical systems such as automobiles, aircraft, ships, offshore wind turbines, deep sea oil drilling rigs, and a wide variety of machinery use one or more forms of lubricants. The efficient functioning life of these lubricants has been usually estimated by a "thumb-rule" that was related to their cycles or period of usage. Unless a lubricant sample was removed and investigated using several analytical techniques (*Figure 1.2*) specific to the application [34, 152], the exact remaining effective lifecycle of the fluid is difficult to be accurately estimated [153-155]. Over the past few decades, several ingenious methods have emerged for LMS, which have been spearheaded by industrial research and developments (R&D).

The very first noticeable step towards LMS was made when industrial R&D led to a patent filed in 1986 which concerned the corrosion impurity sensor for fluids [156]. This was a significant technological progress when observed from the perspective of fluid quality monitoring. Until around the 1980s, the need for LMS was not significant since the lubricant and lubricating technology was headed in the direction of its synthetic forms. However, with the introduction of the electronic sensor for monitoring the core cooling water of nuclear fusion light water reactors (LWR), it was then possible to detect in-situ, at least one corrosive impurity in a fluid. Around the same time in 1987, another patent that dealt more specifically with an electronic sensor for detecting machine lubricant deterioration, including engine oil of a vehicle was filed [157]. This sensor shown in *Figure 4.1* [156, 157] involved a resistor coated with a thin copper film that

corroded in the presence of acid content in the machine lubricant, indicating the extent of lubricant deterioration.
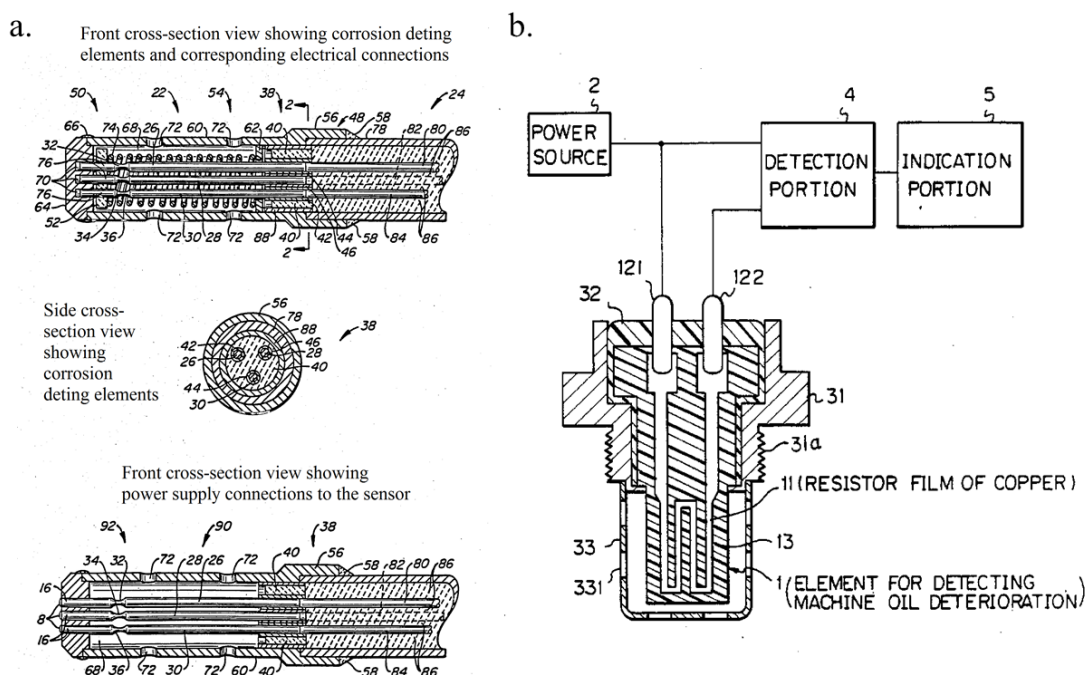
Figure 4.1: The very first fluid monitoring electrical sensors (a) General Electric's corrosion impurity sensor* (b) Nippon Soken Inc. machine oil deterioration detection sensor*. (*Images as filed in their respective patents. The numbers indicate components of sensor specific to the filed patents).

The invention of such in-situ fluid monitoring sensors was capitalized in no time, and research pertaining to the integration of these sensors into mechanical systems and techniques to manufacture them on a large scale started to gain pace. This was evident from the number of high valued patents filed in 1987-88, which tried to integrate and improve these sensors within mechanical systems found in automobile and machine components [11, 158]. Although many of these corrosion-based sensors were better ways of lubricant monitoring, they were not easily integrated into a dynamic system. Most of the R&D undertaken in this field was known to the scientific world only through patents rather than research journals. Even if research were published, it would have been in its infancy as stated in one of the significant reviews from 1988 on wear-debris detection and analysis techniques presented for lubricant based condition monitoring [13]. Although the concept of tribocorrosion was already known during the late 1980s,

tribology of wear debris in lubricants and the simultaneous corrosive effects of these wear debris was yet to be investigated cohesively for lubricants [159, 160].

4.1.2. Recent advances in LMS and their applicability to in-situ lubricant monitoring

The early idea of in-situ fluid monitoring systems based on corrosion initiated by the working environment proved to be the right approach in fluid condition monitoring [11, 156-158]. However, applying this monitoring method for oils and lubricants in a dynamic system proved to be a challenging task [153, 154]. One of the interesting and long-term research approaches was through the integration of particle debris analysis and physical analysis of lubricants through the development of information technology (IT). This research concerned the development and utilization of the information systems relating to the management database and computer-aided wear particle analysis software used for LMS [161-165]. It centered on visual ferrography and IT perspective of increasing the effectiveness and speed of lubricant analysis, improving information management, and using reliable data processing to obtain monitoring conclusions [165-168]. Though these approaches were effective to a certain extent in quantifying wear particles and other contaminants, they are ineffective in actually gauging the real-time synergetic effect on the system performance. These approaches are online monitoring techniques, unlike the more effective in-situ process that gives better insights into the degradation sources of the lubricants and working elements. Following the IT side of research, there have been studies utilizing numerical and soft-analytical methods to determine system reliability based on lubricant analysis using neural network techniques [169-171]. These methods rely on electronic sensors that provide online data for their model analysis and are effective techniques to predict the trend in lubricant degradation and system performance. It implied that the information processing technology plays an important role in processing the data acquired, but their behind-the-scenes role is only as effective as the methodology of monitoring lubricant condition and accuracy of acquiring data [8].

There have been attempts to use spectroscopy and cluster analysis methods, such as two-channel differential dielectric spectroscopy (TD-DES), supervised hierarchical clustering analysis (S-HCA), Fourier transform infrared spectroscopy (FT-IR), ultraviolet-visible spectroscopy (UV–Vis), electrochemical impedance spectroscopy (EIS), and thermal gravimetric analysis (TGA) to provide data on in-service lubricant conditions [172-174]. These methods of analysis are some of the most effective ways of ex-situ lubricant monitoring. Although some research works have

attempted to integrate these for in-situ condition analysis, their commercial viability is improbable due to the complexity of the analytical methods involved.

It can be observed that when it comes to in-situ LMS in a dynamic environment, only very limited research has gone beyond the available standard testing techniques. Still, even the most reliable form of in-situ LMS today are those seen in automobiles, aircraft, ships, and heavy machinery that rely on by-product effect monitoring systems or inline static testing methods [8, 155]. In-situ LMS is even more significant because monitoring the sources of lubricant degradation in a dynamic system can indirectly maximize the lubricant lifecycle.

4.1.3. Limitations of current LMS and tribocorrosion in lubricants

In-situ monitoring of fluid conditions in a dynamic environment using corrosion-based sensors posed a variety of abnormal problems for commercial implementation. These problems resulted in a very low current density due to the type of fluid medium, wear debris, and various contaminants accumulated in the fluid used in the mechanical system [175-177]. Due to the difficulty in integrating corrosion based LMS for commercial applications [175], a new variety of monitoring systems that were based on user handling and lubricant working conditions were introduced. Noticeably, some of the biggest original equipment manufacturers (OEM) in the automotive industry were among the first conducting R&D to integrate this form of electronic LMS in their automotive components for commercial implementation. All these systems simultaneously monitored the engine oil temperature, engine running time, elapsed time since last oil change and other such working conditions to mathematically predict the deterioration rate, and thus, the remaining working lifecycle of the oil [178-180]. Even though patents on many similar systems with new upgrades were filed thereafter [181-184], it was these automotive OEMs who made this electronic LMS commercially viable for implementation and also implemented in most of their automobiles with frequent upgrades since 1988 [185].

The cause of lubricant degradation in most mechanical systems is due to the introduction of one or more forms of foreign contaminants. These contaminants can be the wear debris or by-products generated during the functioning of the mechanical system, for example, water and soot [4-7]. The type of lubricant, boundary lubrication mechanism, and a working environment defines the extent of contamination from wear [7-10]. The lubricant degradation within an enclosed mechanical system is a non-linear process which is initiated by contaminant inclusions but progressively or exponentially accelerated by synergistic effects of wear and corrosion occurring

in the system. The current LMS use sensors to continuously track oil temperature, cycle time, pressure, and elapsed time since the last oil change and other such oil working conditions to predict the extent of oil degradation. These methods of monitoring by-product effects and predicting the extent of lubricant degradation do not consider the synergistic effects of their sources - wear and corrosion. Hence, these electronic-based LMS are not accurate enough to provide for the actual effects of contaminants induced by tribocorrosion [8, 11, 12]. Further, too many by-product effects of lubricant degradation that vary continuously without indicating a predictable pattern. The process of electronically monitoring all these variables and using this data to predict the overall degradation of lubricant makes the estimations much more complex and unreliable in some cases [5, 13-19].

This is the technological gap that is to be addressed in LMS to monitor the *origins* of lubricant degradation, due to wear and corrosion. If an LMS can monitor the synergism between wear rate of the tribo-pairs in contact and the corrosion arising due to the contaminants, this system can be expected to be more reliable than the multitude varieties of electronic-based LMS. This system can further be integrated with the latest corrosion and wear analysis models to provide for condition-based predictive and prognostic outputs.

4.2. Design and evaluation of LMS for in-situ monitoring of tribocorrosion in lubricants

This section of the study addresses the technological gap of monitoring and analyzing the synergism between the wear rate of the tribo-pairs in contact and the corrosion arising due to the contaminants in a lubricant medium [30-33]. An original design of 'modifiable' LMS is presented here. The test rig detailed in this study integrates the wear analysis of a tribo-pair in a lubricating medium with a three-electrode potentiodynamic corrosion set-up. The test rig can monitor the in-situ corrosion rate while monitoring the wear rate between the tribo-pairs in contact. Further, this set-up was used to perform a series of tribocorrosion tests using industrial grade transmission oil under various contamination conditions. A tribometer test rig retrofitted with DC corrosion cell was used to perform in-situ analysis on the effect of tribocorrosion in a lubricant medium. Experiments were performed in accordance with the ASTM standards G119-04 to determine the synergistic effects of wear and corrosion. These tests provide an insight into the reliability of the test rig as an in-situ lubricant condition monitoring system for use in dynamic environments.

4.2.1. Retrofitting of the ball-on-disk test rig

A multi-functional tribometer (Rtec MFT 5000) consisting of a ball-on-disk test rig with lubricant-housing was retro-fitted with a three-electrode corrosion cell setup as represented schematically in *Figure 4.2*. The test rig consists of a rotary lubricant-housing cup containing a disk (specimen) in contact with a ball fully immersed in the lubricating medium. Around this lubricant housing, an adjustable mounting frame was constructed to hold the reference and the counter electrodes immersed in the lubricating medium that was then connected to a potentiostat. The working electrode (which is the disk/specimen of interest) was fixed inside the lubricant housing cup using a screw with a ball-bearing bolt head extending out from the cup connecting to the potentiostat.
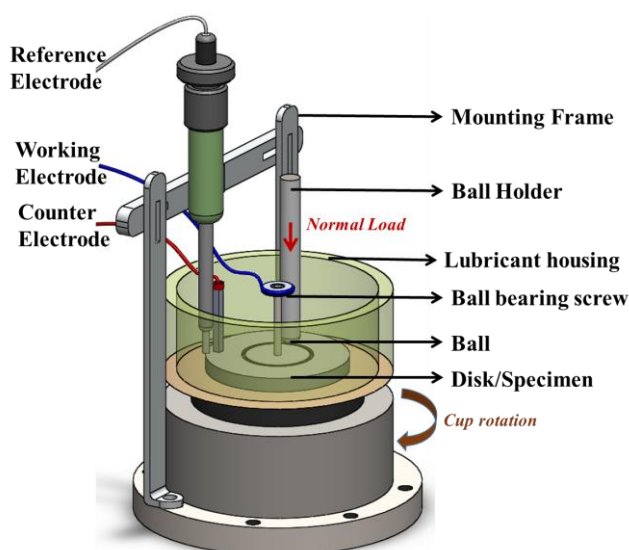
Figure 4.2: Schematic of ball-on-disk test rig retrofitted with three-electrode corrosion cell.

This retrofitted test rig design was aimed to address two major shortcomings of tribocorrosion sets up used in lubricated environments. Firstly, due to the low conductivity of many oils and lubricants, the electrochemical cells for a tribocorrosion setup are found to be very unstable. Hence, the first challenge was to ensure accurate readings of effective resistance in the electric circuit arising from the combined effects of ohmic resistance and reactance. This is to say that the high or low impedance that may be observed in the lubricant housing cup needs to be consistently and accurately measured. This is further complicated by the fact that in tribocorrosion testing the fluid medium is constantly agitated. To overcome this shortcoming, the counter electrode was placed as close to the reference electrode as possible while keeping the counter electrode along the fluid flow direction for minimal flow disruption. Further, specific type and shape of electrodes

were used: A spectroscopic grade graphite counter electrode was machined to have a bulging droplet end to ensure maximum surface area of the electrode was in contact with the lubricant, and a Saturated Calomel reference electrode (SCE) being one of the most robust forms of reference electrodes was found to best suited for the current application.

Secondly, it is not easy to measure the potential of the working electrode accurately when both the working electrode (disk/specimen) and the conducting medium (lubricant) are constantly in motion. This interference was minimized by ensuring close proximity of the reference electrode to the wear track of the ball-on-disk test. Achieving a stable set-up that can provide for accurate and reliable readings during the tribocorrosion test was the first objective of this research, followed by stability testing and analysis.

4.2.2. Materials

Ball-on-disk tests were performed using alumina balls of 6.5 mm diameter and AISI 1020 steel disks of 50.8 mm diameter. The disk material used for experimentation is most commonly used as structural alloy steel in ships, vehicles, railway, bridges and more specifically in power generation applications, mechanical gear, and cam shafts that are exposed to rigorous tribological environments [186-191]. With the aim of analyzing the effectiveness of in-situ tribocorrosion analysis using the retrofitted test rig for lubricant based environments, a lubricant intensive system such as an automobile transmission box was selected as a reference system. The tribo-pair was tested in commercial automotive transmission oil, which meets most commercial automatic transmission fluid (ATF) specifications, as shown in *Table 4.1*.

Table 4.1: Specifications of commercial grade ATF used as the lubricating medium

Automatic transmission fluid specifications (Dextron III)	Values
Volumetric mass at 15°C	867 Kg/m^3
Colour, ASTM	6.5
Viscosity at 40 °C	32.26 mm^2/s
Viscosity at 100 °C	7.1 mm^2/s
Viscosity index	190
Viscosity Brookfield at 40 °C	12600 cP
Flash point Cleveland	183 °C
Pour Point	-48 °C

Today, ATFs are some of the most complicated lubricating fluids that are tribologically versatile in properties and specific to applications. These ATF's must be compatible with all transmission components and operate both at low and high-temperature extremes with consistent performance. Hence, this system, which utilizes one of the most technologically advanced forms of lubricating fluids, will provide for a distinctive idea of the test rig performance when contaminants are introduced to the lubricating medium.

4.2.3. Experimentation

Tribocorrosion experiments under cathodic and anodic polarization conditions were performed using the retrofitted test rig as shown in *Figure 4.2*, according to the test parameters listed in *Table 4.2*. The working electrode sample (disk) with a surface area of 2.027×10^3 mm^2 was exposed to commercial grade ATF medium (*referred to as 'oil' in the following discussions*) at room temperature. Saturated calomel and graphite were used as the reference and counter electrodes, respectively.

Table 4.2: Test parameters of the tribocorrosion measurement.

Test Parameters	Value
Normal Force	10 N
Rotation speed	50 rpm
Duration of wear	15 hr
Wear track radius	15 mm
Ball diameter	6.5 mm
Electrolyte/Lubricant medium	Commercial grade
Temperature	24 °C (room)
Humidity ratio	10 % RH

The experiments were performed in four stages, as listed in *Table 4.3*. Each of these experiments consisted of a specific form of boundary condition, according to ASTM G119-04 standards. Each experiment was performed for 15 h without interruption, during which the coefficient of friction (COF), wear volume, and corrosion rates were continuously monitored. The wear displacement data (change in Z-height of the ball holder) was recorded throughout these experiments and was used to compute the specific wear rate coefficient of the system. Due to the low load conditions and the wear resistant characteristics of the alloy steel ball, there was minimal

contribution of the wear on the ball surface to the Z-height. The computations were based on a system of sphere-on-plane Hertzian contact pressure.

$$k_i = \frac{h_i}{ps}$$

where, h_i = wear displacement (using Z-height data), mm^3; k_i = specific wear rate coefficient; p = contact pressure = $F/A_{wear\ track}$, N; s = slide distance = slide rate $\times$ time = $v \times t$, m.

Table 4.3: Experimental design to investigate tribocorrosion in oil lubricated dynamic environment.

Stage	Objective	Experiments	Data recorded
Stage – I	Establish control wear rate.	Ball-on-disk test in oil medium without corrosion cell set-up.	Wear rate in oil medium.
Stage – II	Establish control for the synergistic effect of wear and corrosion without any external contaminate.	a. Ball-on-disk test in oil medium with corrosion cell set-up. b. Static corrosion cell experiment in oil without wear to isolate the corrosion rate.	Synergistic effect of wear and corrosion in oil medium.
Stage – III	Effect of one external contaminates in the oil medium on synergism of wear and corrosion	a. Ball-on-disk test in - oil + 5% (wt.%) sea salt - medium with corrosion cell set-up. b. Static corrosion cell experiment in - oil + 5% (wt.%) sea salt - medium without wear to isolate corrosion rate.	Synergistic effect of wear and corrosion in oil medium consisting of oil + 5% (wt.%) sea salt.
Stage – IV	Effect of two external contaminates in the oil medium on synergism of wear and corrosion.	a. Ball-on-disk test in -oil + 5% (wt.%) sea salt + 10% (wt.%) water - medium with corrosion cell set-up. b. Static corrosion cell experiment in- oil + 5% (wt.%) sea salt + 10% (wt.%) water - medium without wear to isolate corrosion rate.	Synergistic effect of wear and corrosion in oil medium + 5% (wt.%) sea salt + 10% (wt.%) water.

A sequence was programmed on the potentiostat to monitor the open circuit potential (OCP, E_{OC}) throughout the tribocorrosion experiment. Before the start of each experiment, the sample was ultrasonically conditioned by using acetone and once dried by an air blower. The specimen was then kept in the required combination of oil medium for 1 hr to obtain a stable OCP, which was followed by the 15 hr tribocorrosion experiment. An anodic condition of +0.5 V potential vs. OCP (E_{OC}) was applied to test the sample and accelerate the corrosion process. The cathodic condition was maintained at -0.5 V potential vs. OCP (E_{OC}) to suppress the corrosion process. Throughout these cell conditions, the evolution of current was monitored in parallel with the wear process. After the experimentation, the samples were left in the oil medium for 1 hr to allow for surface re-passivation. The sample was then de-greased by using N-hexane and prepared for analysis of the wear track under a 3D optical profilometer and scanning electron microscope (SEM). The tribocorrosion experiments were performed in three conditions of oil medium listed in *Table 4.4*. The synergism of wear and corrosion has been analyzed in each of these three oil conditions.

Table 4.4: Oil mediums and their contaminants used for tribocorrosion experiments.

Oil Medium	Contaminate Introduce	Oil Contents
Medium - I	-	oil (uncontaminated)
Medium - II	5% (wt.%) sea salt	oil contaminated with sea salt
Medium - III	5% (wt.%) sea salt and 10% (wt.%) water	oil contaminated with sea salt and water

4.3. Results and Discussion

Each stage of the experiment detailed in *Table 4.3* was performed, and their results are discussed and analyzed in this section. Stage I of the experiment was used as the base line to compare the wear behavior of the tribo-pair against the corrosive influence of the oil contaminants tested in Stages II-IV. All electrochemical experiments were performed as DC corrosion tests in the potentiodynamic state as the current study concerns analyzing the influence of cell solution (oil medium) on the phenomenon of tribocorrosion with no coatings on the surface of the sample involved. It is a common knowledge in the electrochemical analysis that the impedance of the resistor (oil medium) is independent of the frequency, and the current through this resistor stays in

phase with the voltage. Hence, the potentiodynamic analysis was found to be appropriate for the present study, which utilizes a single frequency.

4.3.1. Open Circuit Potential (OCP)

The OCP (E_{OC}) i.e. the equilibrium (corrosion) potential of the steel sample in each of these three oil mediums was initially measured for 1 hr (3600 s) as shown in *Figure 4.3*. It can be observed that the sample was able to reach a stable equilibrium potential in all three oil mediums. The OCP of the sample in - Medium-I, uncontaminated oil medium was found to be -232 mV; Medium-II, oil contaminated with 5% (wt.%) sea salt was found to be -210 mV; and Medium-III, oil contaminated with 5% (wt.%) sea salt and 10% water was found to be -84 mV. These values of OCP are initial indicators that even without the influence of wear, the sample in Medium-II and Medium-III containing contaminates will be highly susceptible to corrosion when an electrical potential was applied.
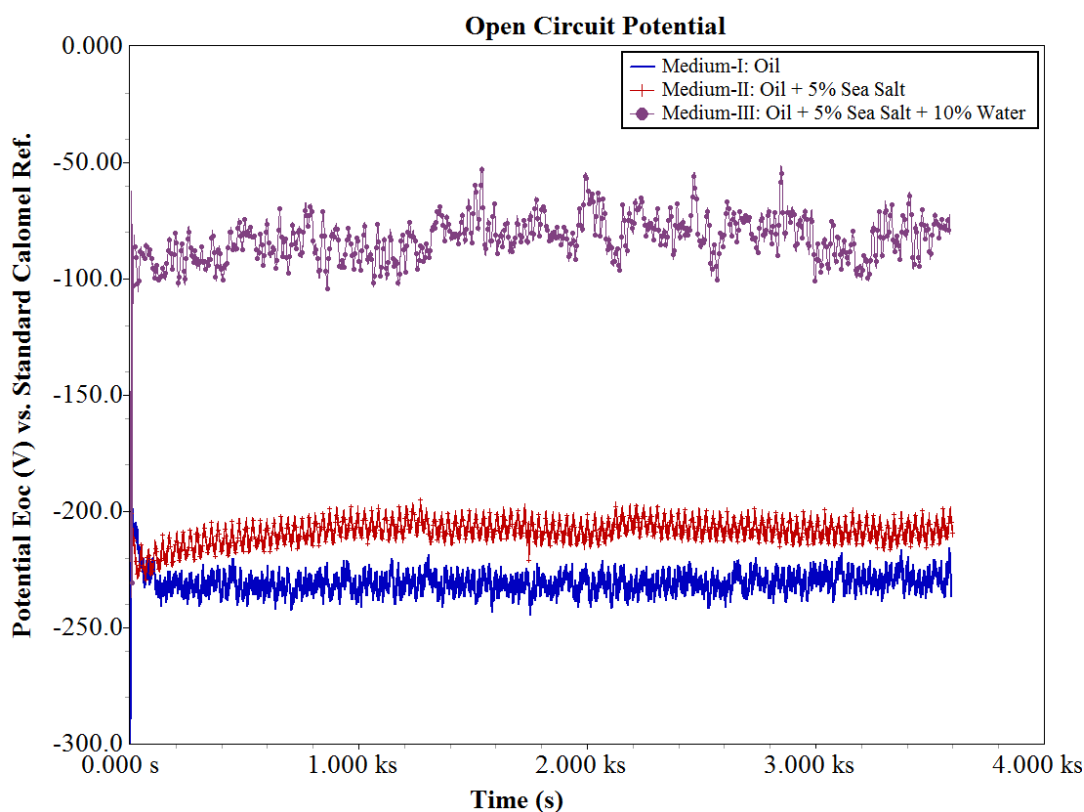
Figure 4.3: Open Circuit Potential (OCP) of the sample in different oil mediums.

4.3.2. Influence of wear on OCP

Once the equilibrium potential was obtained at the end of 1 hr OCP measurement, the tribocorrosion tests were initiated according to the test parameters as detailed in *Table 4.2* for 15 hrs followed by 1 hr of re-passivation. The evolution of OCP before, during and after the wear test on the sample was shown in *Figure 4.4*. It can be observed that the sample in Medium-I was stable throughout the wear test period with minimal variation in potential. This can be attributed to the high resistance of the oil to wear and corrosion in its uncontaminated state, which is a typical characteristic of synthetic oil that was specifically formulated for application in these environments. However, in the case of wear tests performed in contaminated conditions of Medium-II and Medium-III, the OCP was observed to steadily drop from the quiescent conditions, more so in Medium-III than in Medium-II. In the case of Medium-II, the OCP drops from -210 mV to -250 mV, whereas in Medium-III a more prominent drop from -84 mV to -200 mV was observed by the end of the wear test. In all three oil mediums, the sample was observed to re-passivate close to their initial inert conditions soon after the wear test ends.
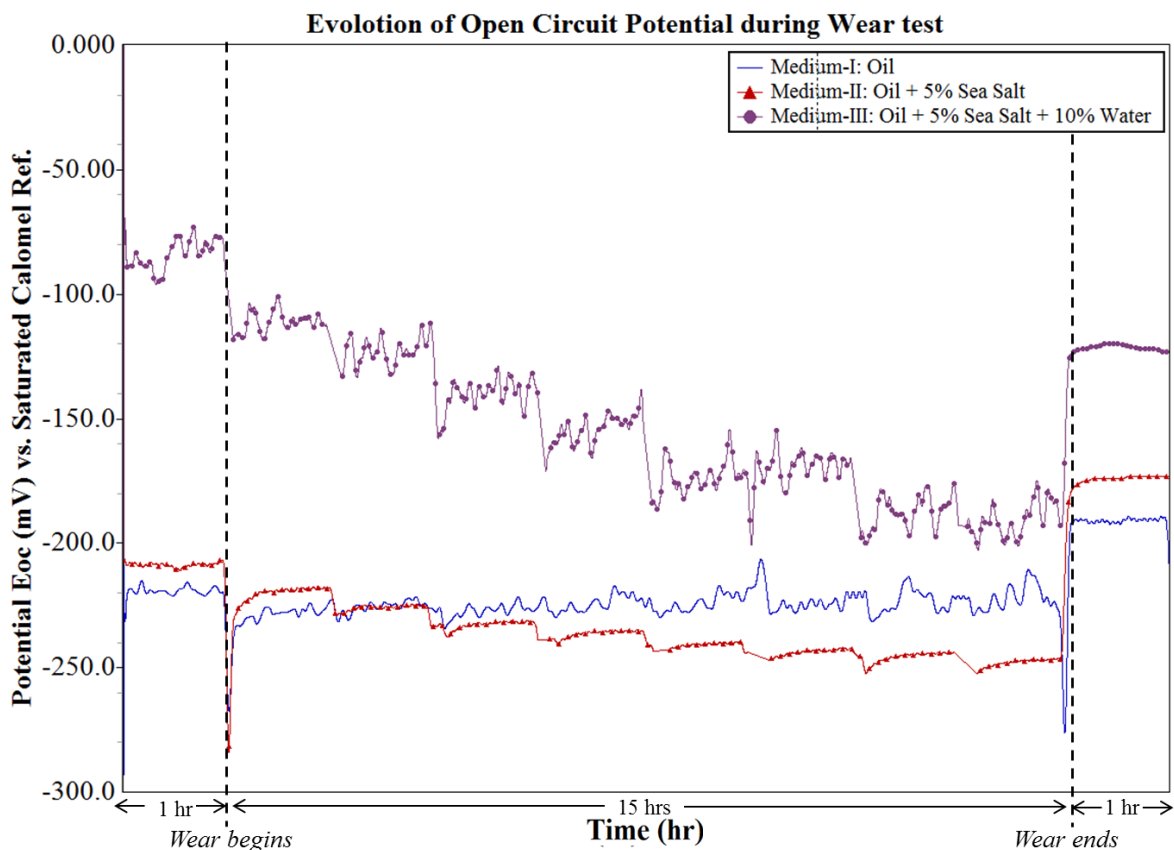
Figure 4.4: Evolution of OCP during wear test in different oil mediums.

A certain degree of oscillation in OCP under each of the oil conditions was observed. The oscillations in case of wear test in Medium-I and Medium-II can be considered not very significant since there can be negligible corrosion products expected in Medium-I and fewer corrosion products in Medium-II on the sample surface. In Medium-III, there was a very high degree of oscillation, indicating the formation and destruction of a large amount of corrosion products on the surface of the steel sample. The presence of water along with sea salt in Medium-III causes accelerated oxidation of steel wear debris and wear track, which was investigated in the later stages of the analysis. It cannot be ignored that these fluctuations in potential can also be due to the cell current variations caused because of the dynamic nature of the experiment wherein the oil medium was in constant motion. This aspect of the experiment would define the stability of the test-rig design for tribocorrosion analysis in oil medium. The influence of the dynamic nature of the experiment on the reliability of data was better understood when analyzing the potentiodynamic results in the following sections.

The effects of wear on OCP during wear test were further investigated by monitoring OCP for 15 hr without wear in all three mediums as shown in *Figure 4.5*. It can be clearly observed that
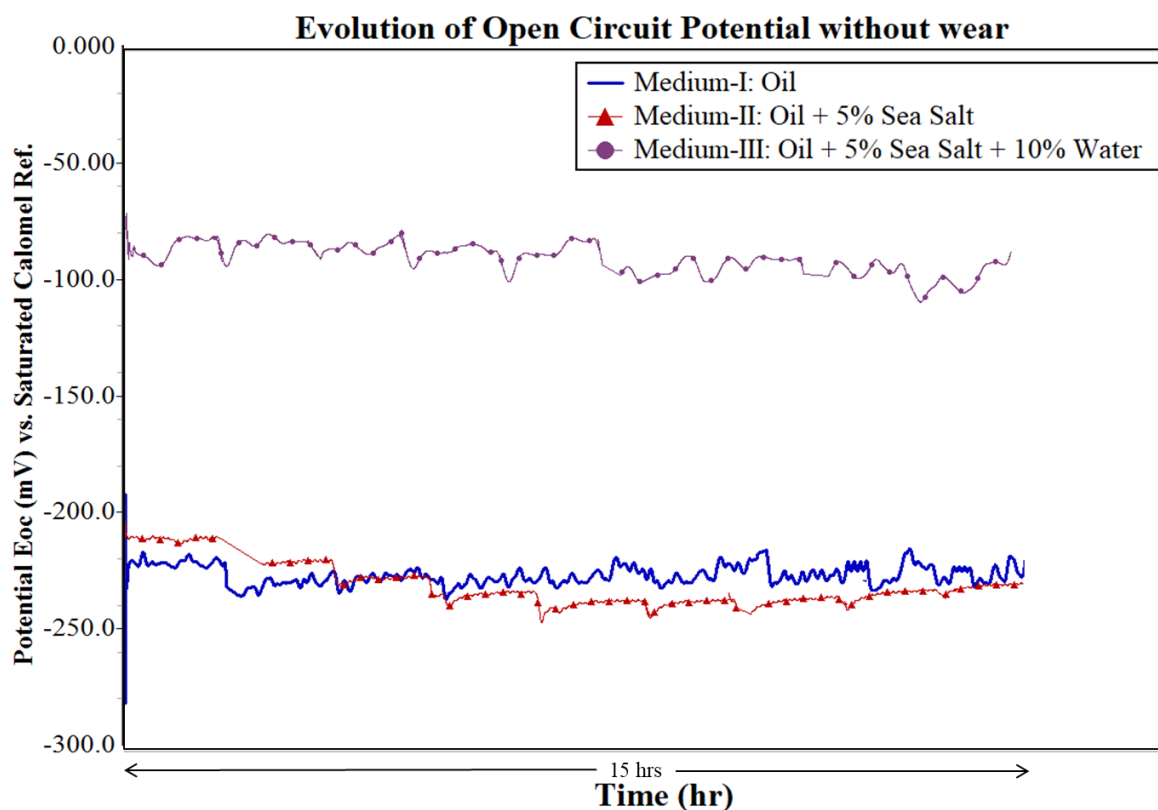
Figure 4.5: Evolution of OCP without wear.

there was a negligible drop in OCP over this period in Medium-I, II and III. It was estimated that over a period of 15 hrs the effect of wear on OCP was such that the OCP drops by 7mV, 36 mV, and 98 mV in Medium-I, II and III, respectively. These variations can be attributed to the change in the cell current flowing through the resistance of the cell solution during the wear. It can be expected that the wear debris continuously entering the cell solution during wear interact with the salt and water contaminates in the solution. This affects the stability of OCP over longer durations with progressively increasing severity.

4.3.3. *Analysis of coefficient of friction (COF) and wear during tribocorrosion test*

The COF was monitored in-situ during the tribocorrosion test as shown in *Figure 4.6*. It was observed that the COF of the tribo-pair in Medium-I gradually decrease over the first two hours of wear and there after becomes stable over the remaining period of the test with an average COF of 0.066. The tribo-pair in Medium-II shows an initial drop in COF with a high slope for the first two hours as compared to that in Medium-I. This was followed by a gradual drop in COF over the following two hours, and the tribo-pair achieves an average stable COF of 0.075 after nearly 4 hours of wear. The period of stability of COF in Medium-II was observed to have been disrupted after 7 hours of wear after which the frequency of COF was affected till the end of the experiment.
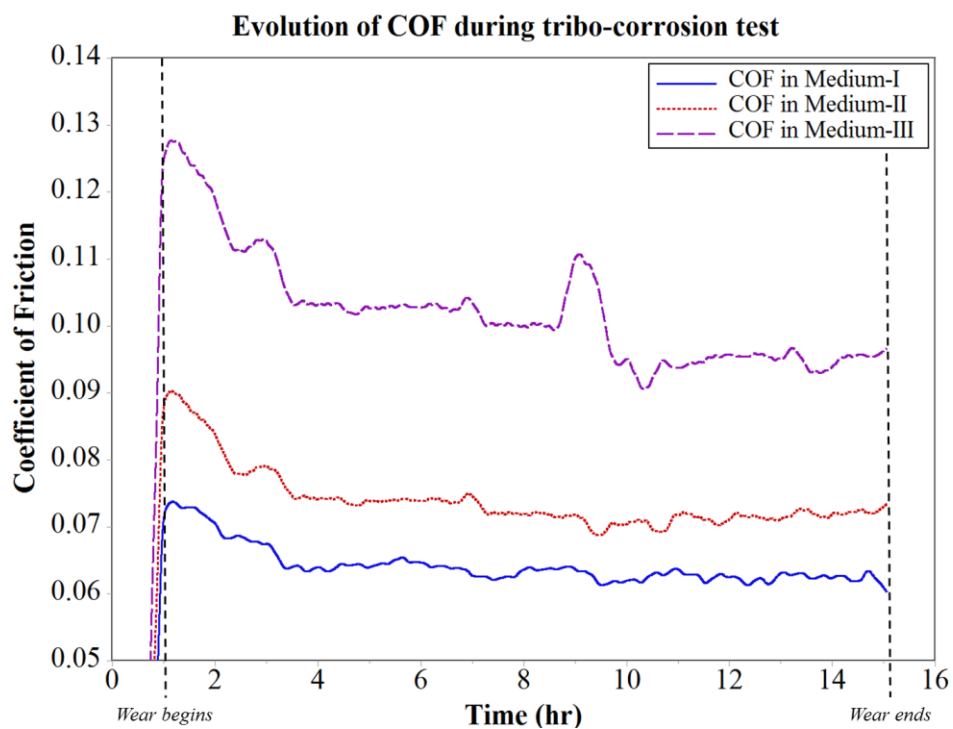
Figure 4.6: Evolution of COF during tribocorrosion testing.

This disruption in COF can be attributed to the sea salt contaminate which at this stage can be expected to react with the wear track causing repeated formation and break down cycles of oxide tribo-layers.

In the case of Medium-III it was observed that for the first 4 hours of wear there was a high initial drop in COF having a considerably high slope when compared to Medium-I and II. This can be attributed to the wear track run-in period that was constantly interrupted by the salt and water contaminants, which are immiscible in oil. At the end of the run-in period, the water contaminants can be expected to have dissolved the salt contaminates forming an aqueous NaCl form of contaminate in the oil Medium-III. Even though the tribo-pair achieves a small duration of stable COF of 0.14 after 4 hours of wear, it was observed to have been disrupted at the end of 8 hours of wear period. More specifically, it is to be noticed that this disruption causes the COF to spike over the next few minutes and then drop with similar frequency. The COF in Medium-III was consistently unstable thereafter. This behavior of COF between the tribo-pair was consistent with the observed wear rate as seen in *Figure 4.7*. The wear rate of the trio-pair in Medium-I and II was found to be increasing consistently with time. But, in the case of Medium-III the disruption in COF observed after 8 hours of wear was because of an increase in the wear rate. At this stage of the analysis, it was speculated that this was the point where the corrosion started to accelerate the wear
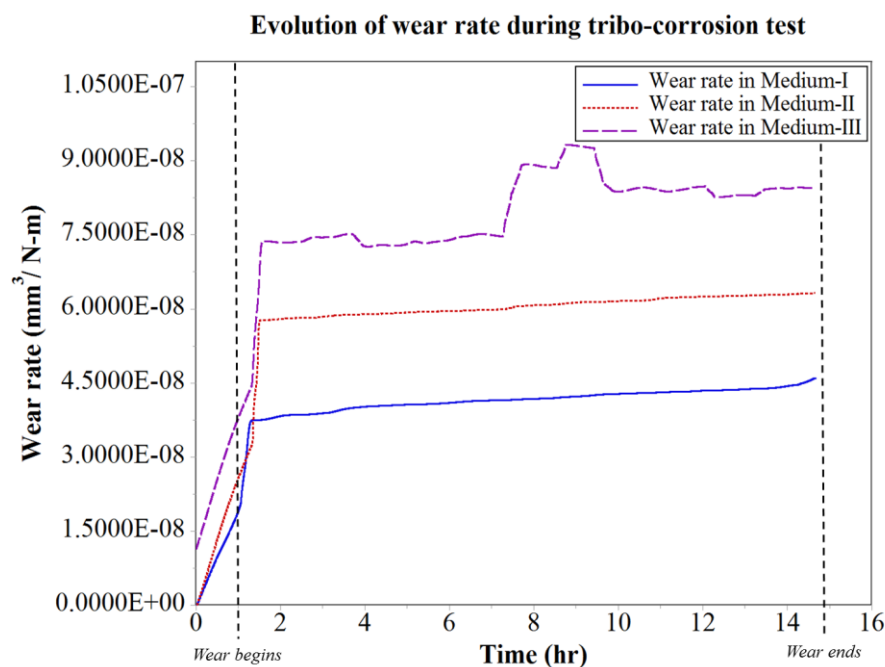
Figure 4.7: Evolution of wear rate during tribocorrosion testing.

occurring at the interface of the tribo-pair during sliding. This phenomenon was evidence to the tribocorrosion in action which was seen to affect COF and wear. Further, the effectiveness of the test-rig design in analyzing and isolating the effects of tribocorrosion in an oil medium with respect to wear and COF was also proven.

The wear tracks in all three mediums were also investigated post experimentation under SEM to gauge the effect of contaminants in the oil medium on the wear track as shown in *Figure 4.8*. It was clear that the uncontaminated condition of oil (Medium-I) was very effective and yielded a wear track that was only 0.774 mm wide as seen in *Figure 4.8*(a). Whereas, the salt contaminated oil medium (Medium-II) shows a wear track of 1.11 mm as seen in *Figure 4.8*(b). Both these wear tracks indicated no visible anomalies along the wear track, whereas the sample in Medium-III which was contaminated with sea salt and water indicated to have a very wide wear track as seen in *Figure 4.8*(c). It can be observed that this wear track bore evidence of cavitation due to contaminating inclusion at the tribo-pair interface which further aided and accelerated synergistic effects of wear - corrosion during sliding.
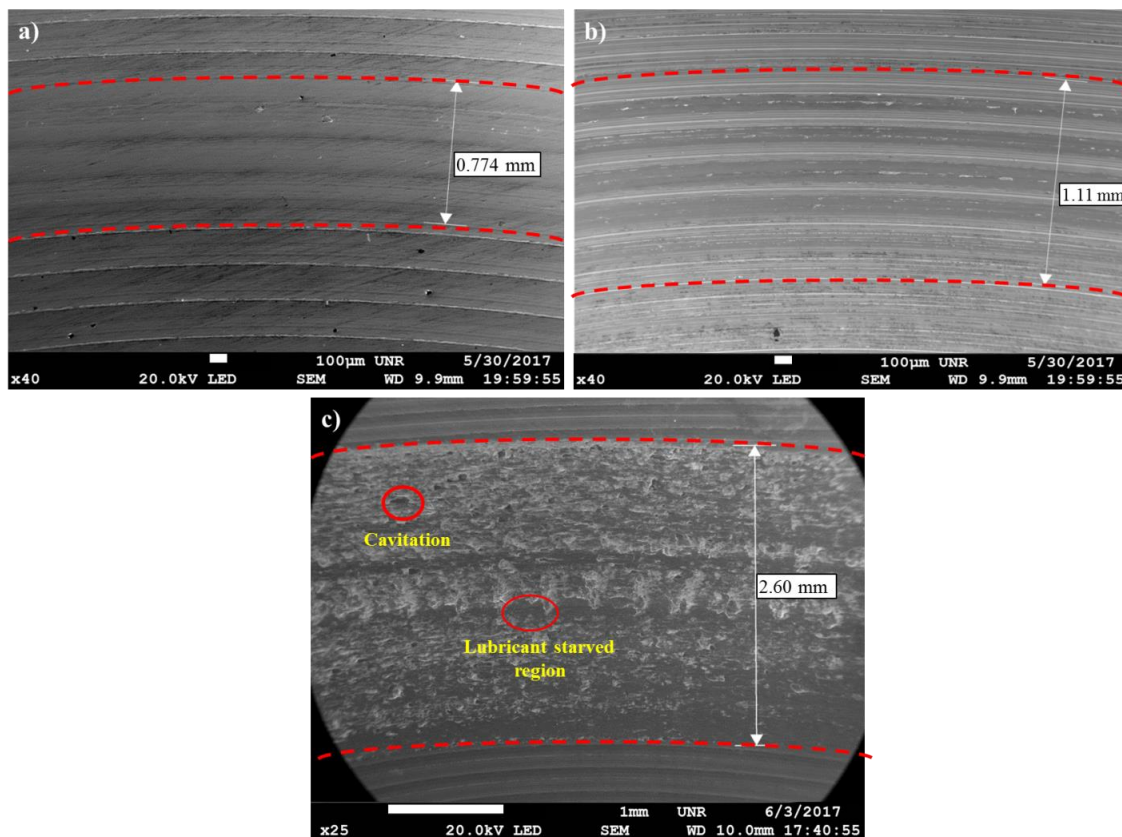
Figure 4.8: Wear track under SEM post tribocorrosion testing.

4.3.4. *Evolution of corrosion rate during tribocorrosion test*

In-situ Direct Current Corrosion tests were performed in parallel with the wear test for 15 hours in each of the oil mediums. During the DC corrosion testing the potential was continuously varied from anodic condition of +0.5 V potential vs. OCP (E_{OC}) to cathodic condition of +0.5 V potential vs. OCP (E_{OC}) at a scan rate of 0.167 mV/s and data being sampled every second. The three-electrode DC Corrosion test-rig shown in *Figure 4.2* was based on the potentiodynamic testing module. The sequential potentiodynamic test performed follows the quantitative corrosion theory which assumes that the rates of both anodic and cathodic processes are a function of the electron transfer reaction at the metal surface. The Butler-Volmer equation defining the opposing reactions in a corrosion system was used to determine the corrosion current (I_{corr}), Tafel constants and their respective Tafel curves (log I vs. E plot). The 15-hour tribocorrosion testing yielded 20 Tafel curves for each oil medium, from which the corrosion rates were calculated and plotted as a function of time as shown in *Figure 4.9*.

$$I = I_a + I_c = I_{corr}\left(e^{\frac{2.3(E-E_{OC})}{\beta a}} - e^{\frac{-2.3(E-E_{OC})}{\beta c}}\right)$$

where, I = measured cell current in amps; I_a = current resulting from anodic reactions; I_c = current resulting from cathodic reactions; I_{corr} = the corrosion current in amps; E = the electrode potential; E_{OC} = the corrosion potential in volts; β_a = the anodic beta Tafel constant; β_c = the cathodic beta Tafel constant.

It was observed during the tribocorrosion test that for the first 6 hours of wear the corrosion rate in Medium-I was minimal at 0.325×10^{-5} mm/year. After 6 hours of wear, it was observed that the corrosion rate moderately accelerates over the remainder of the test and increases to a maximum of 0.689×10^{-5} mm/year at the end of 12 hours of wear. The corrosion rate in Medium-II was similar to that in Medium-I for the first 6 hours of wear after which it linearly accelerates to a maximum of 1.792×10^{-5} mm/year at the end of 10.5 hours of wear. This acceleration in corrosion rate in Medium-II indicates the corrosive reaction of the salt contaminants with the wear debris. Since this increase in corrosion rate did not effectively vary either the COF or the wear rate shown in *Figure 4.6* and *Figure 4.7*, respectively, it can be attributed to the increase in the cell medium resistance that would have caused the anodic reactions to increase considerably. Hence,

tribocorrosion testing in Medium-II can be expected to yield a higher rate of wear over prolonged wear period that would progress beyond 15 hours when compared to Medium-I.
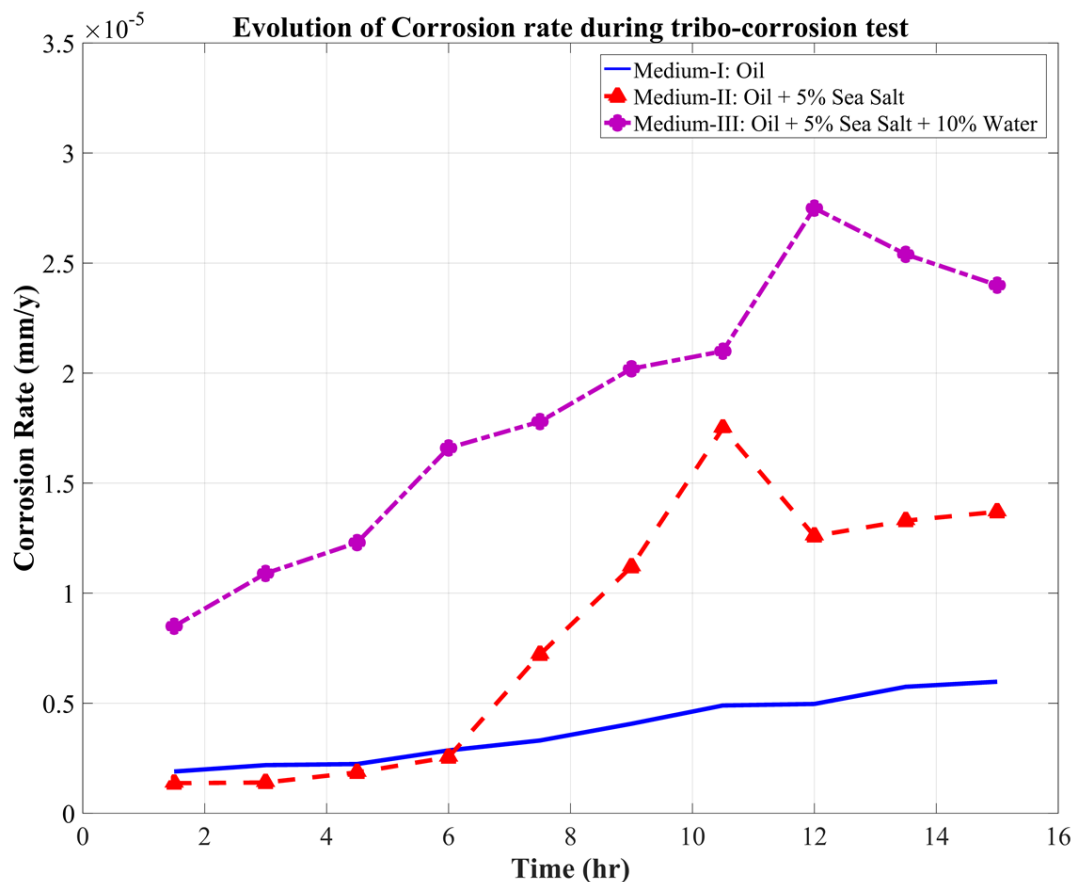
Figure 4.9: Evolution of corrosion rate during the tribocorrosion test.

Further, in *Figure 4.9* the corrosion rate of the sample in Medium-III was observed to linearly increase from the beginning of the tribocorrosion test. The corrosion rate increases from a minimum of 0.86×10^{-5} mm/year at the end of 1 hour of wear to a maximum of 2.58×10^{-5} mm/year at the end of 12 hours of wear. A spike in corrosion rate was observed to be initiated after 8 hours of wear that was also indicated by the test-rig as an increase in COF and wear rate around the same period. Medium-III which was contaminated with salt and water seems to have stabilized as a single contaminate consisting of aqueous NaCl which starts to corrosively react with the steel wear debris and wear track forming corrosion elements. The corrosion elements consisting of iron oxide along with the contaminants interfere with the sliding of tribo-pair causing cavitation, minor pitting and starved lubrication regions at the interface as observed in *Figure 4.8*(c). Evidently, this was also the point at which wear and corrosion synergism effect was the maximum because when the

corrosion tests were performed without wear the corrosion rate was fairly linear throughout for Medium-III as can be observed in *Figure 4.10.*
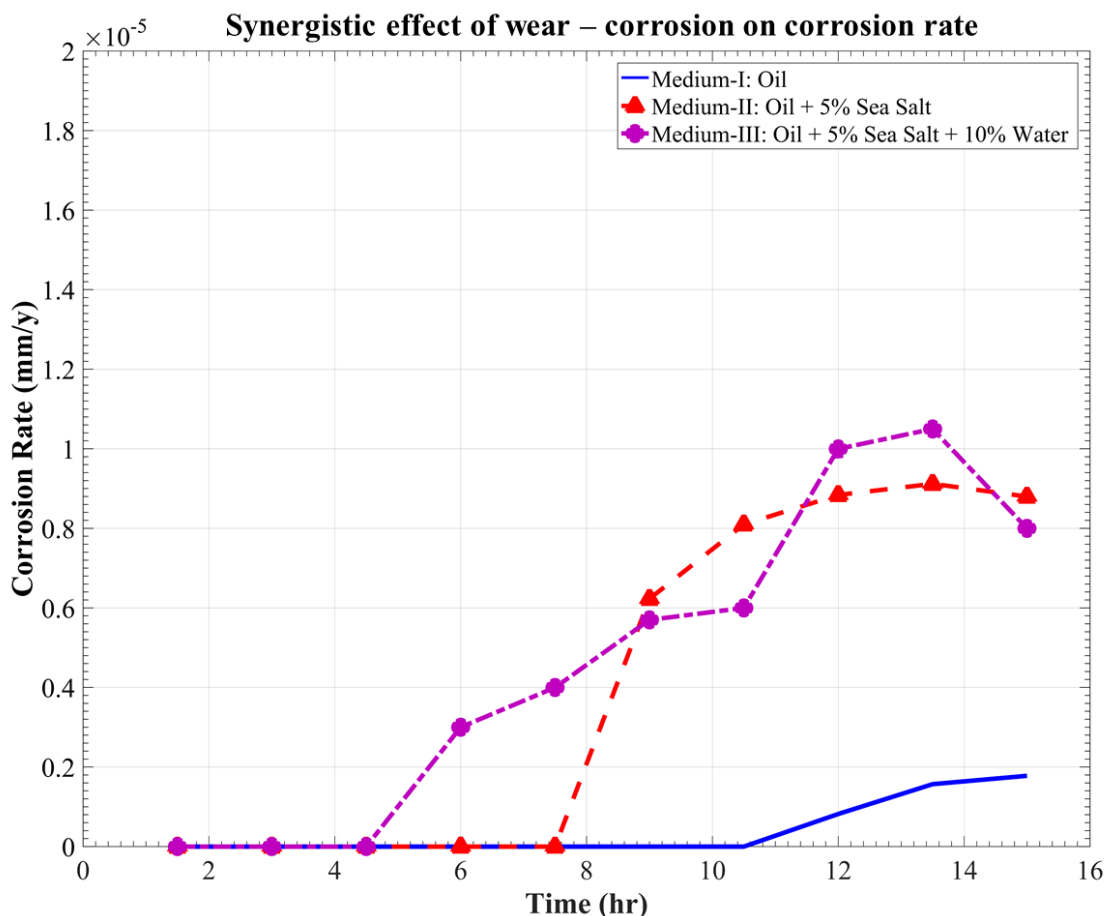
Figure 4.10: Synergistic effect of wear - corrosion on corrosion rate.

Comparing the corrosion rates shown in *Figure 4.9* and *Figure 4.10* the synergistic effect of wear-corrosion on corrosion rate was determined as shown in *Figure 4.11*. This gives a clear perspective on the synergistic effect of wear-corrosion in uncontaminated oil medium (Medium-I) and contaminated oil mediums (Medium-II and III). The synergistic effect of wear-corrosion on corrosion rate can be observed to have been initiated after 10.5 hrs, 7.6 hrs and 4.3 hrs of wear in Medium-I, II and III, respectively. There is also observed periods of acceleration in corrosion rates in Medium-II and Medium-III which are indicative of breaking down of oxide tribo-layers on the surface of the sample, wear debris and wear track. This is evidently the tribocorrosion phenomenon that causes the variations in OCP, corrosion rate, COF and wear rate. The test-rig design for

analyzing this phenomenon in oil mediums was found to be effective and consistent irrespective of the contaminants and time of testing period.
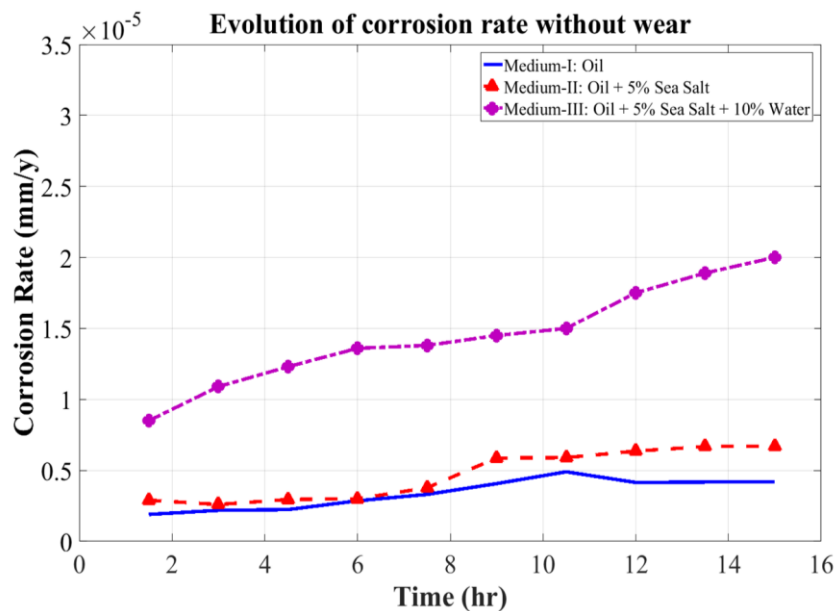
Figure 4.11: Evolution of corrosion rate without the influence of wear.

4.4.Conclusions

The current study was aimed at designing and analyzing a tribocorrosion test-rig which could effectively monitor the phenomenon in an oil medium. The study attempts to solve the prolonged ineffectiveness of tribocorrosion measurements in oil medium due to the design and cell medium limitations. It was found that during testing the kinetic nature of the oil medium causes moderate fluctuations in the reading which can be compensated by strategically aligning the reference and counter electrodes with the wear track and fluid flow. The test-rig design proves to be an effective method of monitoring wear and corrosion synergism in the oil medium, which can be in contaminated or uncontaminated conditions. The presented test-rig provides reliable and consistent in-situ data on COF and synergism of wear and corrosion. It was observed that the synergistic effect of wear and corrosion in an uncontaminated oil medium was negligible. Whereas, in the oil mediums that were contaminated with salt and water, the effect of tribocorrosion was very prominent. When the oil medium was contaminated with 5 wt.% salt, the effect of tribocorrosion on corrosion rate was observed after 7 hours, while in the oil contaminated

with 5 wt.% salt and 10 wt.% water, it was observed as early as 3 hours into the tribocorrosion test.

The in-situ oil monitoring system presented in the current study has a wide range of industrial applicability involving oil and lubricating systems such as transmission systems and engines in automobiles, pressure vessel cooling systems, wind turbines, heavy duty drills, and a variety of industrial machinery. Further, the system will enable better control and monitoring of over and under usage of lubricants which will reduce the overall oil waste output into our ecosystem. The LMS designed though this study is found to be a reliable method of investigating in-situ tribocorrosion behavior of functional surfaces in a dynamic lubricated environment. The LMS designed in this study will be used to investigate the tribocorrosion behavior of engineered surfaces and coatings in the subsequent chapters. The equipment has been able to test LSP surfaces and nanocomposite surfaces under various boundary conditions. These studies have been discussed in the following chapters.

Chapter 5: Characterization and tribological performance of engineered surfaces

The present study aims to characterize the effect of LSP on surface morphology and friction behavior of metallic surfaces, with a specific focus on the influence of laser intensity on surface roughness, coefficient of friction (COF), and transfer layer formation. As a result of this investigation, a surface behavior model describing the effect of laser intensity on surface morphology has been developed. The study also demonstrates the use of an effective surface modification technique to control the tribological properties of a surface.

5.1. Materials and methods

The experimental work design of the current study is schematically represented in *Figure 5.1*, and the materials and methods are detailed in this section.
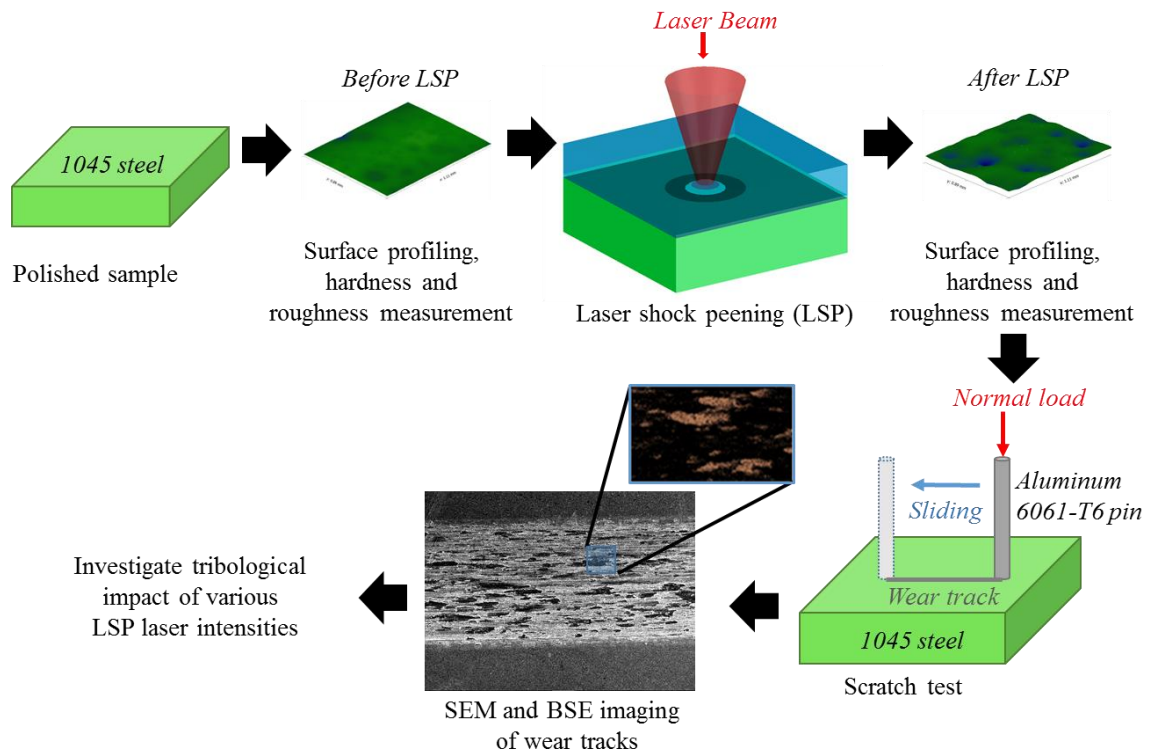
Figure 5.1: Experimental work scheme for tribological analysis of LSP treated surfaces.

5.1.1. Materials

High strength 1045 medium carbon steel (ASTM A108) of 30 mm × 12 mm × 10 mm were used as the plate material on which LSP was performed. In order to perform the scratch test on these steel plate surfaces, 6061-T6 aluminum alloy (ASTM B211) of 3 mm diameter was used as the counterpart pin material. The material composition and physical properties of the tribo-pair (pin and plate) are detailed in *Table 5.1*. The tribo-pair used in the present study has widespread applications in overhead power lines as Aluminum Conductor Steel-Reinforced cables (ACSR), electrical connectors involving aluminum connections with steel, aircraft fittings, marine fittings and hardware, valves and valve parts.

Table 5.1: Material composition and physical properties of 1045 medium carbon steel and 6061-T6 aluminum alloy.

Properties	1045 medium carbon steel (ASTM A108)		6061-T6 aluminum alloy (ASTM B211)	
Material Composition			Aluminum	95.1-98.2%
			Chromium	0.4-0.8%
	Iron	98.21-98.85%	Copper	0.05-0.4%
	Carbon	0.43-0.50%	Iron	0-0.7%
	Manganese	0.60-0.90%	Magnesium	0.8-1.2%
	Phosphorus	0-0.04%	Manganese	0-0.15%
	Silicon	0.15-0.30%	Nickel	0-0.05%
	Sulfur	0-0.05%	Silicon	0.4-0.8%
			Titanium	0-0.15%
			Zinc	0-0.25%
			Zirconium	0-0.25%
			Other	0.15%
Yield Strength	530 MPa		241.32 MPa	
Hardness	190HV0.5		107HV0.5	
Hardness rating	Medium		Soft	
Melting Point	1427 °C		582.22 °C	
Elongation	19		12.5 %	

5.1.2. LSP of steel surfaces

The initial preparation of the steel surfaces before LSP, involved rough polishing using sandpapers of grit sizes 100, 320, 600, 800 and 1200. This was followed by a fine wet polishing using 3 µm, 0.5 µm diamond slurry, and 0.06 µm colloidal silica suspension. Five steel specimen surfaces were polished in this manner to have an average surface roughness (S_a) of 0.1 ± 0.03 µm. After the initial surface preparation, the LSP was performed on four steel specimen surfaces at specific laser intensities, as indicated in *Table 5.2*. The remaining one untreated steel surface was considered as the reference surface. The LSP was performed using a nanosecond pulsed Nd-YAG laser with a wavelength of 1064 nm and a pulse duration time (t) of 5 ns. The laser beam diameter (d) was maintained at 1.5 mm. A black tape with a thickness of 0.132 µm and BK7 (borosilicate) glass were used as the ablative coating and confinement media, respectively. The black tape was carefully peeled off after processing, and the specimens were cleaned in an ultrasonic cleaner using N-hexane solution to remove the adhesive remnants of the black tape. Further, the specimens were ultrasonically cleaned in soap water and acetone before being stored in a desiccator.

Table 5.2: LSP process parameters for different specimens.

Specimen Number	Laser Intensity, I (GW/cm^2)
#1 (untreated)	0
#2	1.68
#3	3.46
#4	4.40
#5	6.00

5.1.3. Surface Characterization

The surface topography of each specimen was characterized before and after the LSP using Rtec 3D optical profilometer which has a resolution of 50 nm. As an example, the surface profiles before and after the LSP processing is shown in *Figure 5.2*. An area of 1.11×0.89 mm^2 was profiled at five random locations on the sample surface, and an average of these roughness value has been reported. During this surface characterization, various 3D surface roughness parameters were recorded to investigate the surface morphological changes due to LSP. Further, Vickers microhardness test (HV) was conducted to study the effect of LSP on the surface hardness. The HV values were measured using a diamond tip indenter with a load of 500 g and a dwell time of

10 s. The hardness value of the untreated specimen was considered as the baseline, against which the hardness of LSP treated samples were compared and analyzed.

(a) Before LSP

(b) After LSP

$Sa = 0.102\ \mu m$

$Sa = 0.0673\ \mu m$
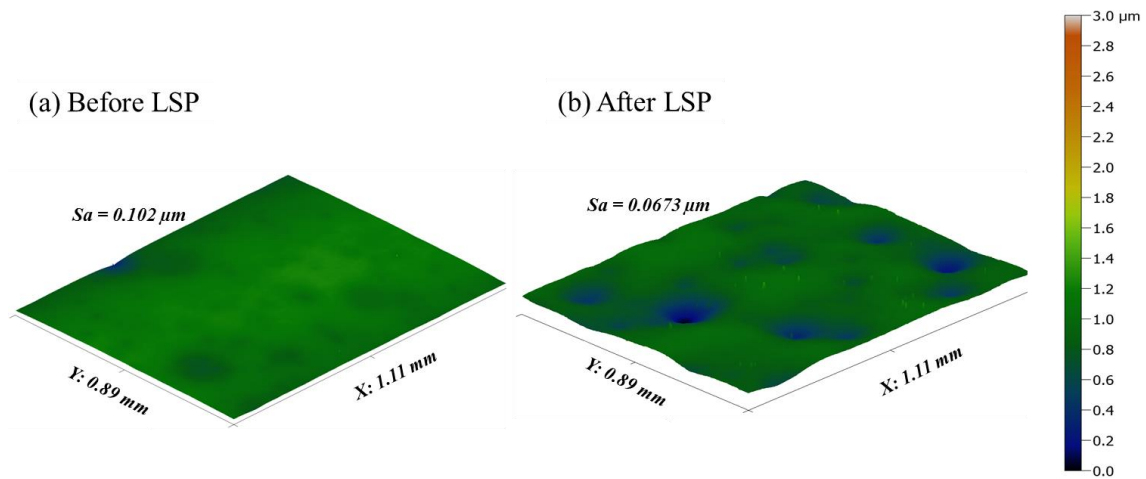
Figure 5.2: 3D-Surface topography (a) Before LSP (b) After LSP at I = 1.68 GW/cm^2.

5.1.4. Tribological performance

The tribological properties, such as friction, and transfer layer formation were investigated using a scratch test. The scratch tests were performed as per ASTM G133 on each of the five steel surfaces (four LSP treated and one untreated surface) using aluminum alloy pins as shown schematically in *Figure 5.3*. The scratch tests were performed using a Rtec multi-function tribometer 5000 which is equipped with a high-resolution 1D normal force load cell (15 mN resolution) and a 1D friction force load cell (6 mN resolution). The test conditions for the scratch experiments are detailed in *Table 5.3*. These test conditions were determined based on previous investigations that considered similar applicability of the steel substrate [192, 193]. Before each test, the pin and steel surface was thoroughly cleaned in an aqueous soap solution followed by ultrasonic cleaning in acetone. The repeatability and consistency of the results were verified by performing each scratch test three times.

Table 5.3: Scratch test conditions.

Experiment parameters	Values
Specimen surface condition	Dry
Temperature	24 °C
Humidity	30% RH
Load (constant)	50N
Sliding Distance	10 mm
Sliding speed	2 mm/s
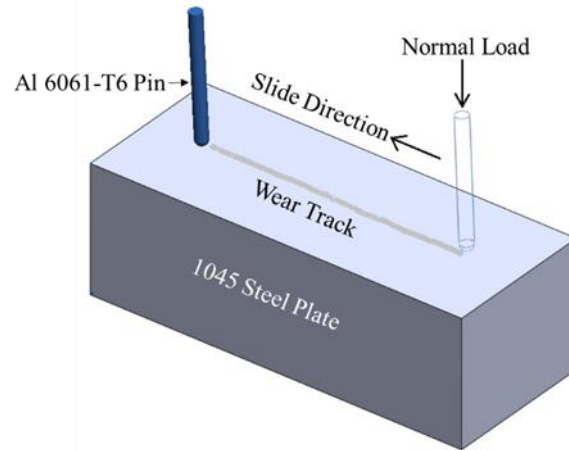
Figure 5.3: Schematic diagram of the scratch test when Al 6061-T6 pin slides against 1045 steel plate.

After the tests, scanning electron microscope (SEM) was used to analyze the transfer layer formation on the steel surfaces. Backscattered scanning electron microscopy (BSE) coupled with energy dispersive spectroscopy (EDS) was used to obtain data on the composition of the transfer layer formed on the wear tracks. Furthermore, the wear tracks were phase mapped to quantify the amount of aluminum transfer layer formed on the steel surfaces.

5.2. Results and Discussion

5.2.1. Surface Roughness

The 3D surface roughness profiles were recorded before and after LSP of each steel surface. The roughness parameters of the profile that are discussed in this study have been described in detail by Menezes et al. [194]. The surface roughness parameters discussed in this study are – average surface roughness (R_a, S_a), root mean square surface roughness (R_q, S_q), skewness (R_{sk}, S_{sk}), kurtosis (R_{ku}, S_{ku}), average maximum height of valley depth (R_{vm}) and peak height (R_{pm}), average maximum height of the profile (R_z), average wavelength of the profile (λ_a), and average absolute slope (Δ_a). Among the various surface roughness parameters investigated in the present study, it was found that the skewness (S_{sk}) and the kurtosis (S_{ku}) roughness values were significantly affected by the change in laser intensity of the LSP as shown in *Figure 5.4*. The figure shows the observed change in surface roughness amplitudes due to LSP when compared against the most commonly used surface roughness parameters- average surface roughness (S_a) and RMS surface roughness (S_q). It can be observed that as the laser intensity increases, the S_a and S_q show a variation < 0.2, while S_{sk} shows a variation ranging between 0.89 to 2.86 (42.18 % to 188%) and

S_{ku} shows a variation ranging between 1.9 to 3.32 (61.09% to 92.46 %). The S_{sk} and S_{ku} values at each laser intensity of the LSP has been tabulated in *Table 5.4*. These variations in 3D roughness values indicate that the traditional methodology of quantifying the changes in surface roughness after the LSP using S_a and S_q [107, 108, 134] is insufficient to describe the changes in surface morphology. It was found that the effect of LSP on surface roughness can be quantified appropriately by using more than one roughness parameter [109, 111, 195, 196]. The roughness parameters S_{sk} and S_{ku} are found to be a good representation of the changes in surface roughness as a function of laser intensity.

Table 5.4: 3D Skewness and Kurtosis amplitudes before and after LSP processing.

Laser Intensity (GW/cm²)	3D Skewness (S_{sk})			3D Kurtosis (S_{ku})		
	Before LSP	After LSP	Change due to LSP	Before LSP	After LSP	Change due to LSP
$I_1 = 0$	-1.22	-1.22	0.00	3.08	3.08	0
$I_2 = 1.68$	-2.11	-1.21	0.89	3.11	1.21	1.90
$I_3 = 3.46$	-1.80	-0.22	1.57	3.67	0.59	3.08
$I_4 = 4.40$	-2.08	0.34	2.43	3.58	0.26	3.31
$I_5 = 6.00$	-1.52	0.76	2.86	3.59	0.81	2.78
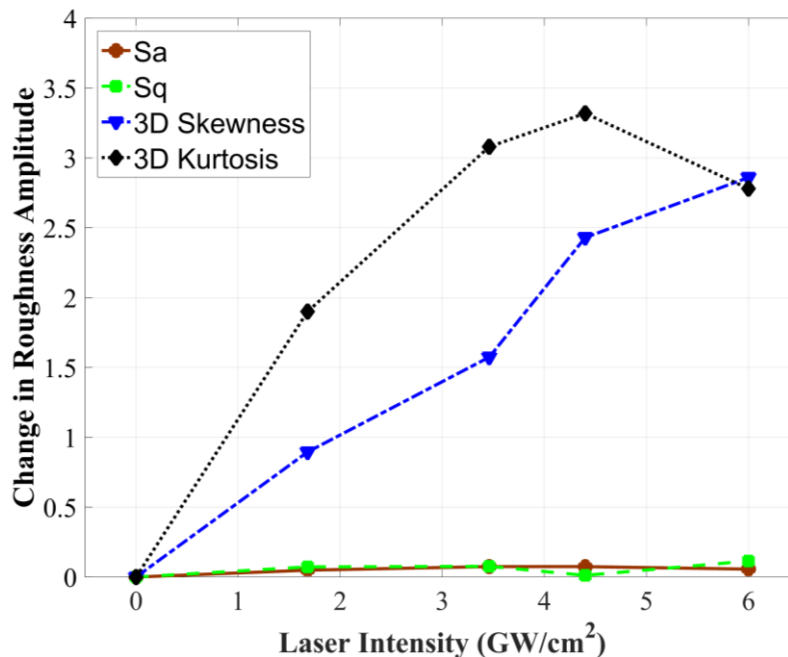
Figure 5.4: Change of various roughness parameters as a function of laser intensity.

5.2.2. Surface Profile

Investigations were performed to analyze the effect of laser intensity on the surface profile of the LSP treated steel surfaces as shown in *Figure 5.5*. The *Figure 5.5*(a) shows 2D surface profile of the untreated steel surface ($I_1 = 0$ GW/cm^2) while the *Figure 5.5*(b-e) represent the 2D surface profiles of steel surfaces treated at various laser intensities ($I_2 = 1.68$ GW/cm^2, $I_3 = 3.46$ GW/cm^2, $I_4 = 4.4$ GW/cm^2, and $I_5 = 6.0$ GW/cm^2). It can be clearly observed that as the laser intensity increases the asperities are accordingly compressed to be closer to the mean surface line of the profile. This indicates that there is a negative skewing effect on the surface profile as the laser intensity increases. It can be observed in *Figure 5.5*(b) and (c) that for lower intensity treatments
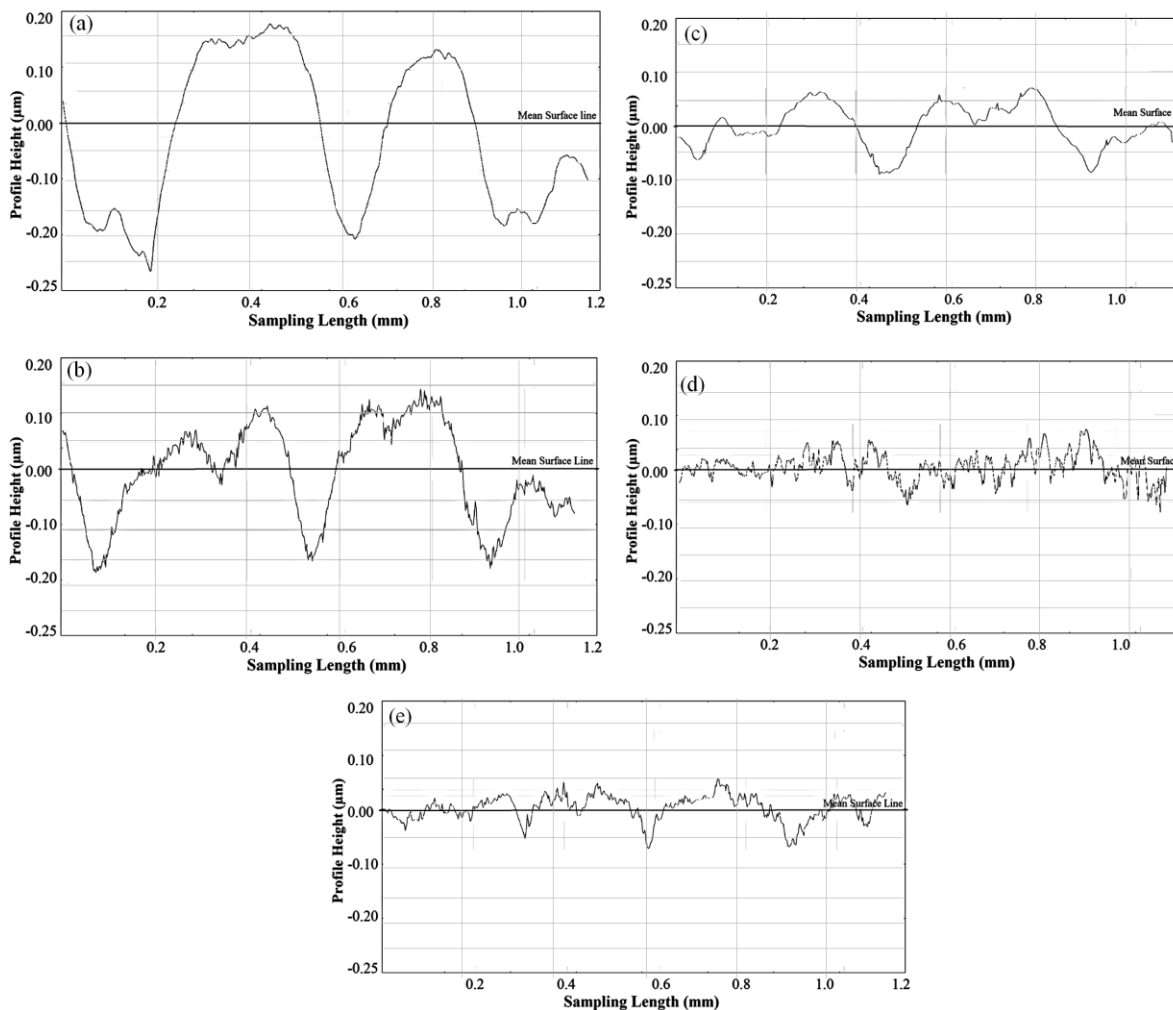
Figure 5.5: Effect of laser intensity on surface profile: (a) Untreated Surface ($I1 = 0$ GW/cm^2) (b) LSP at $I2 = 1.68$ GW/cm^2 (c) LSP at $I3 = 3.46$ GW/cm^2 (d) LSP at $I4 = 4.4$ GW/cm^2 (e) LSP at $I5 = 6.0$ GW/cm^2.

a platykurtic form of asperities with a low degree of sharpness was formed. Whereas, in case of high laser intensity treatment seen in *Figure 5.5*(d) and (e) symmetric-small sharp asperities were formed. Compared to the untreated surface profile seen in *Figure 5.5*(a) the asperities are observed to undergo a progressively increasing degree of plastic deformation as a function of laser intensity.

The observed changes in the asperity profiles are better understood when analyzed with their respective laser shockwave pressures during the LSP. The laser shockwave pressure as a function of time observed at each laser intensity treatment is shown in *Figure 5.6*. The peak pressures were calculated using the relationship between the laser intensity (I), and the laser shock peak pressure (P) which is expressed as:

$$P = 0.01 \sqrt{(\alpha/2\alpha + 3) \times Z \times I}$$

where α is the efficiency of the interaction, Z is the combined shock impedance defined as:

$$Z = 2/((1/Z_1) + (1/Z_2))$$

where Z_1 and Z_2 are the shock impedance of the material and the confining media, respectively. The estimations shown in *Figure 5.6* are based on the well-accepted LSP model proposed by Fabbro et al. [197]. It can be observed that as the laser intensity is increased from 1.68 to 6.0 GW/cm^2, the laser shockwave peak pressure increases from 2.9 to 5.6 GPa. This laser shockwave pressure introduces a compressive loading effect on the asperities leading to the observed surface plastic deformation. The gradient of asperity restructuring at various laser intensities can be
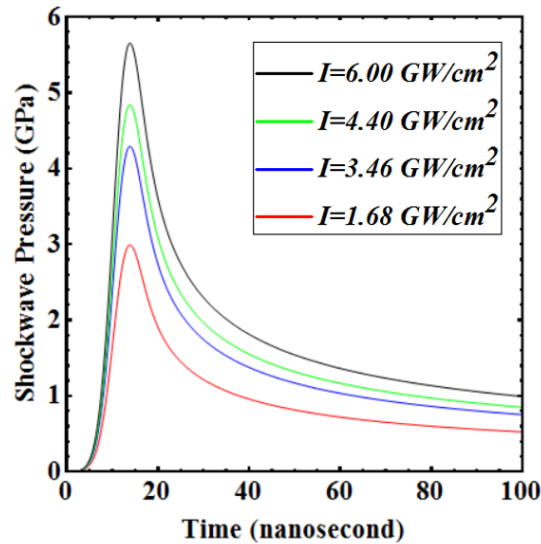
Figure 5.6: Laser shockwave pressure as a function of time with respect to different laser intensities.

attributed to the magnitude of laser shock loading during the LSP. At low laser intensity treatments, there was a low gradient of the shockwave pressure that generated asperities with a platykurtic form of peaks having low sharpness. Whereas, at high laser intensities a larger gradient of the shockwave pressure was observed resulting in a high degree of surface plastic deformation that generates sharp asperities [106].

5.2.3. Friction behavior

The effect of LSP on the COF is shown in *Figure 5.7*. It can be observed that as the laser intensity increases there is a decrease in the COF. The untreated steel surface exhibits a COF of 0.4, and as the laser intensity increases to 4.4 GW/cm^2 the COF decreases to 0.067. Upon further increasing the laser intensity to 6.0 GW/cm^2, the magnitude of COF increases to 0.112. Depending on the applied laser intensity the COF can be reduced by 17.5% - 83.25% with reference to the untreated steel surface. This decrease in the COF due to LSP can be attributed to the changes in surface morphology discussed in section 3.1. As observed in *Figure 5.5*, the process of LSP causes deformation and restructuring of the asperities depending on the applied laser intensity. *Figure 5.5*(a) which corresponds to the untreated steel surface exhibits a COF of 0.4, and when the surface was treated with a laser intensity of 1.68 GW/cm^2 the COF decreased by 17.5%. This can be attributed to the plastic deformation of asperities due to LSP which results in smaller peaks and valleys as compared to the untreated steel surface. Similarly, as the laser intensity was further increased to 3.46 GW/cm^2 (*Figure 5.5*(c)) and 4.4 GW/cm^2 (*Figure 5.5*(d)) the asperity size decreased to create a surface of platykurtic form with low sharpness. At these two laser intensity treatments, the COF was observed to decrease by 50 % and 83.25 %, respectively. It is also
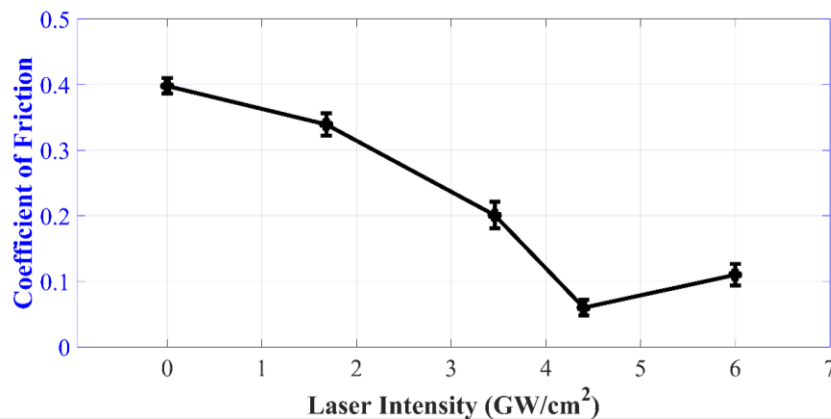
Figure 5.7: Effect of laser intensity on the coefficient of friction.

important to note that as the laser intensity increased there was a decrease in the peak-valley distance relative to the mean surface line and this distance was minimal when treated at 4.4 GW/cm^2. Similar effects of LSP have been indicated by Prabhakaran et al. [198] and Trdan et al. [199].

Further, when the laser intensity was increased to 6.0 GW/cm^2 the COF was found to increase to a value of 0.112 as compared to a COF of 0.067 at 4.4 GW/cm^2. This change in the COF can be attributed to the change in surface morphology from a valley dominant profile to a peak dominant profile with small asperities (*Figure 5.5*(e)). It can be observed that more sharp peaks are formed due to the high-density plastic deformation of asperities during LSP at 6.0 GW/cm^2. This observation corresponds to the change in kurtosis values for the surface treated at 6.0 GW/cm^2 as seen in *Table 5.4*. The surface treated at 6.0 GW/cm^2 exhibits a higher kurtosis value of 0.81 as compared to 0.26 for 4.4 GW/cm^2.

The observed trend in COF as a function of laser intensity indicates that the COF for a given surface can be precisely varied using LSP. In order to understand the relevance of the observed change in COF, the results from the present study have been compared with other similar studies and are shown in *Table 5.5* [47, 200-202]. It is to be noted that, even though similar laser intensity treatments have been considered in these studies, the material properties and tribological test parameters (such as load, velocity, and surface roughness) vary. It is also important to note that the other studies listed in *Table 5.5* did not consider the effect of surface morphology on the COF. The present work was able to achieve the lowest COF when the 1045 steel surface was treated at laser intensities of 4.4 and 6.0 GW/cm^2. This study demonstrates that it is possible to identify an optimum laser intensity which would produce a surface morphology that exhibits a low COF during sliding. Hence, it is necessary to consider the effect of surface morphology in defining the tribological behavior of LSP surfaces.

Table 5.5: Comparison of the coefficient of friction values before and after LSP processing.

Materials	LSP parameters	COF before LSP	COF after LSP	Reference
Ti6Al4V	4.25 GW/cm^2	0.435	0.451	[200]
Ti6Al4V	10 W, 5 mm/s	0.92	0.22	[201]
Al 6061-T6	5.3 GW/cm^2	1.0	1.3	[202]
100Cr6 rolling steel	5.5 GW/cm^2	0.55	0.45	[47]
AISI 1045 steel	4.4 GW/cm^2	0.40	0.067	Present work
	6.0 GW/cm^2	0.40	0.12	

5.2.4. Transfer layer formation

The wear tracks observed after the scratch tests at various laser intensities are shown in *Figure 5.8*. These wear tracks were analyzed under SEM to investigate the morphology of transfer layer formation.
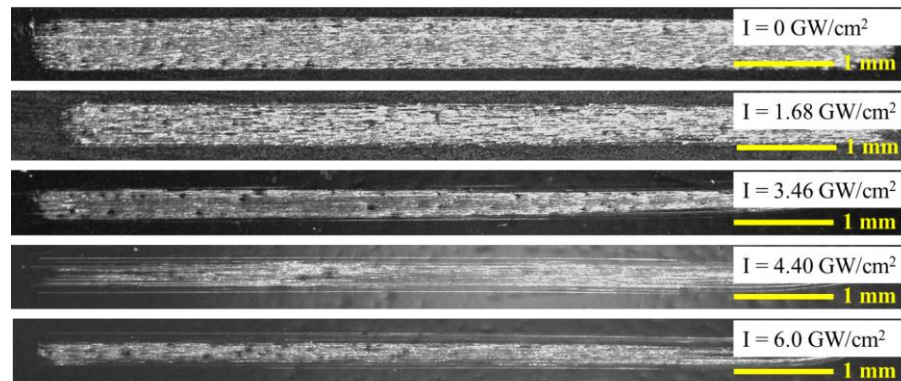
Figure 5.8: Wear track on steel surfaces treated at various laser intensities.

The BSE coupled with phase mapped EDS images of wear tracks are shown in *Figure 5.9*. The figure shows aluminum transfer layer formed during scratch test along the wear tracks. It can be observed that as laser intensity increases there is a significant reduction in the amount of transfer layer formed on the wear tracks. Though *Figure 5.9* represents a small section of the wear track, phase mapping was performed on the entire length of the wear track to quantify the exact amount of aluminum transfer layer. The observed trend in transfer layer formation was compared with the corresponding COF values and laser intensities as shown in *Figure 5.10*. It can be observed that the weight percentage of aluminum transfer layer as a function of laser intensity exhibits a similar trend as the COF. This indicates that the change in surface morphology due to LSP not only decreases the COF but also reduces the amount of transfer layer formed on the steel surfaces. The untreated steel surface exhibits a transfer layer of 17%, and as the laser intensity increases to 4.4 GW/cm^2 the transfer layer decreases to 5.4%. This is due to the small asperities formed during LSP at 4.4 GW/cm^2 which reduces the amount of shear stresses experienced by the asperities at the tribo-pair interface. This in-turn results in low weight percentage of transfer layer formation. Upon further increasing the laser intensity to 6.0 GW/cm^2, the transfer layer increases slightly, to 6.5%. At this laser intensity, small asperities with sharp peaks can be observed which increases the plowing effect by the asperities at the contact interface and thus increases the transfer layer formation. It can also be inferred that the same mechanism leads to a 67.2% increase in the COF at LSP of 6.0 GW/cm^2 as compared to the COF at 4.4 GW/cm^2.

Phase mapped EDS Image   Backscattered SEM
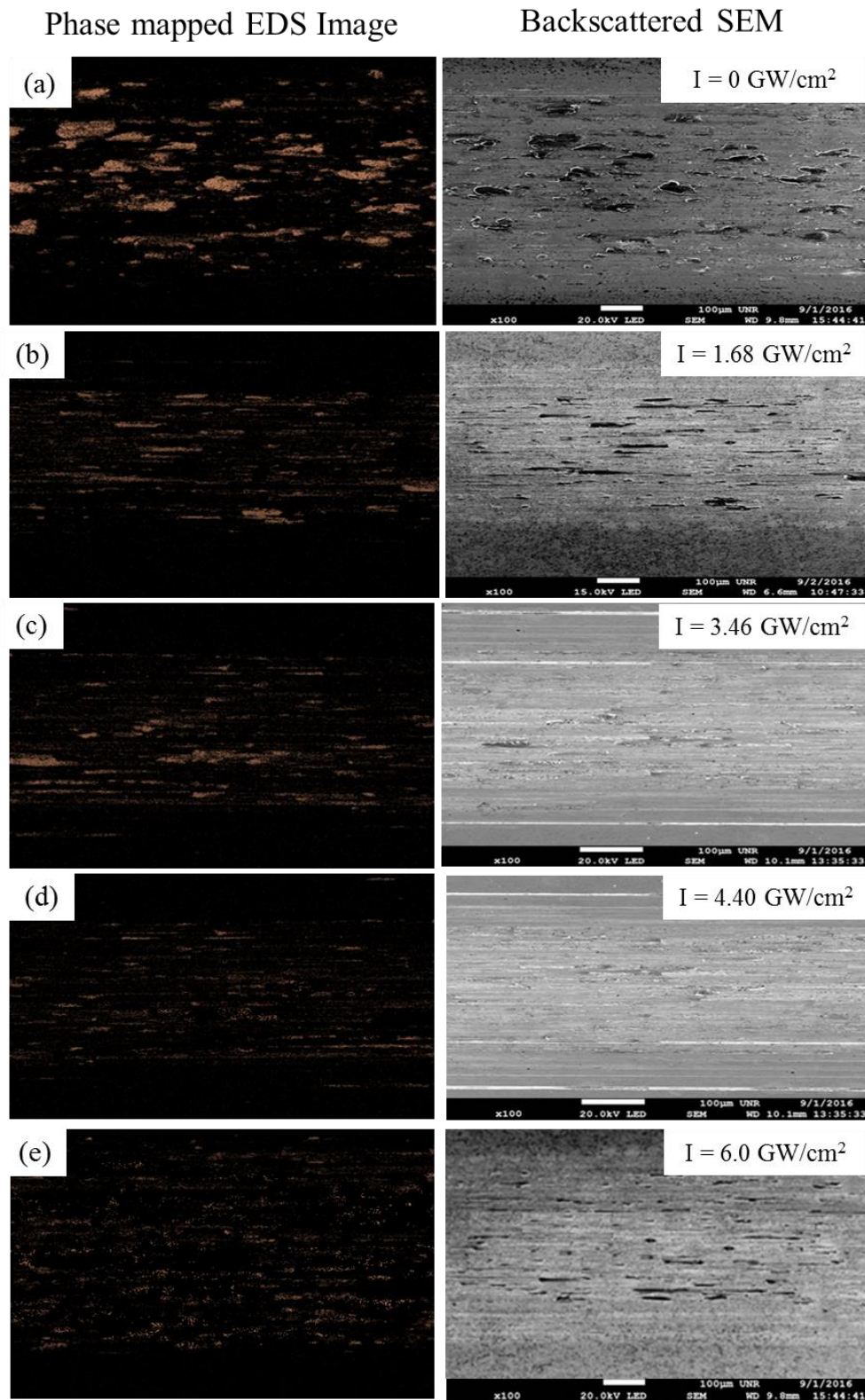
Figure 5.9: SEM backscattered images coupled with phase mapped EDS images of Al transfer layer formed on Laser Shock Peened surfaces at laser intensities of (a) I = 0 GW/cm^2 (untreated surface); (b) I = 1.68 GW/cm^2; (c) I = 3.46 GW/cm^2; (d) I = 4.4 GW/cm^2; (e) I = 6 GW/cm^2.
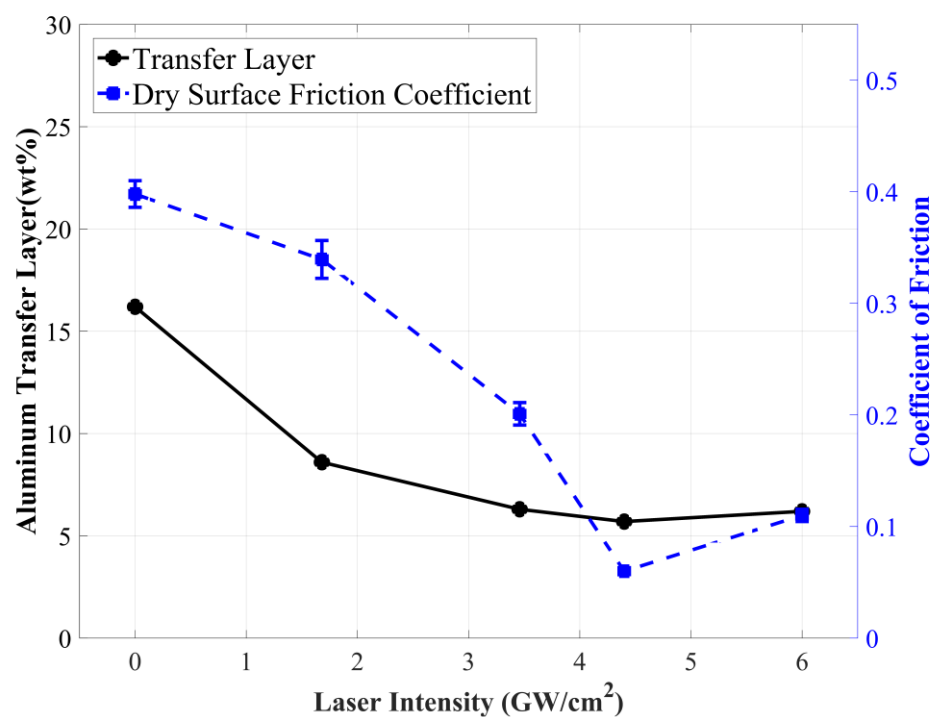
Figure 5.10: Effect of LSP on wt% percentage of Al transfer layer formation compared with COF.

5.2.5. Surface hardness

Microhardness tests were carried out on LSP surfaces to investigate the surface strengthening effect by the LSP. It was found that the surface hardness increases progressively with laser intensity as shown in *Figure 5.11*. This is mainly attributed to the strain hardening effect introduced by the LSP [51-54]. Even though it is intrinsic for the COF to decrease as the hardness of the surface increases, an 83.25% drop in COF cannot be attributed only to the change in surface hardness. It can be observed in *Figure 5.11* that when the laser intensity was increased from 0 to 1.68 GW/cm^2, the COF decreased from 0.4 to 0.33 (17.5% decrease) with an increase in the surface hardness from 190 to 225 HV (18.4% increase). Increasing the laser intensity from 1.68 GW/cm^2 to 4.4 GW/cm^2 lead to a decrease in COF from 0.33 to 0.067 (79.7% decrease) and an increase in the surface hardness from 225 to 234 HV (4% increase). When the laser intensity was further increased from 4.4 GW/cm^2 to 6.0 GW/cm^2, the COF increased from 0.067 to 0.112 (67.2% increase), respectively. Additionally, for the same increase in laser intensity (4.4 GW/cm^2 to 6.0 GW/cm^2) the surface hardness increased by only 4 HV (1.71% increase), which is negligible as

compared to the observed increase in COF. This indicates a dominant effect of the surface roughening at higher laser intensities. Similar roughening effects at high laser intensity treatments have been recently reported [198]. These results indicate that for a low laser intensity range of LSP, both surface strengthening and roughening effects contribute to the decrease in COF. Whereas, for a high laser intensity range of LSP, the surface strengthening effect reaches a saturation point and the surface roughening will have a dominant effect on the COF.
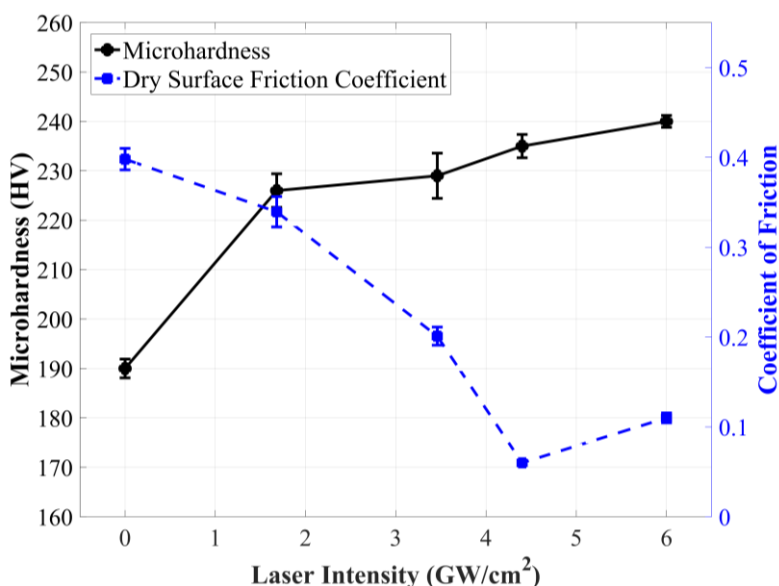
Figure 5.11: Effect of LSP on surface hardness compared with COF.

5.3. Surface behavior model

The effect of laser intensity on the surface profile as was shown in *Figure 5.5* indicated that the surface morphology varies with laser intensity. Additionally, the formation of transfer layer during sliding also varied as a function of the applied laser intensity (*Figure 5.9*). Based on these findings and the observed COF, a surface behavior model for LSP treated surfaces was developed as shown in *Figure 5.12*. The model represents a direct proportionality between the laser intensity and change in surface morphology due to plastic deformation of asperities. At low laser intensities, the asperity peaks were found to be plastically deformed ("squashed") reducing the overall kurtosis (sharpness) of the surface profile. As a result, the surface experienced a lower shear force during sliding leading to a 17.5% decrease in COF as compared to the untreated surface. When the surface was treated at an optimum laser intensity, the asperities undergo plastic deformation to yield a

profile with minimum kurtosis and skewness. This optimum change in surface morphology minimizes the shear force during sliding providing an 83.5% decrease in COF as compared to the untreated surface. At high laser intensities, the asperities undergo extreme plastic deformation leading to a restructuring of the asperities. This results in small-sharp asperities on the surface. Even though, the surfaces treated at high and optimum laser intensities experience a low shear force due to small asperities, the sharp asperities on surface treated at high laser intensity lead to a 67.2% increase in COF as compared to the surface treated at optimum laser intensity. This can be
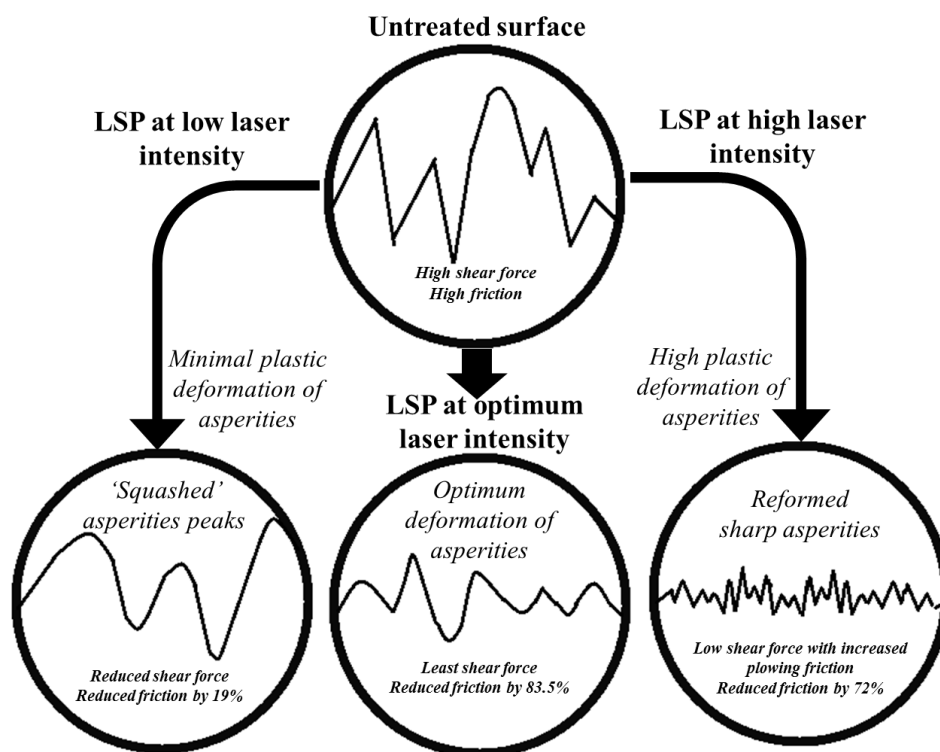
Figure 5.12: Surface texture model for laser shock peening at various laser intensities.

attributed to the increase in plowing effect as a result of the sharp asperities on the surfaces treated at high laser intensities. The high laser intensity treated surface can still provide a 72% decrease in COF as compared to the untreated surface. This behavior of friction with respect to the laser intensity and surface morphology indicates that COF can be controlled using appropriate laser intensity to suitably modify the surface morphology.

The present study shows that LSP can be used as an effective surface modification tool to enhance not only the wear resistance and surface hardness but also to control the friction behavior of the surface. The study also shows that a fundamental understanding of the friction behavior and

surface morphology for LSP treated surface is necessary to maximize the effectiveness of the surface modification technique.

5.4. Conclusions

The present study aimed to investigate the effects of LSP on the tribological properties of the steel surfaces. More specifically, the study investigated the effects of laser intensity on the surface roughness, surface profile, COF, transfer layer formation, and surface hardness. The study also investigated the interdependence of surface morphology and COF followed by interdependency of surface morphology and surface hardness to clearly discern the effects of LSP. Some of the major findings of the study are as follows:

- The roughness parameters S_{sk} and S_{ku} were found to be good representations of the changes in surface roughness as a function of laser intensity.

- The gradient of restructuring the asperities at various laser intensities was attributed to the magnitude of laser shock loading during LSP.

- At low laser intensity treatments, there was a low gradient of the shockwave pressure that generated asperities with a platykurtic form of peaks having low sharpness, whereas, at high laser intensities a lager gradient of the shockwave pressure was observed resulting in high degree of surface plastic deformation with sharp asperities.

- Depending on the applied laser intensity, the COF can be reduced by a range of 17.5% - 83.25% with reference to the untreated steel surface.

- The change in surface morphology due to LSP not only decreases the COF but also reduces the amount of transfer layer formed on the steel surface.

- The aluminum transfer layer formation as a function of laser intensity exhibits a similar trend as the COF.

- The observed trend in COF as a function of laser intensity indicates that the COF for a given surface can be precisely varied using LSP.

- For a low laser intensity range of LSP, both surface strengthening and roughening effects contribute to the decrease in COF.

- For a high laser intensity range of LSP, the surface strengthening effect reaches a saturation point and the surface roughening will have the dominant effect on the COF.

With the understanding of the surface roughness and tribological behavior of LSP surfaces, the following chapter investigates the tribocorrosion behavior of LSP surfaces.

Chapter 6: Tribocorrosion of engineered surfaces

Laser shock peening (LSP) is one of the widely used surface processing technique for tailoring functional behavior of the surfaces. However, understanding of LSP treated surfaces involving tribological contacts in electrochemically active environments is limited because the mechanism of wear-corrosion interactions (tribocorrosion) for such surfaces is still unclear. In the present study, the effect of LSP surface processing on wear-corrosion behavior of AZ31B Mg alloy was investigated. Specifically, the study investigates the changes in surface roughness, microhardness, friction, wear, and tribocorrosion during sliding in 3.5% NaCl solution. The study provides qualitative insight into the wear-accelerated corrosion mechanism for LSP at various laser intensities. The study finds that the LSP processing can decrease the corrosion potential difference between worn and unworn regions of the surface, thereby mitigating the effect of wear-accelerated corrosion during sliding. The effect of wear-accelerated corrosion was evident from the change in average surface roughness (S_a) of the unworn areas. It was found that understanding the change in surface roughness due to wear-corrosion interactions is necessary to investigate the onset and propagation of corrosion. Based on these results, the study details the mechanism of wear-corrosion interactions during sliding.

6.1. Materials and methods

Mg alloys are lightweight with exceptional ductility that is widely used in the fields of automobiles, aerospace, and manufacturing. They possess unique features where they can be easily recycled without affecting their material and mechanical properties. Today, these alloys are being used as intelligent product solutions and commercial application solutions. More specifically, the tribological applications involve Mg alloys being subjected to sliding in automotive brakes, engine piston, and cylinder bores where they encounter other materials, such as Al alloys. In order to make these tribo-contact interfaces functionally resistant to wear and enhance the surface mechanical properties, they are sometimes processed using LSP. Further, friction and wear along with the understanding of electrochemical behavior of Mg alloys are of interest in the processing using extrusion, forming, and rolling. Hence, understanding the tribological and tribocorrosion behavior of functionally processed Mg alloy surfaces are of practical and theoretical importance.

6.1.1. Materials and electrolyte

In this investigation, a rolled AZ31B Mg alloy block purchased from Metalmart.com was used for the experiments. Square plate samples with a 1-inch width and 0.5-inch thickness were cut from the block for LSP processing. Before LSP, the surface of the samples was ground using SiC sandpapers with different grit numbers (from 320 to 1200), followed by fine polishing using 3-micron diamond suspension. The counter material for the tribocorrosion testing was a non-conductive ceramic material, alumina ball of 6.35 mm diameter. The present tribocorrosion study simulates a corrosive lubricated environment according to ASTM B895-99, where 3.5% NaCl solution is used as the electrolyte/lubricant.

6.1.2. LSP of AZ31B Mg alloy surfaces

A Q-switched Nd-YAG laser (Surelite III from Continuum, Inc.) operating at a wavelength of 1064 nm and a pulse width of 7 ns (full width at half maximum), was used to deliver the laser energy. The laser beam size was 0.0025 m. BK7 glass and black tape with a thickness of 130 µm were used as confinement and ablative coating, respectively. Laser power intensity was varied by adjusting the Q-switched delay time [40]. Five laser intensities were used in this study along with untreated surface conditions as detailed in *Table 6.1*.

Table 6.1: Laser intensities used for LSP processing of AZ31B Mg surfaces.

Surface processing	Laser Intensity (GW/cm^2)
Untreated	0
LSP-1	0.47
LSP-2	0.87
LSP-3	1.36
LSP-4	1.76
LSP-5	2.22

At each laser intensity, a surface area of 17×7 mm^2 was processed with LSP. It was only this LSP processed area that was exposed to the electrolyte/lubricant during the tribocorrosion test. A schematic of the LSP processing method on AZ31B Mg material is illustrated in *Figure 6.1*.
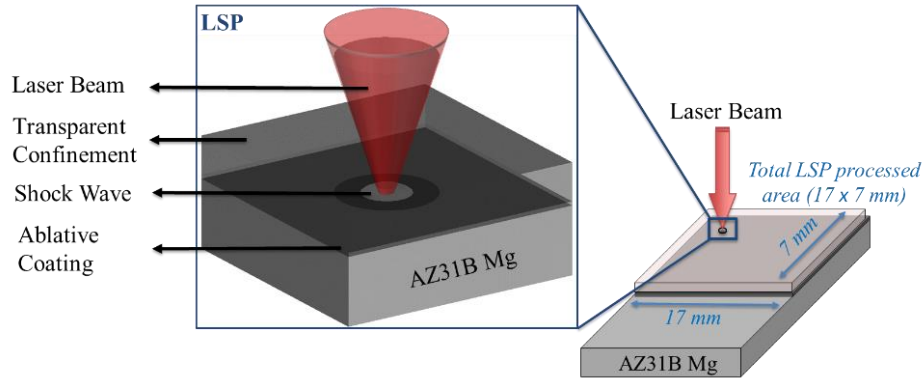
Figure 6.1: Schematic of LSP and LSP processing area of AZ31B Mg alloy surface.

6.1.3. Surface analysis and microhardness test

The surface roughness profiles, and roughness parameters were recorded for each Mg sample before and after LSP to determine the effect of laser intensity on the surface roughness. Additionally, the same was recorded after the tribocorrosion testing on the surfaces. A white light 3D optical profilometer (Rtec) was used to record these surface profiles and roughness data. In-depth hardness was measured from the top surface to a depth of 600 μm using a Wilson Hardness tester with a 500 g load and 10 s dwell time. The surface roughness and hardness values are reported along with their respective standard deviations calculated over three repetitions. During each tribocorrosion test, the linear wear loss was recorded by measuring the vertical displacement of the pin from the surface due to rubbing. The linear displacement of the pin (having a hemispherical cross-section profile) was converted into a volumetric wear loss using equation derived from the geometry of a spherical tip:

$$V = \frac{\pi h^2}{3}(3r - h)$$

where h is the linear displacement (mm) in the vertical (longitudinal) axis for the surface, r is the alumina ball radius (mm), which is assumed to be constant (6.35 mm) throughout the test, and V is the volumetric wear loss (mm^3). This theoretical calculation of V was verified by measurement of total volume loss (V_{tot}) by 3D profiling of the wear tracks. The theoretical and the 3D profiled wear volumes were found to be in good agreement with a maximum variation of 2%. The study reports the average coefficient of friction (COF) values, and the wear volume loss calculated using the 3D wear track profiles. The COF and wear volume are reported along with their maximum and minimum deviations calculated over three repetitions of the experiment.

6.1.4. Open circuit potential (OCP) measurements

The OCP measurements were carried out on untreated, and LSP processed AZ31B surfaces to understand and compare their open circuit kinetics in 3.5% NaCl. The OCP, also known as the corrosion potential is a mixed potential that depends on the rate of the anodic as well as the cathodic reactions. If the corrosion cell involves one dissolution reaction and one cathodic reaction, the corrosion potential will be between the reversible potentials of the two half-reactions. Understanding this evolution of OCP will provide an insight into the kinetics of corrosion without wear for untreated, and LSP processed AZ31B Mg surfaces. The experiments were conducted using 3-electrode configuration, which consisted of Mg surface as the working electrode, standard calomel electrode (SCE) as the reference electrode, and 99% pure graphite as the counter electrode. The OCP was measured using a Gamry reference 3000 potentiostat. All potential in the present study is reported with reference to SCE, which has a potential of 0.250 V vs. SHE (standard hydrogen electrode) at 25 °C. A working electrode area of 2.5 cm^2 was exposed to the electrolyte. Each test was carried out three times to ensure repeatability of results.

6.1.5. Tribocorrosion tests

The tribocorrosion tests were carried out based on the free potential method, also known as zero resistance ammeter (ZRA). The ZRA method has been used instead of the ASTM G119 mainly due to the susceptibility of AZ31B Mg alloys to hydrogen embrittlement under polarization conditions in corrosive environments [203, 204]. It has been shown that ASTM G119, which uses an external reference, such as wear at cathodic potential during the tribocorrosion testing, can induce the risk of hydrogen embrittlement [205]. This would lead to inaccurate estimations of tribocorrosion properties for the substrate surface. The ZRA method of tribocorrosion testing enables measurement of the galvanic current between the passive (cathode, unworn area) and the depassivated (anode, worn area) areas of the sample surface at OCP.

In the present study, 17×7 mm^2 surface area of AZ31B Mg alloy was in contact with the electrolyte throughout the tribocorrosion testing. Within this area of contact, the cyclic 10 mm reciprocating sliding of alumina ball on Mg surface was the depassivated area (anode), and the remaining unworn surface was the passive area (cathode), thus completing the galvanic couple. *Figure 6.2* schematically illustrates the tribocorrosion test setup used for the experiments. The setup shown is a combination of the standard reciprocating test on a tribometer and a 3-electrode electrochemical test configuration connected to the potentiostat. The reciprocating test consisted

of the alumina-Mg alloy tribo-pair, and the electrochemical test consisted of the sample surface as the working electrode, SCE as the reference, and graphite as the counter electrode that was connected to the potentiostat. *Figure 6.2* also shows the passive and depassivated regions of the Mg alloy surface during sliding. The tribocorrosion test was conducted for 4000 mm sliding distance at a speed of 1 mm/s and a normal load of 20N. The tests were conducted at laboratory conditions of 24 °C lab temperature and 15% relative humidity. During the reciprocating tests, potential and current values were recorded on the potentiostat while the wear and friction force were recorded on the tribometer, in-situ.
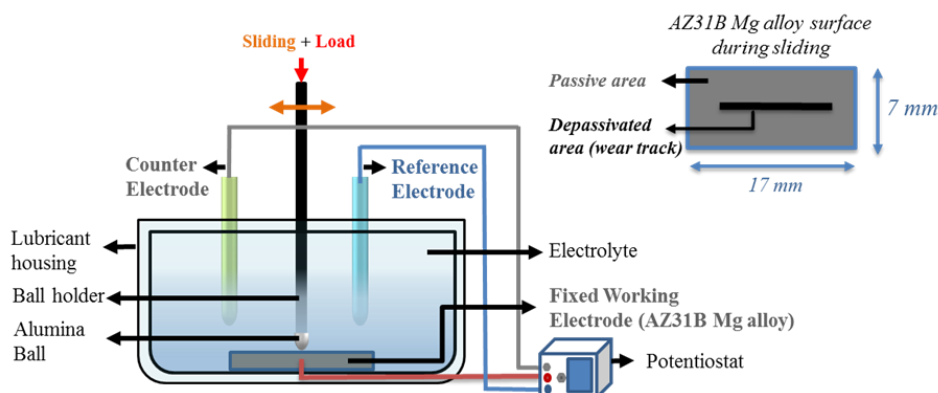
Figure 6.2: Schematic of tribocorrosion test setup and the galvanic couple of worn (depassivated) and unworn (passivated) area during sliding.

6.2. Results and discussion

6.2.1. Evolution of OCP during tribocorrosion

The evolution of OCP during tribocorrosion as a function of sliding distance is shown in *Figure 6.3*. The figure shows the OCP of various surfaces (untreated, and LSP-1 to 5) in 3.5% NaCl. The OCP is the corrosion potential (E_{OC}) defined by the rate of anodic, as well as cathodic reactions. E_{OC} reflects the dissolution reaction at the depassivated wear track and cathodic reaction on the passive unworn regions of the AZ31B surfaces. The OCP data was monitored and recorded before sliding, during sliding (4000 mm), and after sliding. In the tests, sliding was initiated only after ensuring a stable E_{OC} within the tribochemical system. It was observed that all LSP processed surfaces (LSP-1 to LSP-5) stabilized at a potential of -1.59 ± 0.008 V except for the untreated surface, which stabilized at a slightly higher potential of -1.538 ± 0.005 V. It can be observed in *Figure 6.3* that after the onset of sliding, the E_{OC} for untreated surface showed the highest

variations followed by the E_{OC} for LSP-5 and 4. The E_{OC} for LSP-1, 2, and 3 were found to be the most stable with the potential, almost consistent throughout the 4000 mm sliding distance. At the end of the sliding, the E_{OC} for the untreated surface stabilized at -1.37 ± 0.006 V, which is 12.26% more than the E_{OC} before sliding. The E_{OC} of LSP-5 and 4 stabilized at of -1.496 ± 0.005 V, and -1.575 ± 0.004 V, respectively. The E_{OC} before sliding and after sliding were almost the same for LSP-1, 2, and 3.
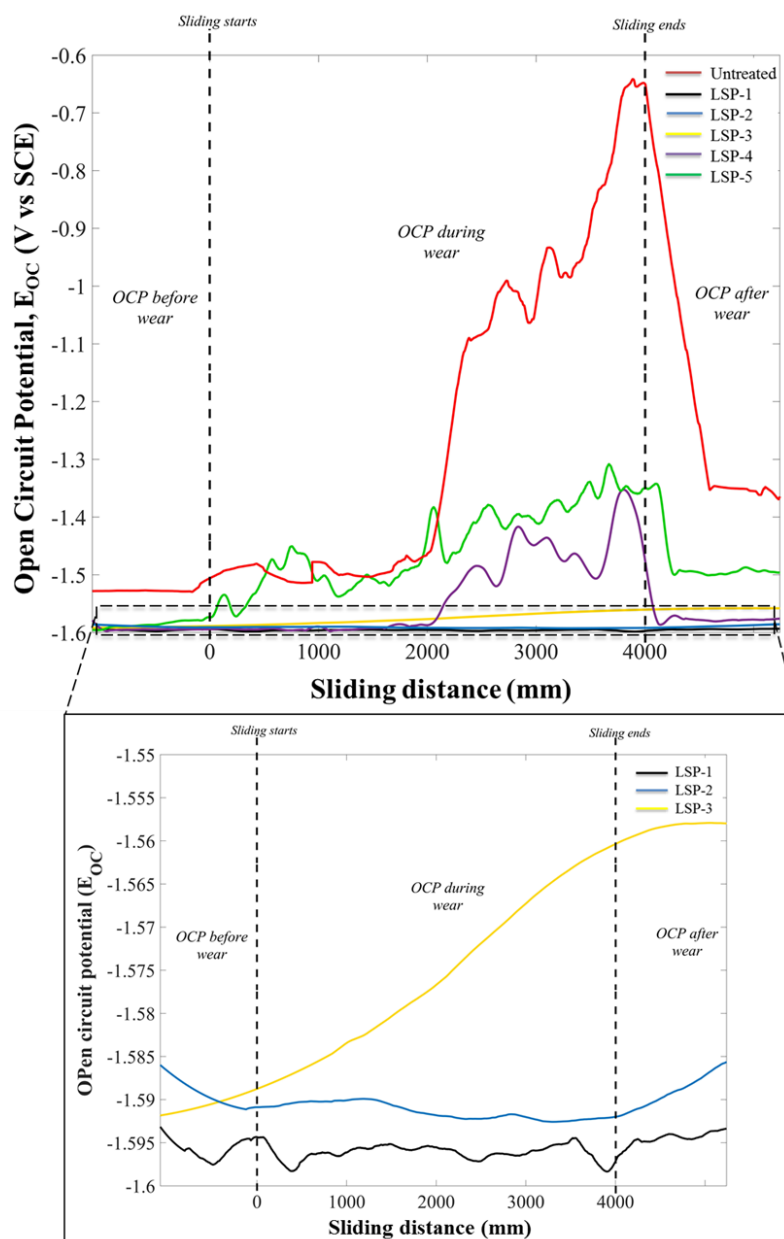
Figure 6.3: Evolution of OCP as a function of sliding distance during the tribocorrosion test.

6.2.2. *Friction behavior during tribocorrosion*

During tribocorrosion tests, the evolution of friction was also monitored to understand the effect of tribocorrosion on the COF. *Figure 6.4* reports the average COF during sliding for untreated and LSP processed surfaces under the action of tribocorrosion. The average COF for the untreated surface was found to be 0.14. It can be observed in *Figure 6.4* that all LSP treated surfaces show a lower COF than the untreated surface. When the surface was treated at LSP-1, the COF dropped by 43% as compared to the untreated surface, which was the lowest COF observed among all the surface conditions. The COF of LSP-2, 3, 4, and 5 were found to be 28%, 21%, 14.3%, and 7.14% less than the untreated surface, respectively. This trend in COF is consistent with the OCP behaviors of the surfaces, where the untreated surface had the highest COF, and LSP-1 had the lowest COF. An increase in COF is observed as the laser intensity increases from LSP-1 to LSP 5. This similarity in the trend for COF and OCP relative to the applied laser intensity indicates that surfaces exhibiting low COF can have a stable OCP and are least susceptible to tribocorrosion. Earlier studies concerning the effect of LSP on the friction behavior of surfaces have shown that at low laser intensities the surface strengthening effect defined the friction behavior. As the laser intensity increases the surface roughening effect of LSP plays a major role in defining the friction behavior [40]. At a low laser intensity of LSP-1, a considerably low COF is observed due to the increase in surface hardness after LSP. But, as the laser intensity increases to LSP-5 the surface roughening effect is dominant which causes an increase in COF during sliding. Further, the surface roughening effect at relatively high laser intensity treatment causes larger fluctuations in OCP during sliding (*Figure 6.3*).
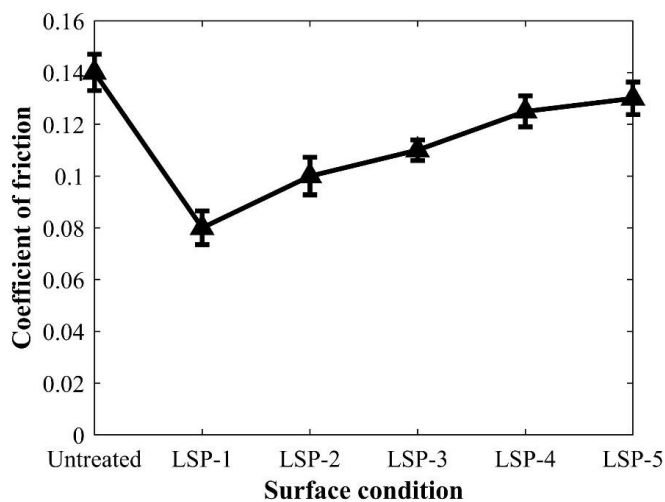
Figure 6.4: Coefficient of friction during tribocorrosion tests.

6.2.3. *Wear behavior during tribocorrosion*

It is necessary to investigate the changes in the surface morphology of the galvanic couple to understand the mechanism of OCP evolution observed during sliding (*Figure 6.3*). The surface morphology of the galvanic couple includes the worn and unworn area of the AZ31B surface exposed to the electrolyte. *Figure 6.5* shows the 3D profiles of the worn and unworn areas after tribocorrosion testing of untreated and LSP processed AZ31B surfaces. The changes in surface morphology of unworn areas after tribocorrosion observed in *Figure 6.5* depicts the effect of galvanic corrosion accelerated by wear. It can be observed that the initiation of localized corrosion on the unworn areas caused serrated filament-shaped pits, giving rise to more localized corrosion sites. These pits may be a resultant of the oxide film breakdown during LSP as a function of the applied laser intensity, which can lead to varying degrees of pitting corrosion when exposed to aqueous NaCl environments [120].
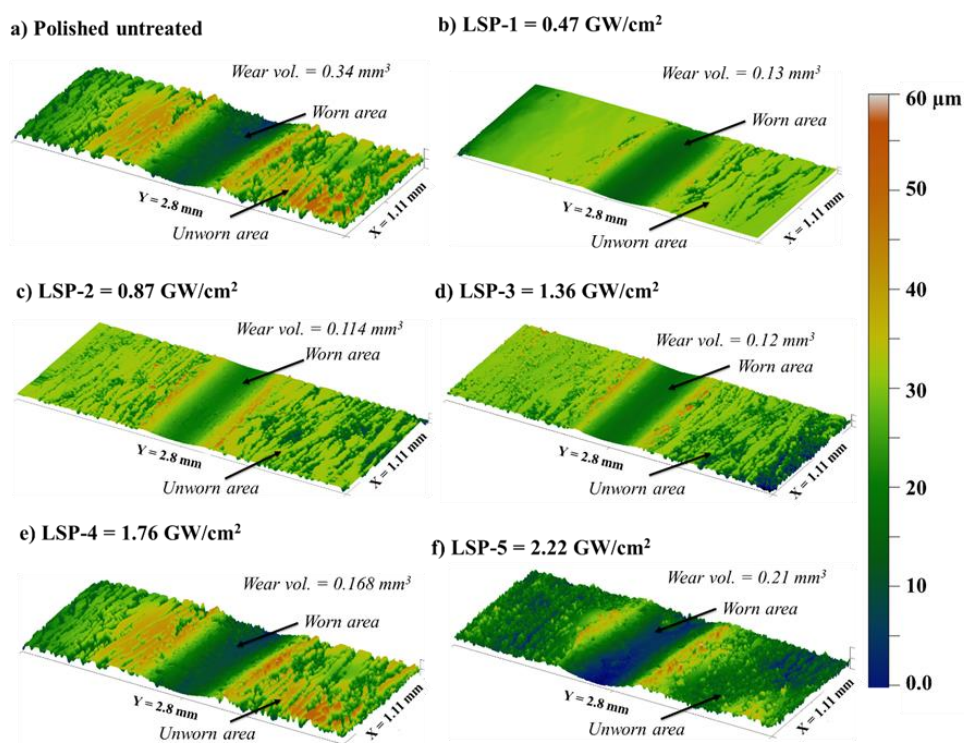
Figure 6.5: Wear track and unworn area after tribocorrosion testing of AZ31B surfaces conditions at (a) untreated surface (b) LSP-1 (c) LSP-2 (d) LSP-3 (e) LSP-4 (f) LSP-5.

The initiation of galvanic corrosion for AZ31B occurs due to the differential electrocatalytic mechanism, where the areas consumed by the corrosion products catalyze hydrogen evolution (HE) reaction [206, 207]. These HE reactions dissolve the Mg and any oxide layers (porous films

[120]) around the corrosion-initiated regions, and the laterally spreading corrosion sites lead to the formation of serrated filament shaped pits leaving behind significantly roughened regions on the surface [208-212]. It is these serrated filament shaped pits that lead to an increase in the average roughness, S_a, which is discussed in the following section. The initiation and propagation of these corrosion sites are further accelerated by the wear debris generated during sliding, which is the effect of wear-corrosion synergism and is observed as an increase in the OCP (*Figure 6.3*) during sliding. During the action of wear-corrosion synergism the metal in the wear track and the metallic wear debris in the electrolyte undergo oxidation reactions forming soluble ions and/or solid products as per the following reactions [213]:

$$M \rightarrow M^{n+} + ne^-$$

$$M + \frac{n}{2}H_2O \rightarrow MO_{n/2} + nH^+ + ne^-$$
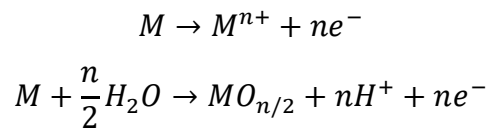
where *M* designates the metallic materials. The generated electrons are consumed by the cathodic reactions (unworn area) in order for the oxidation reactions to proceed. The cathodic reaction in the aqueous solution that leads to the HE and formation of any hydroxides are [213]:

$$2H^+ + 2e^- \rightarrow H_2$$

$$O_2 + 2H_2O + 4e^- \rightarrow 4OH^-$$
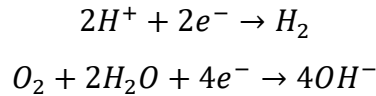
It can be observed in *Figure 6.5* that the formation of serrated filament-shaped pits (hereafter referred to as '*pits*') are prominent on both the worn and the unworn area of the untreated AZ31B surface while for the LSP processed surfaces the pits are predominant on the unworn regions. This indicates that the difference in the corrosion potential of the worn and unworn regions for the untreated surface is higher than for the LSP processed surfaces. Since the ratio of the worn (anodic) to the unworn area (cathodic) exposed to the electrolyte is the same for the untreated and all the LSP treated surfaces, the wear-corrosion synergistic effect is defined by the corrosion potentials and kinetics of the reactions on the worn and unworn areas. It has been shown that exposure of AZ31B Mg alloy to aqueous NaCl solutions results in extensive, nanoporous $Mg(OH)_2$ formation with very high surface areas that range from 4 to 40 m^2/g [120]. In the present study, the break down of this $Mg(OH)_2$ film during sliding leads to the difference in corrosion potential on the worn and unworn areas leading to tribocorrosion. Additionally, due to the porous nature of the $Mg(OH)_2$ film rapid, non-protective corrosion can be observed on the unworn area of AZ31B surface [120]. The increase in surface area of the oxide layer formation is also expected to affect the corrosion behavior of the surface.

The wear volumes indicated in *Figure 6.5* reflects the involvement of wear in accelerating the corrosion. As the highest wear was observed for the untreated surface (0.34 mm^3), it can be seen in *Figure 6.3* that after the onset of sliding the E_{OC} of untreated surface fluctuates by $\pm$ 0.05 V until a sliding distance 2000 mm after which the E_{OC} fluctuates and increase drastically until the end of sliding. This is due to the increase in the generation of wear debris, which accelerates the rate of anodic and cathodic reactions. During the sliding, the E_{OC} for the untreated surface had changed by nearly 57.5%. In the case of LSP-5, a wear volume of 0.21 mm^3 was observed with an increase in E_{OC} after the initiation of sliding. This increase in E_{OC} for LSP-5 was not as drastic as for the untreated surface since the E_{OC} had changed by only 17.5% during sliding. The early onset of fluctuations in OCP observed for the LSP-5 surface may be due to the roughening effect of high laser intensity during LSP that can increase the wear during sliding. Similarly, an increase in E_{OC} for LSP-4 surface was observed after 2000 mm of sliding with a 14.6% change in E_{OC} during sliding. The surface processed at LSP-3 had a 2.4% increase in E_{OC} during sliding while there was <1% change in E_{OC} for LSP-2 and LSP-1. These observations reinforce the earlier indications that LSP of a surface with good surface characteristics (surface roughening and strengthening effects) can yield a consistent tribological and tribocorrosion performance.

6.2.4. *Effect of LSP and tribocorrosion on surface roughness*

The surface morphology of AZ31B Mg alloy samples was investigated before and after LSP processing, and tribocorrosion testing. For instance, *Figure 6.6* shows the surface profile and roughness of a sample after polishing, LSP processing at 0.47 GW/cm^2, and after tribocorrosion testing. Similarly, surface profiles were recorded for other LSP processed samples, as shown in *Table 6.2*. The authors in their earlier tribological study of LSP processed surfaces investigated the effect of average surface roughness (S_a), skewness (S_{sk}), and kurtosis (S_{ku}) parameters as they were found to affect friction and transfer layer formation [40]. Hence, the current investigation of surface roughness parameters was limited to these three parameters with a focus on understanding the effect of tribocorrosion on LSP processed surfaces. Surface roughness is especially important in understanding the influence of wear-corrosion synergism since the AZ31B unworn area (area outside the wear track) is part of the galvanic couple with the worn area (area of wear track) of AZ31B surface. The changes in surface roughness of the unworn area influence the rate of corrosion initiation sites that initiate and impel the tribocorrosion process. [126, 214].

Table 6.2: Surface roughness parameters of AZ31B Mg surfaces after LSP processing at various laser intensities and tribocorrosion testing.

Surface processing	Surface condition of AZ31B Mg alloy	Surface roughness (µm)			Change in value after tribocorrosion[*]		
		S_a	S_{sk}	S_{ku}	ΔS_a	ΔS_{sk}	ΔS_{ku}
Polished untreated	Before testing	0.1 ± 0.02	1.23	2.32	7.24	(-)1.17	(-)2.99
	After polarization test (corrosion without wear)	2.9 ± 0.1	-0.74	-0.24			
	After tribocorrosion test	7.34 ± 0.15	0.06	-0.67			
LSP-1 0.47 GW/cm^2	Before testing	0.16 ± 0.05	0.36	0.51	1.34	(-)0.67	(-)0.43
	After tribocorrosion test	1.5 ± 0.07	-0.31	0.08			
LSP-2 0.87 GW/cm^2	Before testing	0.17 ± 0.03	-0.05	-0.31	2.06	(-)0.17	(-)0.23
	After tribocorrosion test	2.23 ± 0.1	-0.22	-0.54			
LSP-3 1.36 GW/cm^2	Before testing	1.2 ± 0.02	-0.67	-0.58	2.51	0.3	0.38
	After tribocorrosion test	3.71 ± 0.1	-0.37	-0.20			
LSP-4 1.76 GW/cm^2	Before testing	1.5 ± 0.08	-0.05	-0.74	3	0.28	0.16
	After tribocorrosion test	4.5 ± 0.11	0.23	-0.58			
LSP-5 2.22 GW/cm^2	Before testing	1.5 ± 0.06	-0.52	0.85	3.2	1.29	(-)1.09
	After tribocorrosion test	4.7 ± 0.12	-0.77	-0.24			
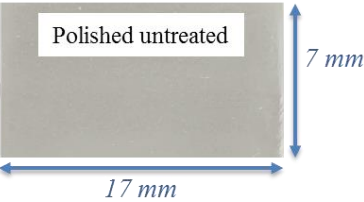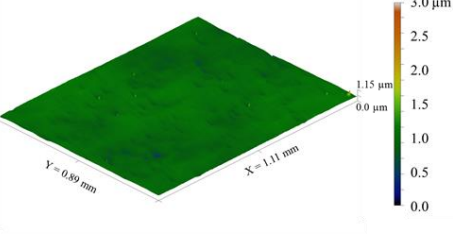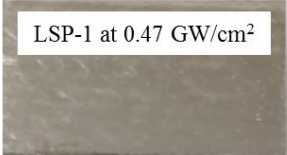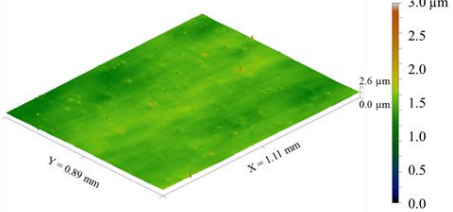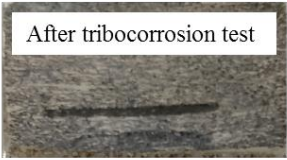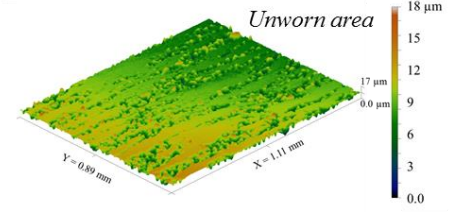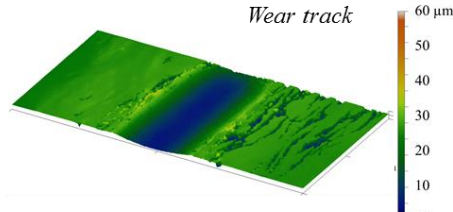
Surface condition of AZ31B Mg alloy	3D surface profile	Surface roughness
Polished untreated 7 mm 17 mm		$S_a = 0.1 \pm 0.02$ μm $S_{sk} = 1.23$ $S_{ku} = 2.32$
LSP-1 at 0.47 GW/cm^2		$S_a = 0.16 \pm 0.05$ μm $S_{sk} = 0.36$ $S_{ku} = 0.51$
After tribocorrosion test	*Unworn area* *Wear track* 	$S_a = 1.5 \pm 0.03$ μm * $S_{sk} = -0.31$ $S_{ku} = 0.084$ * Roughness parameters for unworn area

Figure 6.6: Surface profiles and roughness parameters of AZ31B Mg surface after polishing, LSP processing at 0.47 GW/cm^2, and after its tribocorrosion testing.

Table 6.2 details the three roughness parameters S_a, S_{sk}, and S_{ku} measured for untreated, LSP processed, and tribocorrosion tested surface conditions of the samples. It can be observed that even though the LSP processing has a similar effect on all the three surface roughness parameters as discussed in the authors' previous study [40], the effect of tribocorrosion is evident only in S_a. When the AZ31B Mg surfaces are LSP processed and tribocorrosion tested, the change in S_{sk} ($\varDelta S_{sk}$) and the change in S_{ku} ($\varDelta S_{ku}$) values are found to be small and inconsistent while the change in S_a ($\varDelta S_a$) value is found to increase relative to the applied laser intensity. The $\varDelta S_a$ observed in *Table 6.2* is highest for the untreated surface and increases as the applied laser intensity is increased from LSP-1 to LSP-5. It is well known that the LSP generates indents (dimples) on the surface, and it

is these indents that affect the surface morphology of the processed area [48]. *Figure 6.7* shows the change in surface morphology of AZ31B, before and after LSP. The figure shows that a low laser intensity treatment of AZ31B Mg alloy surface produces smaller dimple effects as compared to the dimple effects observed at high laser intensities [40, 48]. The applied laser intensity defines the change in surface roughness and extent of asperity deformation on the surface. These dimples play an important role in defining the surface area that is exposed to the electrolyte during tribo-contact. In the case of AZ31B Mg surfaces, it has been shown that the dimple effect can exceed a depth of 0.8 mm from the surface depending on the applied laser intensity [215]. Hence, the LSP processing of AZ31B Mg surfaces may cause a high degree of local plastic deformation that affects the average surface roughness S_a more drastically than S_{sk} or S_{ku}. Further, the change in surface area due to LSP is expected to affect the tribocorrosion behavior of the processed surfaces.
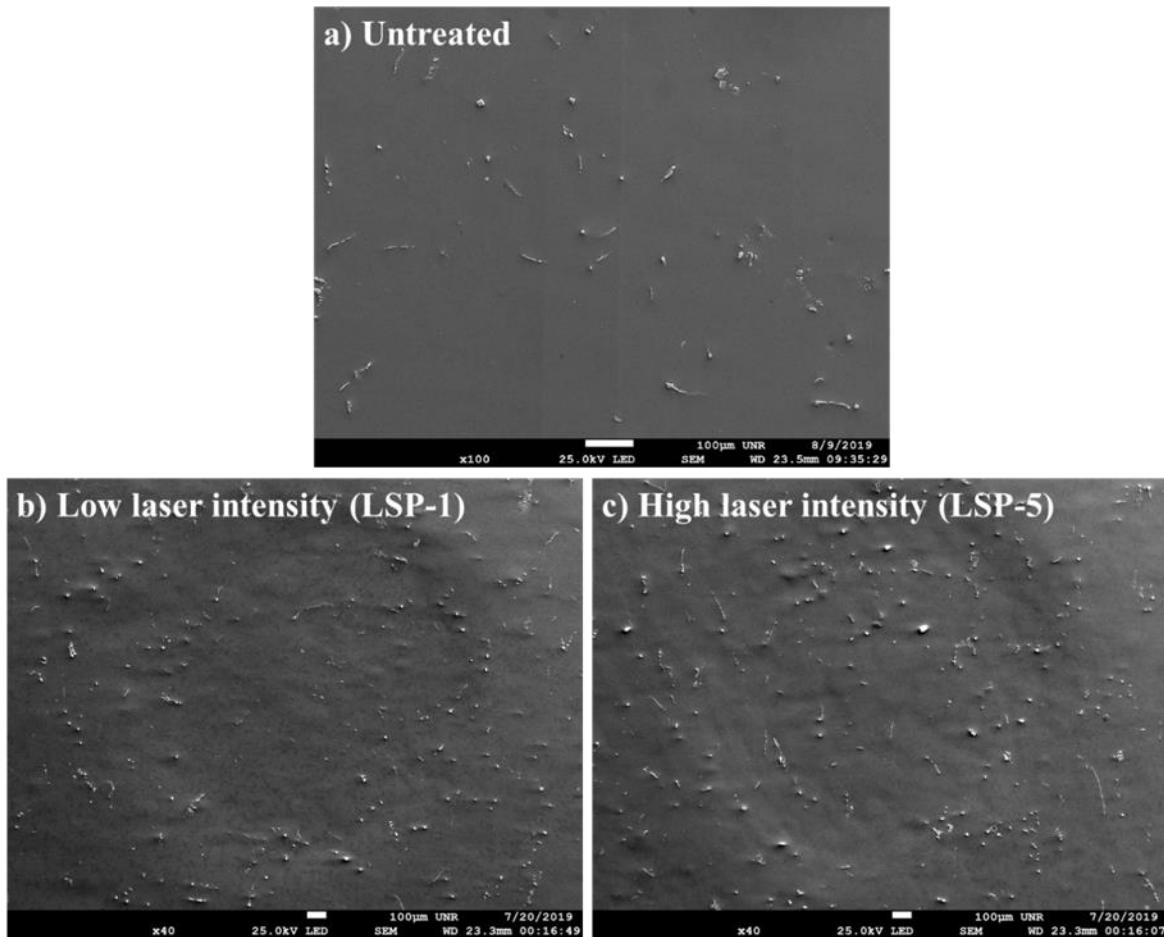
Figure 6.7: SEM images of AZ31B Mg alloy surface (a) untreated (b) low laser intensity LSP-1 (c) high laser intensity LSP-5.

In order to clearly distinguish the effect of tribocorrosion on the S_a for LSP processed surfaces, the S_a before and after tribocorrosion is shown in *Figure 6.8*. It can be observed that the untreated surface experiences the maximum increase in S_a after tribocorrosion as compared to the LSP processed surfaces. It can be expected that the surface strengthening effect of LSP processing aided in reducing the variations in surface roughness due to tribocorrosion at low laser intensities. As the laser intensity increases the surface roughening effect of LSP increases and a larger variation in surface roughness can be observed after tribocorrosion. This behavior indicates that the surface strengthening and roughening effect of laser processing can aid in modifying the surface characteristics and hence the tribocorrosion resistance of the surface.
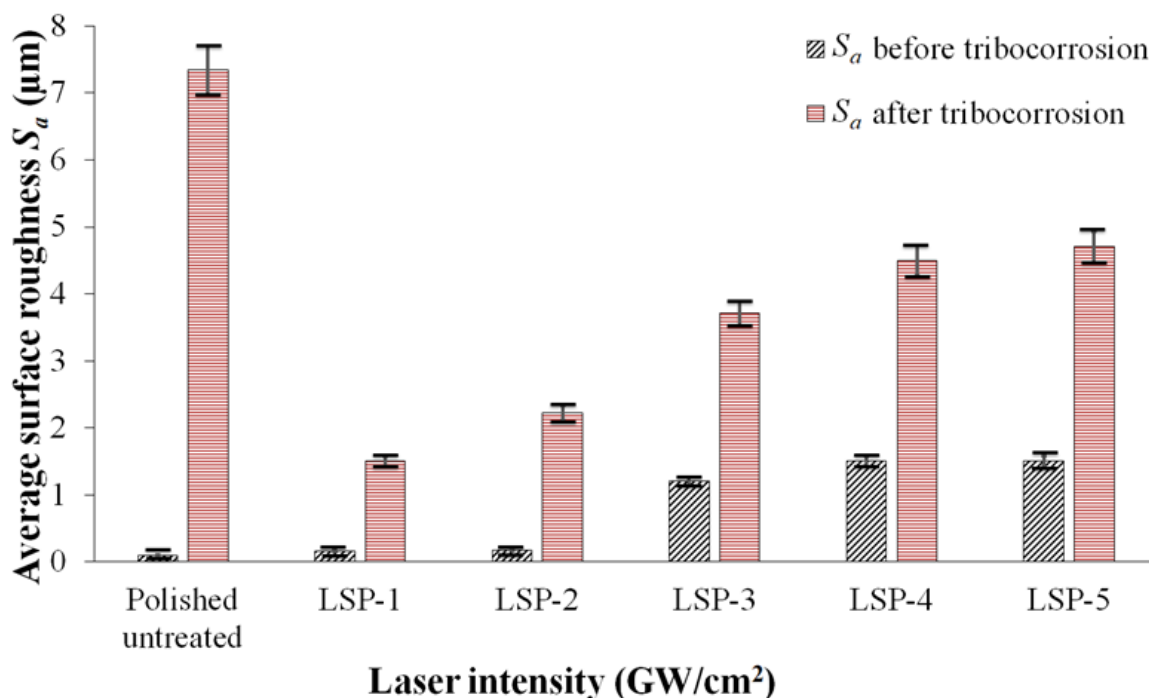
Figure 6.8: SEM images of AZ31B Mg alloy surface (a) untreated (b) low laser intensity LSP-1 (c) high laser intensity LSP-5.

The LSP process inherently also breaks down oxide films at specific points depending on the applied laser intensity [131]. The same can be observed to affect the surface roughness after LSP of the AZ31B surface. The beak down of oxide films in this manner initiates pitting corrosion and affect the tribocorrosion behavior of the surface. The change in S_a shown in *Figure 6.8*, indicates the breakdown of oxide film should be negligible at laser intensity, LSP-1, as compared to the untreated and other LSP surfaces. With regards to Mg alloy, the structural mismatch between the hexagonal Mg lattice and the crystalline structure of the passive oxide layer will weaken the

adherent ability of the oxide layer [118, 128]. It is expected that LSP can be an effective method to mitigate the weak adhesion of oxide layers.

6.2.5. Microhardness

The correlation between the hardness of LSP processed surfaces and its wear behavior has been well reported in previous studies [38, 48, 53, 216]. These studies indicate that the wear resistance increases with an increase in hardness due to the surface strengthening effect of LSP processing. *Figure 6.9* shows the change in microhardness observed due to LSP of AZ31B Mg surfaces at various laser intensities. The figure also shows the variation in wear volumes after tribocorrosion testing (4000 mm sliding distance) for these LSP processed surfaces.
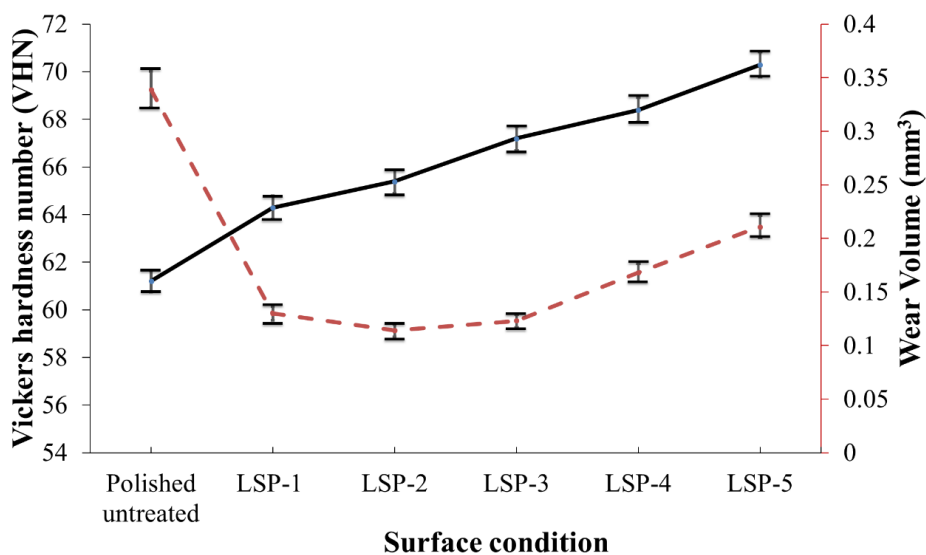
Figure 6.9: SEM images of AZ31B Mg alloy surface (a) untreated (b) low laser intensity LSP-1 (c) high laser intensity LSP-5.

It can be observed in *Figure 6.9* that as the laser intensity increases, the microhardness of the surface increases. However, the corresponding wear volumes do not decrease as expected with an increase in hardness. It was found that the untreated AZ31B Mg surface had a hardness of 61.2 VHN and experienced a wear volume of 0.34 mm^3. When the surface was LSP processed at LSP-1 (0.47 GW/cm^2) the microhardness increased by 5.1% while the wear volume decreased by 61.7%. When the laser intensity was increased to LSP-2 (0.87 GW/cm^2) the microhardness increased by 7% and the wear volume decreased by 66.4% as compared to the untreated surface. Theoretically, as the laser intensity is further increased it is expected that the microhardness would increase and the corresponding wear volume would decrease [45, 48]. However, when the laser

intensity was increased to LSP-3 (1.36 GW/cm^2) the microhardness increased by 10% and its corresponding wear volume decreased only by 64%, which is less than the 66.4% observed for LSP-2. This indicates a negligible surface strengthening effect of LSP on the wear resistance when the laser intensity was increased from LSP-2 to LSP-3. Further, as the laser intensity was increased to LSP-4 and LSP-5 the microhardness increased by 11.8% and 15%, respectively with the corresponding wear volumes decreasing by 50.4% and 37.8%, respectively as compared to the untreated surface. These observations indicate that at low laser intensity LSP the surface strengthening effect had a dominating influence on wear during tribocorrosion and as the laser intensity increased the surface roughening effect of LSP had a dominating influence on wear.

6.2.6. Surface behavior model

The observed effects of tribocorrosion on the surface characteristics of untreated and laser processed surfaces indicate that the tribocorrosion behavior varies with laser intensity. Based on the observed evolution of OCP, surface roughness, COF, and wear during tribocorrosion, a surface behavior model for the laser processed surfaces in a tribocorrosion system has been presented in *Figure 6.10*. The model represents a direct proportionality between the laser intensity and the tribocorrosion behavior of the surface. The untreated surface was found to be highly susceptible to corrosion initiation and had high friction and wear characteristics with drastic changes in OCP during tribocorrosion. Additionally, there was a drastic change in surface roughness of the untreated surface after tribocorrosion. At low laser intensity LSP, the surface exhibits a low COF and low wear along with a stable OCP during tribocorrosion. This was due to the increased surface strength with minimal change in surface roughness at low laser intensity LSP. After tribocorrosion, these surfaces had minimal change in surface roughness. As the laser intensity of LSP is increased, the surface exhibits a high COF and wear, and moderate changes in OCP during tribocorrosion. The high COF and wear during tribocorrosion are due to the increased surface roughening effects at high laser intensity LSP (*Figure 6.8*). This surface roughening increases the surface area and provides an increased number of corrosion initiation sites, leaving higher surface rougher after tribocorrosion.

Similar tribological effects of LSP processed surface were observed in the author's previous study [40]. These studies indicate that LSP processing is an effective method of moderating and mitigating tribocorrosion by inducing appropriate surface strengthening and roughening effects. The study shows that by understanding the initial surface morphology and correlating the effect of

LSP on the tribological behavior of the surface, it is possible to tailor the tribocorrosion behavior of the surface. For AZ31B Mg alloy, it was observed that the surfaces processed at low laser intensities (LSP-1 and LSP-2) had a good balance of the surface roughening and strengthening effects that resulted in minimization of wear-accelerated corrosion. It is speculated that the stable OCP observed for surfaces treated at low laser intensities indicates low corrosion potential difference between the worn and unworn regions of the surface. This is believed to directly correlate to the reduction in corrosion initiation sites on the unworn areas and minimize the galvanic corrosion. Additionally, the inherent high wear resistance of LSP processed surfaces aids in decreasing the rate of wear-accelerated corrosion and thus decreasing the effect of tribocorrosion.
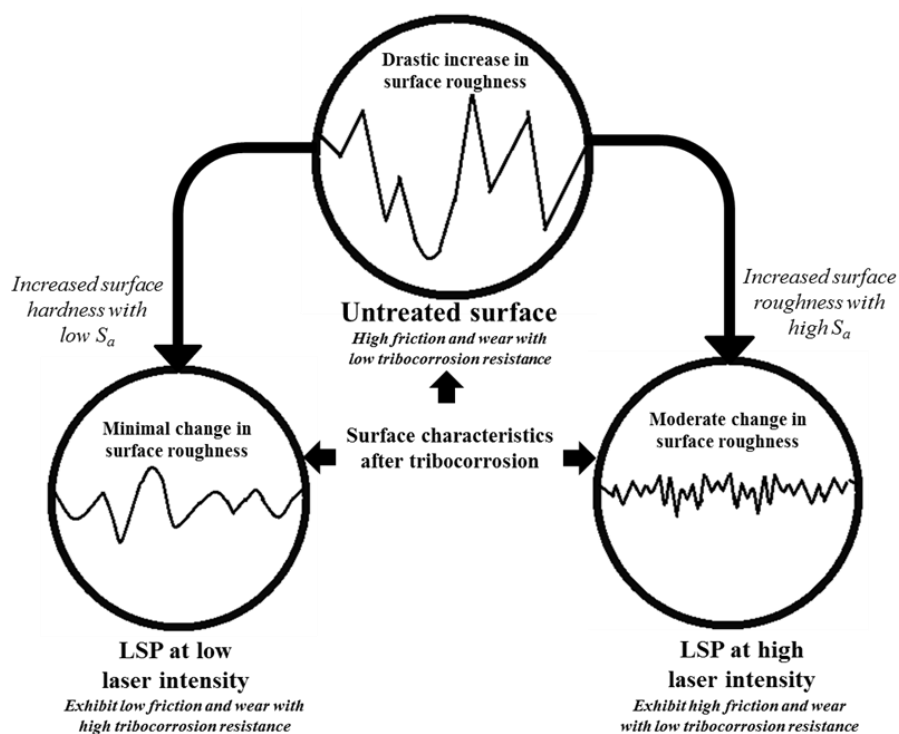
Figure 6.10: SEM images of AZ31B Mg alloy surface (a) untreated (b) low laser intensity LSP-1 (c) high laser intensity LSP-5.

6.3. Conclusions

The present study investigated the effect of LSP on the tribocorrosion behavior of AZ31B Mg surfaces. More specifically, the influence of surface roughening and strengthening due to LSP on the evolution of friction, wear, and tribocorrosion (wear-accelerated corrosion) properties were

studied. The ZRA method was used to investigate the tribocorrosion behavior of AZ31B surfaces. Additionally, the study validates the hypothesis that the tribological properties such as wear and friction during the action of tribocorrosion on LSP processed surfaces are influenced by both the surface strengthening and roughening effects of the applied laser intensity. Following conclusions can be drawn from this investigation:

- Understanding the change in surface roughness parameters due to tribocorrosion is necessary to investigate the onset and propagation of galvanic corrosion and its synergism with wear.

- S_a is found to reflect best the surface roughening effects resulting from the tribocorrosion of LSP processed surfaces.

- The increase in the slope of measured OCP during sliding is found to increase the wear-corrosion synergistic effect.

- The initiation and propagation of corrosion sites are influenced by the wear debris, which indicates a dominant wear-accelerated corrosion behavior for AZ31B Mg alloy.

- The initiation of localized corrosion on the unworn areas caused serrated filament-shaped pits, giving rise to more localized corrosion sites, which drastically increased the S_a during tribocorrosion.

- The initiation and propagation of corrosion sites are accelerated by the wear debris generated during sliding, which results in wear-accelerated corrosion.

- Surfaces treated at low laser intensities (LSP-1, 2, and LSP-3) have the least increase in E_{OC}, and lowest wear volume and friction during sliding.

- During tribocorrosion, the surface strengthening effect of LSP had a dominating influence on wear at low laser intensities (LSP-1, 2 and 3), whereas the surface roughening effect of LSP had a dominating influence on wear at higher laser intensities (LSP-4 and LSP-5).

- The change in surface roughness due to LSP affects the tribocorrosion behavior of the processed surface.

The insight into the tribological and tribocorrosive behaviors of LSP surfaces with reference to their surface roughness motivates the next chapter that presents study concerning the surface energy of LSP surfaces. Surface roughness which modifies the surface energy of the engineered surfaces is an important factor in defining the corrosion and tribocorrosion behavior in addition to lubricating properties.

Chapter 7: Effect of surface energy of engineered surfaces on tribocorrosion

The present study investigates the influence of laser shock peening (LSP) on surface energy (S_E) of AZ31B Magnesium alloy and its resilience to corrosion and tribocorrosion. AZ31B alloy was treated at different laser intensities. The surface energy and its interfacial components of treated surfaces were analyzed. The surface energy was found to be least at low laser intensity LSP. Lower interfacial surface energy showed decreased wettability, providing enhanced tribocorrosion resistance with respect to untreated surface. However, higher laser intensities increased the surface roughening effect, causing an increase in the interfacial surface energy and wettability of the surfaces, decreasing the tribocorrosion resistance. The study furthers the understanding of surface functionalization using LSP by providing insight into the influence of surface energy on corrosion and tribocorrosion properties. The knowledge of surface energy changes due to LSP will allow better design AZ31B surface properties for sustainable and diverse applications, including applications in aqueous environments.

7.1. Materials and methods

An experimental procedure was developed to study the surface energy changes due to tribocorrosion on LSP processed AZ31B. The AZ31B block (Al - 3.0 wt.%, Zn - 1.0 wt.%, and 96 wt.% Mg) were cut into six $25 \times 25 \times 12.5$ mm^3 samples for the study. A mean surface roughness value (S_a) of 0.3 ± 0.08 μm was achieved by polishing the samples. The polishing involved grinding the surfaces using sandpapers ranging from 320 to 1200 grit size. Further, a diamond suspension (3 μm) was used to polish the samples to achieve the desired roughness. Among the six polished samples, five surfaces underwent LSP at varying laser intensities and one surface was untreated. The surface roughness, hardness, and contact angle measurements were made on each sample, followed by tribocorrosion testing. The experimental methodology is detailed below.

7.1.1. LSP of AZ31B surfaces

The laser processing of the AZ31B surfaces was carried out with a Q-switched Nd-YAG laser (λ = 1064 nm, pulse = 7 ns, beam size = 2.5 x 10^{-3} m). The confinement layer was a BK7 glass which was layered with a black tape ablative coating of thickness of 130 μm [40]. The laser intensity used to process a surface area of 17×7 mm^2 is detailed in *Table 6.1* (Chapter 6), along with the respective nomenclature. The AZ31B surfaces were LSP processed, as illustrated in the

Figure 6.1 (Chapter 6). The figure shows a 17 x 7 mm² surface area that was processed on each sample. The influence of LSP on the surface energy and tribocorrosion performance were analyzed by exposing the laser treated area.

7.1.2. SR and hardness

A Wilson Hardness tester was used to assess the change in hardness due to LSP processing. A load of 500 g was applied with dwell time of 10 s. The variation in SR due to LSP and tribocorrosion on AZ31B surface was analyzed by a 3D optical profilometer. Each surface roughness parameter and hardness measurement were repeated three times. The average of the parameter values is reported with error bars. The error bars for the reported roughness parameter and hardness values were obtained from the standard deviation considering a 90% confidence interval.

7.1.3. Contact angle and surface energy measurements

The total surface energy and the solid-liquid interfacial surface energy between the LSP processed AZ31B surface and three probe liquids were evaluated using rame-hart contact angle goniometer. *Table 7.1* details the probe liquids used in the study in addition to their total surface tension and surface tension components. A sessile drop method was used to measure the contact angle according to ASTM D7334 - 08(2013) standards for each LSP processed surface. The study uses a 3-component approach based on Lewis acid-base surface interaction components. The probe liquids, specifically water and 0.6 M NaCl, simulate some of the atmospheric conditions that lead to corrosion on the real surface area exposed to the environment. Sessile drop technique was performed at 24 °C and 20% RH. The probe liquids were collected in a 2 ml syringe to dispense droplet diameters of 2.5-3 mm (6 µl) on the sample surfaces. The contact angle of the droplet for each surface are reported by averaging the observed values over ten trials. The difference in the left and right contact angle of each droplet was less than or equal to 2°. These steps ensured the repeatability and reliability of the contact angle measurements. The interfacial surface energy with each probe liquid is determined using the Van Oss [129, 130] and Young's equation [217].

Table 7.1: Surface tension and its components.

Probe liquid	Total surface tension, γ_l	Dispersive and Lifshitz der Waals component, γ_l^{LW}	Positive polar acid-base component, γ_l^{AB+}	Negative polar acid-base component, γ_l^{AB-}
Water (W)	72.8	21.8	25.5	25.5
Glycerol (G)	64	34	57.4	3.92
0.6 M NaCl (N)	73.8	22.2	22	29.6

7.1.4. *Tribocorrosion tests*

The tribocorrosion test set-up involved a combination of reciprocating wear testing and a three-electrode electrochemical test configuration as shown in *Figure 6.2* (Chapter 6) [127]. The cell is made up of AZ31B surface - working electrode and a graphite electrode was used as a counter electrode. Whereas, a standard calomel electrode (SCE) was employed as the reference electrode. The equilibrium potential of the open circuit (OCP) was measured for each sample in 3.5% NaCl solution under static conditions. The SCE used in the study has a potential of 0.241 V vs. SHE (standard hydrogen electrode). The reciprocating test on the AZ31B surface was conducted at a speed of 1 mm/s for a total distance of 4000 mm and vertical load of 20 N. The counter material for the reciprocating test was alumina ball of 6.35 mm diameter.

The tribocorrosion test procedure consisted of two stages. The first set of experiments was performed to determine the wear without corrosion by applying cathodic polarization to the AZ31B surface at 1 V below the observed OCP and sliding in 0.6 M (3.5% NaCl solution). The second set of experimentation involved monitoring the OCP of the samples under dynamic conditions to determine the wear-corrosion synergistic effect by sliding with corrosion in 3.5% NaCl solution. Cumulatively, the tribocorrosion test procedure provided the wear-corrosion synergistic effect on wear.

The present study uses the corrosive conditions described in ASTM B895-99, where 0.6 M NaCl is used as the electrolyte. The temperature and humidity conditions during the test were 24 °C and 20% RH, respectively. The test involved in-situ measurement of wear, friction, surface potential, and current variation in the cell. The wear and friction data were collected through reciprocating test while the electrochemical cell was monitored using a potentiostat. Each test was repeated three times for the reproducibility of results. The reported wear behavior in the present study involves understanding the wear-corrosion effects on LSP processed AZ31B surface. The AZ31B surfaces (HV 62 to 72) are relatively soft as compared to the chemically inert alumina, a ceramic counter body (HV 1400 to1500). Moreover, due to the LSP on AZ31B, it is expected that subsurface material structural evolution may occur during tribocorrosion and corrosion testing causing a change in hardness. Hence to accurately interpret the wear loss due to tribocorrosion the wear tracks for with and without corrosion conditions on AZ31B surfaces were profiled using a 3D optical profilometer. The profiles yielded an accurate estimate of the wear volume for each trail, the average value of wear volume is plotted with standard deviation.

The expected worn and unworn regions on the working electrode (sample surface) during sliding is shown in *Figure 6.2* (Chapter 6). Following the tribocorrosion tests, the roughness of the exposed surface area was measured [127]. In addition to the surface roughness, the wear track profiles due to sliding in tribocorrosive conditions were also recorded using the profilometer to calculate the wear.

7.2. Results and discussion

7.2.1. *Influence of LSP on surface roughness*

The variation in surface roughness due to LSP on AZ31B surface was analyzed using a 3D optical profilometer. The surface roughness of AZ31B was recorded after polishing the samples to the same mean roughness (S_a) of 0.3 ± 0.08 μm and after LSP at five laser intensities (Table-1). All measurements were compared against the untreated surface condition of AZ31B (LSP-0, Untreated). The observed values of surface roughness parameters - mean roughness (S_a), maximum peak height (S_p), maximum valley depth (S_v), maximum height (S_z), and change in surface area after LSP are reported in *Table 7.2*.

Table 7.2: Surface roughness measurements of LSP processed AZ31B surface.

Laser intensity GW/cm^2	Surface roughness (μm)				Change in surface area
	S_a	S_p	S_v	S_z	
0	0.3 ± 0.08	0.32 ± 0.06	0.18 ± 0.04	0.74 ± 0.01	0%
0.47	0.35 ± 0.02	0.3 ± 0.03	0.19 ± 0.04	0.92 ± 0.1	1.9%
0.87	0.45 ± 0.02	0.33 ± 0.16	0.2 ± 0.02	1.2 ± 0.2	2.34%
1.36	0.5 ± 0.05	0.65 ± 0.2	0.41 ± 0.06	1.5 ± 0.4	3.1%
1.76	0.6 ± 0.05	0.8 ± 0.1	0.4 ± 0.1	2.2 ± 0.08	6.8%
2.22	0.9 ± 0.06	0.8 ± 0.07	0.9 ± 0.12	2.8 ± 0.05	10.1%

The plot comparing the change in surface roughness parameters and surface area of LSP processed AZ31B surfaces is shown in *Figure 7.1*. The laser intensities used for LSP were found to have a linear effect on the surface roughness parameters where the surface roughness is increases with laser intensity. This is due to the dimple effect (indents) generated by LSP on the surface, which modifies the surface morphology of the processed area [48]. During LSP, laser shock waves

are generated, which induce residual stresses, increase the surface hardness, and generate a variation in the asperity peak heights and valley depths relative to the applied laser intensity. The increased variation in the asperity with laser intensity causes an increase the real surface area that may lead to increased susceptibility of the surface to corrosion. But, it has been shown that the
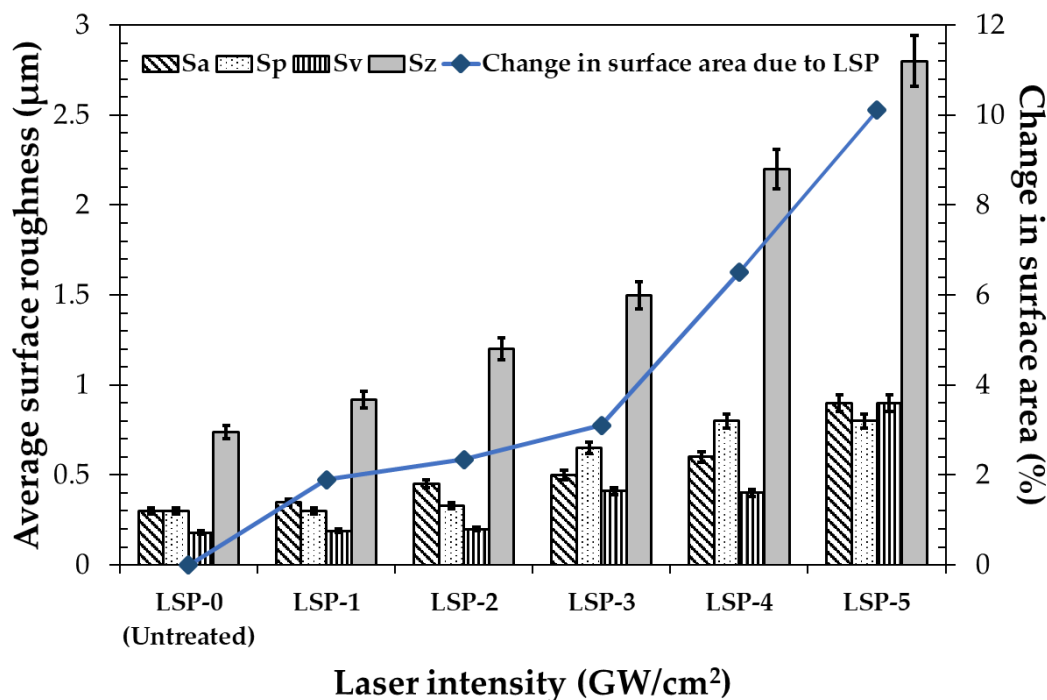
Figure 7.1: Surface roughness and area of LSP processed AZ31B alloy.

observed change in surface area occurs after LSP is a combination of surface roughening and hardening effects [40, 102], which can vary the corrosion inhibition properties of the surface [127, 198].

Further, the results show that the change in surface roughness after LSP can be best perceived using S_a, S_p , S_v, and S_z roughness parameters. The LSP is found to have a linear effect on the surface area, which necessitates the study of surface energy, especially when considering the application of AZ31B alloy in aqueous environments susceptible to both wear and corrosion.

7.2.2. *Influence of LSP on wear during corrosion*

The influence of LSP on tribocorrosion was experimentally studied in terms of wear volume as shown in *Figure 7.2*. The wear after tribocorrosion on LSP processed AZ31B surfaces is observed to be drastic as compared to wear with no corrosion. The maximum wear volume is observed for the untreated surface whereas LSP-1 surface yields least wear volume after tribocorrosion. The

untreated surface experienced nearly three times more wear due to tribocorrosion than LSP-1 surface. Also, the observed increase in hardness with laser intensity (LSP-1 to LSP-2) does translate into increased wear resistance, as shown by many studies [40, 45, 51, 104, 106, 131-134]. The hardness of the AZ31B surface (VHV 62 to 72) is ~23 times less than the hardness of the counter body, alumina ball (VHV 1400 to 1500). Considering this large difference in hardness between the surface and the counter body, the plowing effect of the counter body should lead to abrasive wear on the surface during sliding. Additionally, alumina being a ceramic material has been well studied to be electrochemically inert. The absence of wear, and corrosion products on the ball was verified under an SEM as shown in *Figure 7.3*. The figure shows that observed effects of tribocorrosion are experienced by the AZ31B surface.
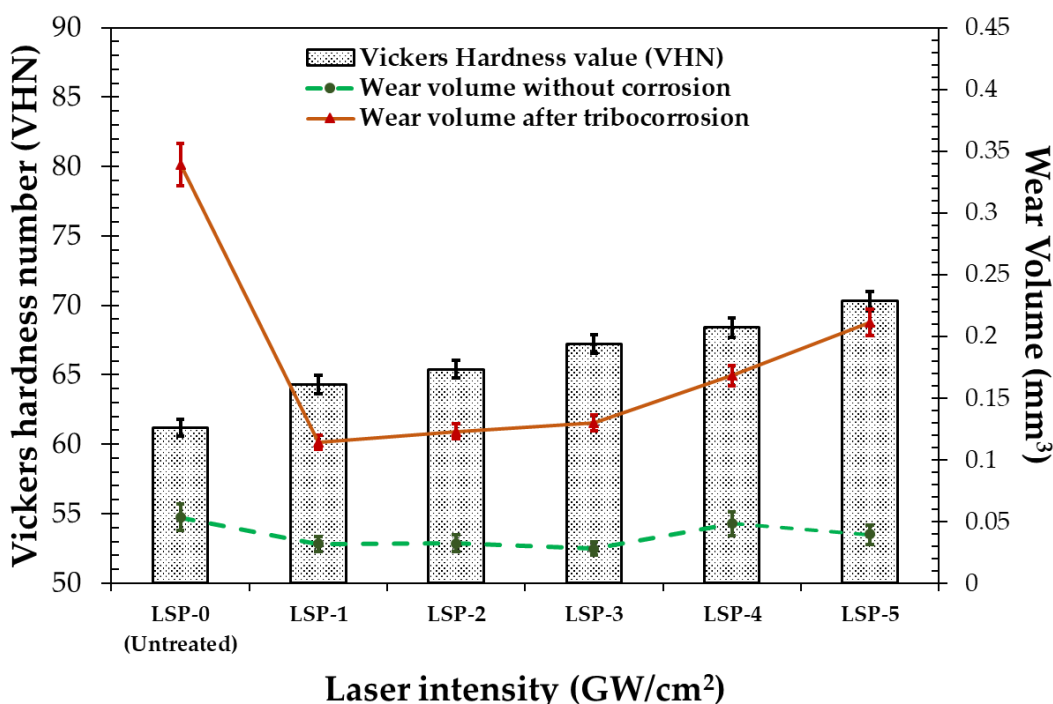
Figure 7.2: Wear volume observed on LSP processed surfaces without the influence of corrosion, and after tribocorrosion.

With increase in laser intensity, surface roughness also increases (*Figure 7.1*), which increases the exposed real surface area to corrosive environment during wear, initiating the wear-corrosion synergism. The dominant surface hardening effect of LSP at low laser intensities enhances the surfaces properties to have increased wear-corrosion synergistic resistance [40]. Whereas, an increase in wear accelerated corrosion is observed due to a dominant surface roughening effect at high laser intensities [40]. This behavior of LSP processed surface was clear from the results

where, LSP-1 processing increased the hardness by 5.1% and reduced the wear volume by 66.4%. LSP-2 processing increased the hardness by 7% and reduced the wear volume by 61.7%. LSP-3 processing increased the hardness by 10% and reduced the wear volume by 58.7%. LSP-4 processing increased the hardness by 11.8% and reduced the wear volume by 50%. LSP-5 processing increased the hardness by 15% and reduced the wear volume by 37.8%. Theoretically, the hardness is expected to increase with a decrease in the corresponding wear volume, as the laser intensity increases. But the results show that after LSP-3 the increase in hardness does not translate to decrease in wear volume [127].
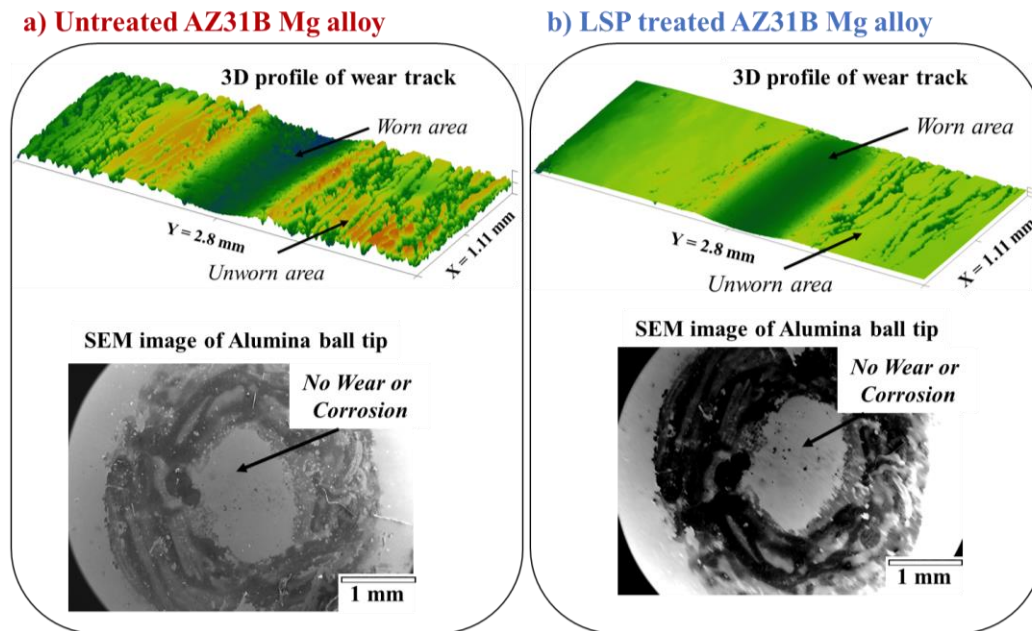
Figure 7.3: The presence of wear and corrosion on wear track and its absence on alumina ball tip after tribocorrosion as observed for a) Untreated b) LSP treated AZ31B Mg alloy.

Studies on the wear mechanism observed during tribocorrosion of LSP processed AZ31B surfaces have shown that the wear particles of micron to sub-micron size are generated during sliding [174]. The size and amount of the wear particles generated are dependent on the laser intensity used to process the AZ31B surfaces. The generated particles then define a three-body wear mechanism during sliding that is susceptible to corrosion and further accelerate the wear under the influence of tribocorrosion [127].

7.2.3. *Influence of LSP and tribocorrosion on surface roughness*

To understand the influence of surface roughness in defining the wear mechanism on LSP processed surfaces, the variation in surface roughness and wear volume due to tribocorrosion was investigated. The surface roughness, wear track, and area around the wear track was recorded post

tribocorrosion testing on each LSP surface using 3D optical profilometer. All tribocorroded surfaces were compared against their respective surface roughness and wear tracks on LSP processed (LSP-1 to LSP-5), and untreated surface (LSP-0, Untreated) of AZ31B. The observed values of surface roughness parameters S_a, S_p, S_v, S_z, and change in surface area after tribocorrosion on LSP surfaces are reported in *Figure 7.4*.

Results show that the change in surface roughness due to tribocorrosion on LSP processed surfaces can be best perceived using S_a and S_z roughness parameters [127]. The plots comparing the change in surface roughness parameters and surface area of LSP processed and tribocorroded LSP surfaces are shown in *Figure 7.4*. The linear trend of surface roughness observed for LSP processing (*Figure 7.4*a) on AZ31B did not hold true after the surfaces experienced tribocorrosion. It can be observed in *Figure 7.4*b, that tribocorrosion has a drastic effect on surface roughness, where LSP-1 surface underwent the least change (9.0%), and LSP-0 (untreated) surface underwent the highest change (31.9%) as compared to their respective conditions before tribocorrosion (*Figure 7.4*a). The results show that the surface treated with LSP-1 could resist surface degradation better than any other surfaces tested in this study, indicating that low laser intensity treated surfaces can resist mechanochemical degradation effects of tribocorrosion better than untreated or surface treated with high laser intensities [40, 127]. The variations in asperity height and surface properties of LSP surfaces post tribocorrosion has been shown to be a combination of wear, corrosion, and wear-corrosion synergistic degradation [127].

In environments susceptible to corrosion and tribocorrosion, surface roughness and surface energy play an important role. Surface energy defines how easy or difficult it is for a surface to
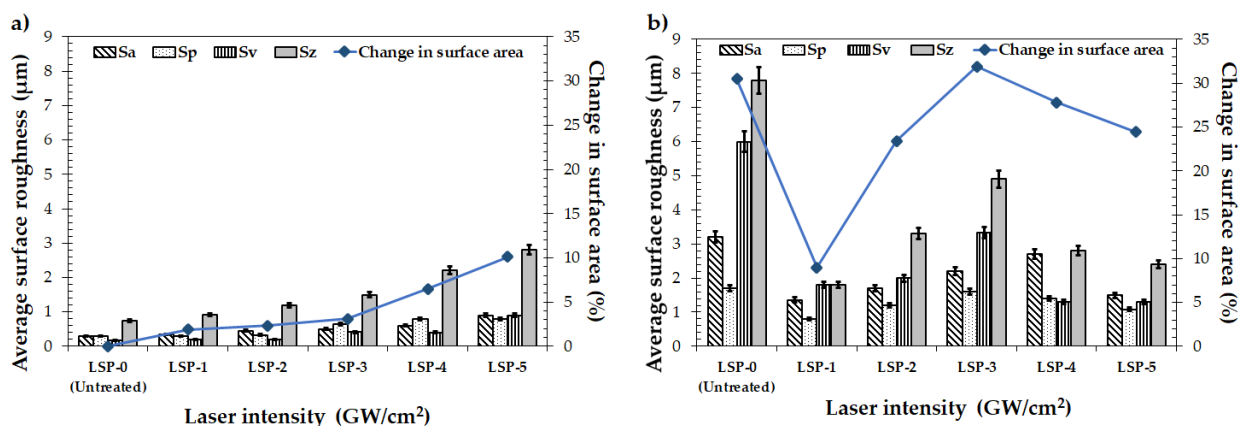
Figure 7.4: Surface roughness and area of (a) LSP processed AZ31B, and (b) LSP processed AZ31B after tribocorrosion testing.

interact with various fluids on a molecular scale and thus defines the wettability of a solid surface. The surface roughness can drastically modify the surface energy by affecting the surface area and wetting behavior. This effect of surface roughness further translates into the modification of electrochemical interactions at the interface of the surface and aqueous media that affects the tribocorrosion properties for AZ31B Mg alloy.
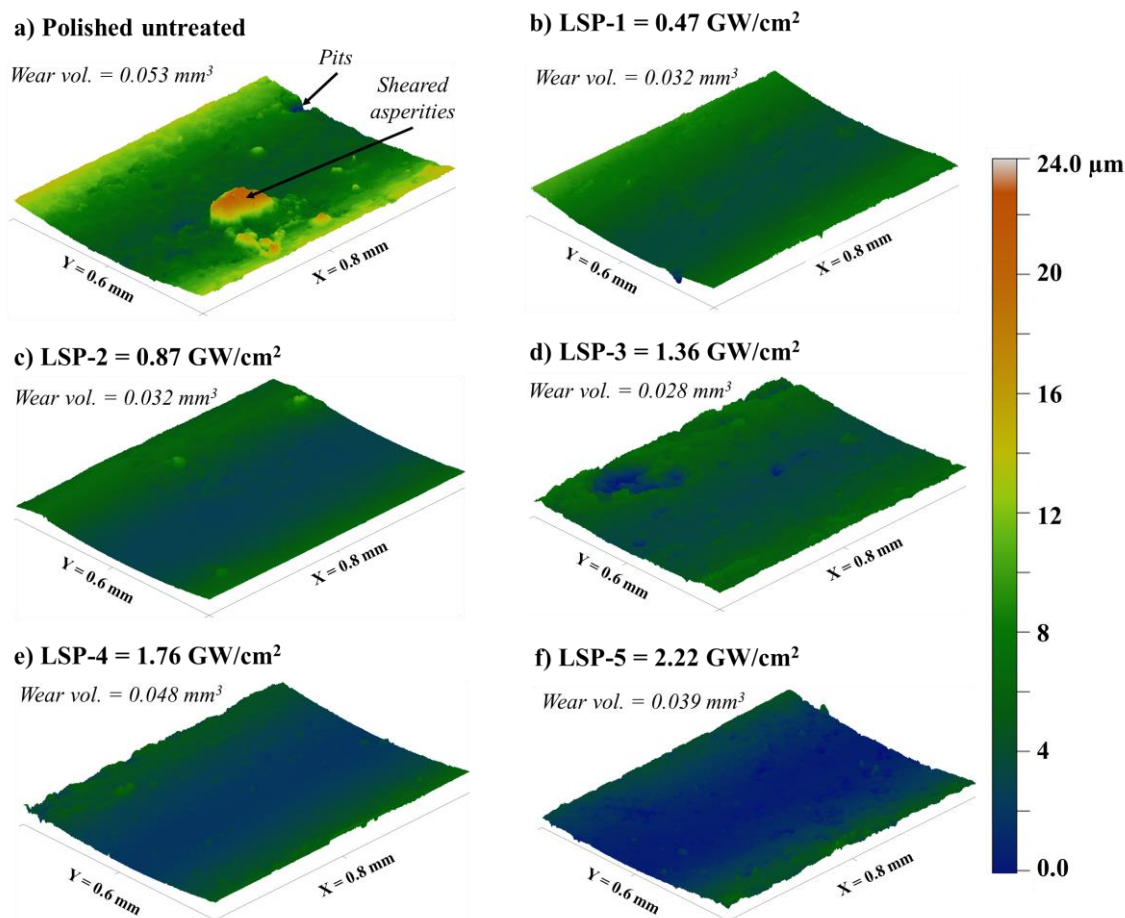
Figure 7.5: Wear track profiles after reciprocating tests without corrosion on AZ31B surfaces processed at various laser intensities (a-f).

The effect of surface roughness in defining the wear mechanism on LSP processed surfaces can be further understood by studying the wear tracks and the area around the wear track. The wear tracks without the influence of corrosion on LSP processed AZ31B surfaces (catholically polarized) are shown in *Figure 7.5*. It was observed that there was negligible change in the area around the wear track hence depicts the wear track generated due to sliding without tribocorrosion. When sliding occurs on the LSP processed AZ31B surfaces under the influence of tribocorrosion, there was a drastic increase in the wear depth and surface roughness around the wear tracks, as

shown in *Figure 7.6*. The mechanism of wear for AZ31B during tribocorrosion depends on pitting [120], and galvanic corrosion formed as a result of differential electrocatalytic mechanism [127, 206, 207]. The localized corrosion on the unworn regions in combination with the worn area forms a galvanic couple due to the change in their galvanic potentials after the initiation of pitting corrosion. The surface morphology of these galvanic couples can be very distinctly depending on the applied laser intensity (*Figure 7.6*) and wear under the influence of corrosion. The degradation effect of tribocorrosion on the surface roughness of the unworn regions is also evident in *Figure 7.6*. These mechanochemical degradations on the AZ31B Mg surface modify the surface roughness based on laser intensity during LSP and their susceptibility to tribocorrosion.

The start of corrosion on the unworn areas in the 0.6 M NaCl aqueous medium causes pits
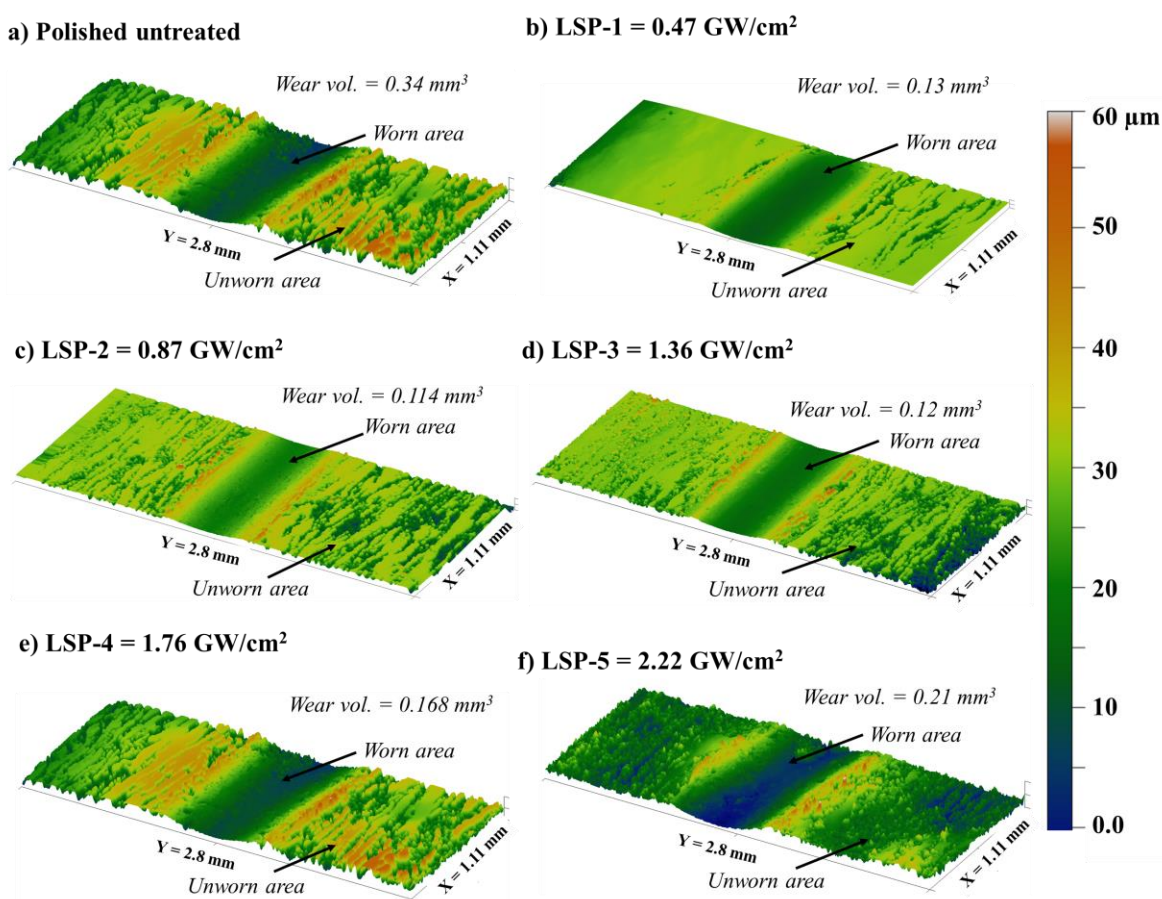
Figure 7.6: Wear track profiles after tribocorrosion testing on AZ31B treated at different laser intensities (a-f).

which result from the breakdown of oxide film during LSP [120]. A similar trend around the wear tracks in *Figure 7.6* was observed. The thin oxide film on the AZ31B surfaces was characterized

using X-ray diffraction (XRD), and the X-ray diffractogram was obtained, as shown in *Figure 7.7*. It was clear that a magnesium hydroxide (Mg (OH)$_2$) layer was present on surfaces of LSP-1 to LSP-4. The layer was absent in the case of the untreated surface and LSP-5. This indicates that the gradient of the oxide film breakdown depends on the applied laser intensity and particularly, the untreated surface shows the most pitting due to the presence of a weak oxide layer. The LSP at low laser intensities, especially LSP-1, was found to strengthen the oxide layer increasing its resilience to pitting corrosion and hence tribocorrosion. At high laser intensity, it is expected that the shock peening effect completely breaks down the oxide layer making the surface susceptible to pitting. Additionally, pitting was also evident on the wear tracks of the untreated surface and surfaces treated at high laser intensity (LSP 3 to LSP 5), as seen in *Figure 7.6*.
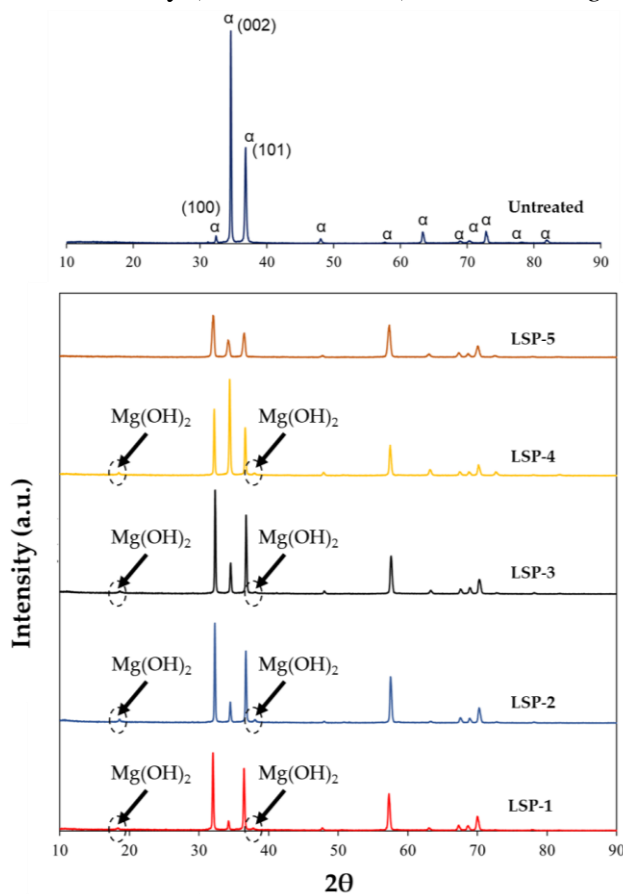
Figure 7.7: XRD of LSP processed surfaces after tribocorrosion.

These results indicate that LSP modifies the surface roughness in addition to surface characteristics and thus, causes a change in the resilience of the surface to tribocorrosion. Since surface energy and wettability of a solid are driven by surface roughness, it is necessary to understand the tribocorrosion behavior of LSP processed AZ31B Mg surfaces as a function of the

surface roughness and surface energy. Even though the influence of LSP processing on the tribocorrosion susceptibility of AZ31B has been investigated [127], the repercussions of tribocorrosion on the surface energy of LSP processed area has not been well understood. Investigating the influence of LSP on surface energy requires the wear after tribocorrosion to be studied considering the change in surface roughness and surface energy due to LSP.

7.2.4. *Influence of LSP on contact angle and tribocorrosion*

The surface characteristics, such as surface roughness and surface energy, define the interfacial area and wettability of a solid surface in aqueous environments. The interaction of the solid surface with the aqueous environment dictates the corrosion and tribocorrosion inhibition properties on engineered surfaces such as LSP. In the present study, the total surface energy and the solid-liquid interfacial surface energy of LSP processed AZ31B Mg surface with probe liquids (*Table 7.1*) – water (W), 0.6 M NaCl (N), and glycerol (G) was calculated through sessile droplet contact angle measurement method (ASTM D7334 - 08(2013)). The total surface energy was calculated based on the three-component approach developed by Van Oss et al. [129, 130]. The change in contact angles due to tribocorrosion on the LSP processed AZ31B surface is shown in *Table 7.3*.

Table 7.3: Contact angle measurements of LSP processed AZ31B surfaces before and after tribocorrosion.

Test condition	Contact angle (θ)			Surface roughness (S_a, μm)
	Water (W)	0.6M NaCl (N)	Glycerol (G)	
Untreated	74.5	87.06	75.25	0.3 ± 0.08
After tribocorrosion	53.31	54.41	73.78	3.2 ± 0.18
LSP-1	72.24	69.16	78.6	0.35 ± 0.02
After tribocorrosion	74.12	59.89	64.93	1.36 ± 0.1
LSP-2	77.8	74.78	74.16	0.45 ± 0.02
After tribocorrosion	58.5	37.42	38.61	1.7 ± 0.15
LSP-3	85.22	83.15	80.39	0.5 ± 0.05
After tribocorrosion	63.45	32.55	35.12	2.21 ± 0.13
LSP-4	85.54	80.68	75.05	0.6 ± 0.05
After tribocorrosion	68.77	39.65	52.06	2.7 ± 0.8
LSP-5	78.19	72.03	65.9	0.9 ± 0.06
After tribocorrosion	76.53	70.53	66.06	1.5 ± 0.1

The LSP processed surfaces had a high contact angle due to low surface roughness as compared to the tribocorroded LSP surfaces. Low contact angles indicated easy wetting (liquid adhesion) of the surface that increases the contact area of the surface with liquids and thus its susceptibility to corrosion. The tribocorroded surfaces had the lowest contact angles when in interface with 0.6 M NaCl as compared to the interfaces with water and glycerol. This is due to the high polar and corrosive nature of aq. NaCl that causes an increase in the liquid adhesion corresponding to the surface energy of the solid. It is this behavior of AZ31B surface, which makes its use limited in aqueous environments, and susceptible to corrosion and tribocorrosion. However, the contact angle measurements indicate that LSP processing can modify the surface roughness to increase the contact angle at the interface of AZ31B surface and aqueous mediums. Additionally, LSP is observed to increase the resilience of the surface to tribocorrosion, where it was observed that the surface could maintain a relatively high contact angle even after experiencing tribocorrosion.

7.2.5. *Influence of LSP on surface energy and tribocorrosion*

The contact angles and the surface tension data of the probe liquids (*Table 7.1*) were used to calculate the total surface energy and the solid-liquid interfacial surface energy of each LSP processed AZ31B surface. The total and the interfacial surface energy were calculated for LSP processed surfaces and compared with the resulting surface energies post tribocorrosion, as shown in

. It can be observed that the total surface energy increases after tribocorrosion for all surfaces, indicative of the surface degradation and change in surface roughness due to tribocorrosion. The increase in surface energy post tribocorrosion indicates an increased adhesion of the liquid to the surface.

The surface processed at LSP-1 experiences the least change in total surface energy and has the lowest surface energy after tribocorrosion, while LSP-3 had the highest change in surface energy due to tribocorrosion. It can be observed in *Figure 7.8*a that even though the total surface energy of the untreated and LSP processed surface is almost the same, within a range of 38-45 mJ/m^2, the solid-liquid interfacial surface energy with various probe liquids varies considerably. The untreated surface exhibits minimal variation in the interfacial surface energy irrespective of the probe liquid, whereas the surfaces after LSP exhibit a considerable change in interfacial surface energy due to the evolution of physical attributes, specifically surface roughness [137, 218].

*Figure 7.8*b shows the LSP processed surfaces under the influence of tribocorrosion experience an increase in total surface energy. This is due to the initiation and propagation of pitting corrosion that increases surface roughness. The total surface energy is observed to increase with an increase in laser intensity, but at high laser intensity (LSP-4 and LSP-5), it has been shown that the shock peening influence of LSP is high enough to restructure (plastic deformation) the surface asperities [40]. At high laser intensities, the asperities are plastically deformed to have small sharp asperities, results in lower mean surface roughness. This decrease in surface roughness due to LSP at high laser intensity increases the resilience to tribocorrosion as there is a decrease in the area prone to galvanic corrosion during wear. Hence, a decrease in surface energy is observed after tribocorrosion on high laser intensity processed surfaces (LSP-4 and 5). It has been shown that when a pitting form of corrosion initiates and degrades the surface, the surface roughness increases, causing a decrease in surface energy and an increase in the adhesion of the liquid to the surface [137]. Hence, the change in surface energy of LSP processed surfaces after tribocorrosion is attributed to the evolution of mechanochemical degradation such as wear, corrosion, and tribocorrosion.

The solid-liquid interfacial surface energy of the untreated and LSP processed surfaces with the probe liquids, observed in Figure *7.8*, decreases after tribocorrosion except for LSP-1. In the case of LSP-1, the interfacial surface energy with water increases after tribocorrosion due to pockets of air being trapped at the interface. The pockets of air trapped at the interface are because of relatively low surface degradation and minimal change in surface roughness after tribocorrosion. However, when the LSP-1 is in contact with 0.6 M NaCl, the interfacial energy decreases due to the increased polar interactions. This causes the air pockets to collapse. The decrease in interfacial energy in the case of remaining LSP surfaces is due to similar reasons (Figure *7.8*). The LSP increases the surface roughness as a function of laser intensity that causes more air to be trapped at the interface, which increases the interfacial surface energy. The change in surface roughness after LSP was found to be insufficient to cause a significant effect on the interfacial energies with the standard probe liquid-glycerol.

Further, after tribocorrosion, the drastic increase in surface roughness combined with the oxide layer break down causes the interfacial surface energy to decrease. This insight into the interfacial surface energy shows that even though the total surface energy of the LSP processed surfaces increase after tribocorrosion, their interfacial surface energy is defined by the surface roughness and polar interactions at the solid-liquid interface. These results indicate that the observed surface degradation due to galvanic corrosion is accelerated by wear in a corrosive environment such as 0.6 M NaCl and depends on the interfacial surface energy of solid with the aqueous environment.
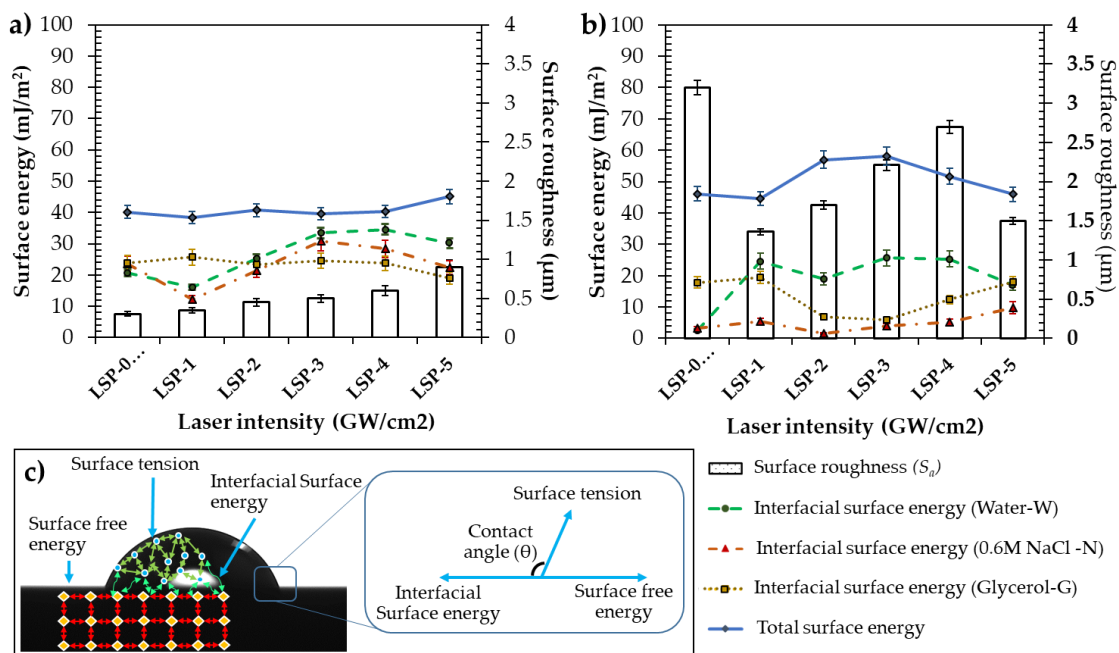
Figure 7.8: Surface energy of (a) LSP processed AZ31B surface and (b) tribocorroded LSP processed AZ31B surface. (c) Schematic representation of surface energy of solid (surface free energy), surface tension of liquid, the interfacial surface energy between the solid and liquid, and the resulting contact angle (θ).

7.2.6. *Effect of surface roughness on interfacial surface energy and tribocorrosion*

The wetting behavior of a solid surface depend on the surface roughness [219]. The surface roughness affecting the wetting behavior is defined as the ratio of actual to geometric surface area and cannot be quantified by mapping the surface profiles. In order to correlate the variation of surface roughness caused by the initiation of tribocorrosion to the surface energy, Wenzel wetting model was applied. Wenzel [220] defined a roughness factor *r,* which was the ratio of the actual surface area to geometric surface. This factor *r* can be considered in the Young's equation as:

$$r(\gamma_s - \gamma_{sl}) = \gamma_l \cos\theta$$

where, $$r = \frac{actual\ surface\ area}{geometric\ surface\ area}$$
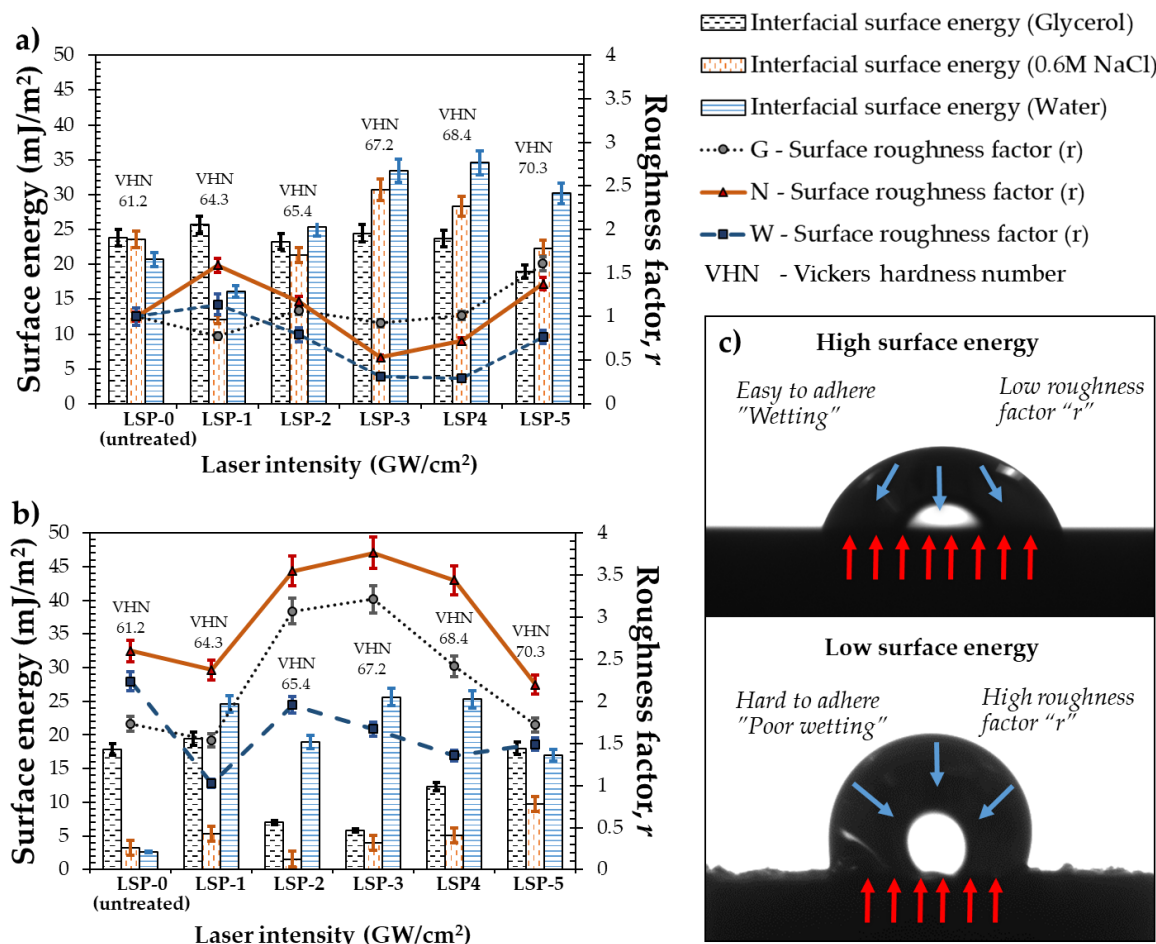
Figure 7.9: Surface roughness factor calculated with respect to the untreated surface condition for (a) LSP processed AZ31B and (b) tribocorroded LSP processed AZ31B surface. (c) Schematic representation of the correlation between the roughness factor and wetting due to the interfacial S_E.

The *r* values were calculated as shown in *Figure 7.8*, considering the *actual surface area* as the untreated surface (LSP-0, before tribocorrosion), and the *geometric surface area* as the surface area after LSP (*Figure 7.9a*), and LSP surfaces undergoing tribocorrosion (*Figure 7.9b*). These *r* values were calculated for each probe liquid to understand the effect of surface roughness on the interfacial surface energy at the solid-liquid interface. The *r* value is an indicative of the resilience imbibed by LSP processing to tribocorrosion through the modification surface roughness and surface characteristics. It can be observed in *Figure 7.9a* that the referenced untreated surface (LSP-0, before tribocorrosion) has an *r* value of 1 with all probe liquids, indicating the ideal condition (*actual surface area*) of the surface roughness. As the interfacial surface energy

decreases, the *r* value increases, and vice versa, this indicates that influence of LSP on surface roughness followed by effect of tribocorrosion on wetting behavior of the surfaces (*Figure 7.9c*). Comparing the roughness ratio for LSP processed (*Figure 7.9a*) and tribocorroded LSP surfaces (*Figure 7.9b*), it can be observed that the least change in *r* was for LSP-1 surface. This characteristic of LSP-1 is an indicative of the optimum surface characteristics obtained through LSP. A minimal change in *r* value shows that the surface characteristics are retained even after experiencing tribocorrosion. Hence, low surface energy was observed for LSP-1 even after tribocorrosion (Figure *7.8b*) indicative of enhanced corrosion and tribocorrosion resistance [40, 127].

A large change in *r* value was observed for samples LSP-2, LSP-3 and LSP-4. It occurs because of an increase in surface roughness after LSP, which causes an increase in the surface area exposed to tribocorrosion. The increase in *r* value and decrease in solid-liquid interfacial surface energy after tribocorrosion for LSP-2 to LSP-4 indicates the high susceptibility of these surfaces to tribocorrosion. Even though theoretically, the wetting should be poor when a high *r* value is observed, under the influence of tribocorrosion, the high *r* values can be detrimental since they indicate an increase in surface area. In the case of surface processed at LSP-5, due to the high laser intensity, the surface asperities undergo a large degree of plastic deformation during LSP processing, which results in small sharp asperities reducing the mean roughness [40]. Hence, a low gradient change in *r* value and interfacial surface energy is observed for LSP-5 after tribocorrosion. Even though this characteristic of LSP-5 is similar to the LSP-1 surface, the LSP-5 experiences a higher degree of surface degradation than LSP-1. This is due to the absence of an oxide layer (*Figure 7.11*), which leads to a change in surface energy after tribocorrosion.

7.3. Conclusions

The influence of LSP on surface energy and the onset of tribocorrosion was investigated on the AZ31B surfaces. Contact angle measurements were made on LSP processed surfaces and tribocorroded LSP surfaces according to the standard practice detailed under ASTM D7334 - 08(2013). The study uses a three-component approach based on Lewis acid-base surface interaction components to understand the surface energy interactions. Liquids, namely, distilled water (W), Glycerol (G), and 0.6 M NaCl (N), were used in the contact angle measurements. These liquids, specifically water and 0.6 M NaCl, simulate some of the atmospheric conditions which

dictate the corrosion properties of surfaces. The following are the conclusions resulting from this investigation:

- Low laser LSP (LSP-1) reduced the wear under the influence of corrosion by more than three times as compared to the untreated surface.

- Surface degradation due to corrosion is accelerated by wear in a corrosive environment and depends on the interfacial surface energy of solid with the aqueous environment.

- LSP-1 experienced the least change (9.0%) in surface roughness after tribocorrosion, and the untreated surface experienced the highest change in surface roughness at 31.9%.

- The change in surface roughness and liquid adhesion (wettability) due to LSP modifies the solid-liquid interfacial surface energy that depends on applied laser intensity.

- A negligible change in the roughness factor (r) is observed after tribocorrosion for low laser intensity treated surfaces which shows the resilience of LSP to tribocorrosion.

- The solid-liquid interfacial surface energy of the untreated and LSP processed surface decreases after tribocorrosion except for LSP-1.

- Magnesium hydroxide ($Mg(OH)_2$) layer was present on surfaces treated from LSP-1 to LSP-4 in decreasing order of $Mg(OH)_2$ peak intensity post tribocorrosion. The high peak intensity of $Mg(OH)_2$ indicated better tribocorroion resistance.

- The $Mg(OH)_2$ layer was absent in the case of the untreated surface and LSP-5 post tribocorrosion.

- LSP processed surfaces exhibit a high contact angle due to a decrease in interfacial surface energy.

- The LSP processed surfaces have a relatively high contact angle (low wettability) in aqueous environments post tribocorrosion as compared to the untreated surface.

- The total surface energy of the AZ31B increases after the LSP processed surface undergo tribocorrosion.

- The increase in surface energy post tribocorrosion can be attributed to the evolution of mechanochemical attributes.

Surface engineering using LSP provided evidence of the modifications possible in tribological and tribocorrosion behaviors though controlling various properties such as laser intensity, surface roughness, and surface energy. The following chapter investigates similar mechanisms of tribocorrosion and surface energy modifications using nanocomposite coatings.

Chapter 8: Tribocorrosion of nickel-graphene (Ni/GPL) nanocomposite coatings

Composite electrochemical coatings (CEC) are a versatile group of coatings generating great interest, both in research work and in practical applications—particularly in transportation, electrotechnical, food, and textile industries. CEC provides a unique technological edge to enhance the mechanical and tribological properties of the surface. Nickel (Ni) is one of the most common metal matrix used to synthesize CEC as it is characterized by superior corrosion resistance, and enhanced mechanical and tribological properties. More recently, graphene has been used in the electrodeposition of Ni composite, coatings known as Ni/GPL composite coatings, because of graphene's superior lubricating properties. Such coatings have been shown to be superior to other hard CEC that consist of chromium, boron nitride, zirconium dioxide, PTFE, etc. The coating thickness, surface morphology, and mechanical properties vary depending on the electrodeposition process parameters used in the synthesis of Ni/GPL. Additionally, these parameters affect the graphene particle distribution in Ni metal matrix, which in turn affect the coating thickness, surface morphology, and mechanical properties. Though, the effect of these process parameters on the mechanical and wear behavior of Ni/GPL composite coatings have been investigated there is a lack of fundamental understanding with respect to wear-corrosion synergism in these CEC. Most experiments test existing coatings that have been developed for either wear resistance or corrosion resistance. Coupling this to the fact that most corrosion resistant elements are not wear resistant and vice versa, these coatings, therefore perform very badly when tested under combined wear corrosion conditions. The current chapter details the tribocorrosion studies performed on Ni/GPL nanocomposite coating electrodeposited on 1020 steel substrate surface.

8.1. Electrodeposition

The nanocomposite coating Ni/GPL was deposited over steel disc samples by using pulse electrodeposition method. The thickness of coating on the samples was kept h = 10 μm. The dimensions and surface roughness of samples was 30mm × 10mm × 3mm and 0.04 μm, respectively. Three samples for each test was prepared to ensure repeatability. All samples were surface conditioned by using ultrasonic treatment before coating deposition. Bath solution containing Nickel(II) Sulfate Hexahydrate, Nickel(II) chloride, and Boric acid was used with their concentrations of 240 g/L, 57 g/L, and 42 g/L respectively. The dispersion of 4–6 nm sized

Graphene nanoparticles in a solution was performed by using ultrasonic dispersion. A magnetic stirrer was constantly used for 12 h for good particle suspension in a solution before the start of coating deposition. The NaOH and diluted H_2SO_4 were used to maintain the pH of the solution between 3.0 and 3.5. The parameters which were maintained the same throughout the deposition process are: current density = 5 A/dm^2, on-off pulse time = 30–90 ms and duty cycle = 30%. Pure nickel plate was used as anode and steel disc was used as the cathode.

8.2. Experimentation

Synergistic wear-corrosion experiments were performed by using the LMS shown in *Figure 6.2*. Three conditions of lubricating oil medium listed in *Table 4.4* were used to perform the synergistic wear-corrosion experiments. The purpose of these three conditions was to compare the synergetic wear-corrosion behavior of Ni/GPL under pure and contaminated oil conditions. Each experiment was repeated at three times to ensure repeatability of results. The experiments were performed for 15 h without interruption. Continuous monitoring of the wear volume and corrosion rates was performed during this duration. For comparative analysis, the synergistic wear-corrosion behavior of steel 1020 under all three conditions was examined. The reason for selecting steel 1020 is its significant applications in the bearing industry and its better wear-corrosion performance compared to other grades of steel [221].

The system contact was isolated in three ways during experimentation: the lubricating cup was made up of a non-conductive polymeric material; the experiments were conducted with a thin ceramic plate under the coated sample (working electrode), and the collects used inside the ball holder that isolated the carbon steel ball from the holder were non-metallic.

Reciprocating wear tests were performed against an alumina steel ball (R = 5 mm radius) at the normal force P of 15 N with a sliding speed of 0.05 m/sec with a constant 2 Hz frequency and a linear displacement amplitude of δg = 2mm using the test rig. The test rig was coupled with the test viewer software to monitor the wear-corrosion volume loss. Constant displacement amplitudes δg (stroke lengths) were applied, during the tests, characterized by the total number of wear cycles. These tribo-conditions were chosen to ensure sliding contact subject to the boundary lubrication regime and to permit retrieval of data before the coating had completely failed. ASTM G119-04 standard was followed to determine the synergism between wear and corrosion in each of the three oil conditions. A potentiostat was used to monitor the corrosion rate throughout the synergistic

wear-corrosion experiment. The reference electrode (saturated calomel) and the counter electrode were placed near the sample for accurate measurements.

At the end of the experiment the samples were kept in oil condition for 2 h to allow the surface re-passivation. After this step, the samples were surface conditioned by using ultrasonic treatment before the respective wear tracks were analyzed via 3D interferometer, Scanning Electron Microscope (SEM) and Energy Dispersive Spectroscopy EDS.

8.3. Results and Discussion

8.3.1. Synergistic wear-corrosion effect

Figure 8.1 shows the post-test EDS micrographs for Ni/GPL and steel 1020 identifying the elements and their concentration. EDS for every medium was conducted at least at five spectrum points located inside and outside the wear tracks however for illustration purpose, only one spectrum point is shown at inside and one at outside for each medium. Inside spectrum points were used to compare the wt% loss of elements inside the wear track from outside. The EDS results revealed that for both the Ni/GPL and steel, the highest wt% loss of elements inside the wear tracks was found in Medium-III and the lowest wt% loss was found in Medium-I. The comparison of EDS results for Ni/GPL and steel showed the higher wt% loss of Fe in steel wear tracks compared to Ni in Ni/GPL wear tracks in all the three mediums. For example, the wt% loss of Fe in Medium-III was 40% compared to a 28% loss of Ni. Likewise, in Medium-II the wt% loss of Fe was 30% compared 13% loss of Ni. Similarly, in Medium-I the wt% loss of Fe was 6% compared 4% loss of Ni. The lower wt% loss of Ni/GPL compared to steel in all the three mediums is linked with its microstructural properties [222]. Ni/GPL has compact, refined grains resulting in minimal transport of corrosive contaminants, water and oxygen which inhibits severe cracking avoiding under coat oxidation, and grain pull-out during wear cycles. Such behavior of Ni/GPL resulted in small wt% loss compared to steel during synergistic wear-corrosion testing.
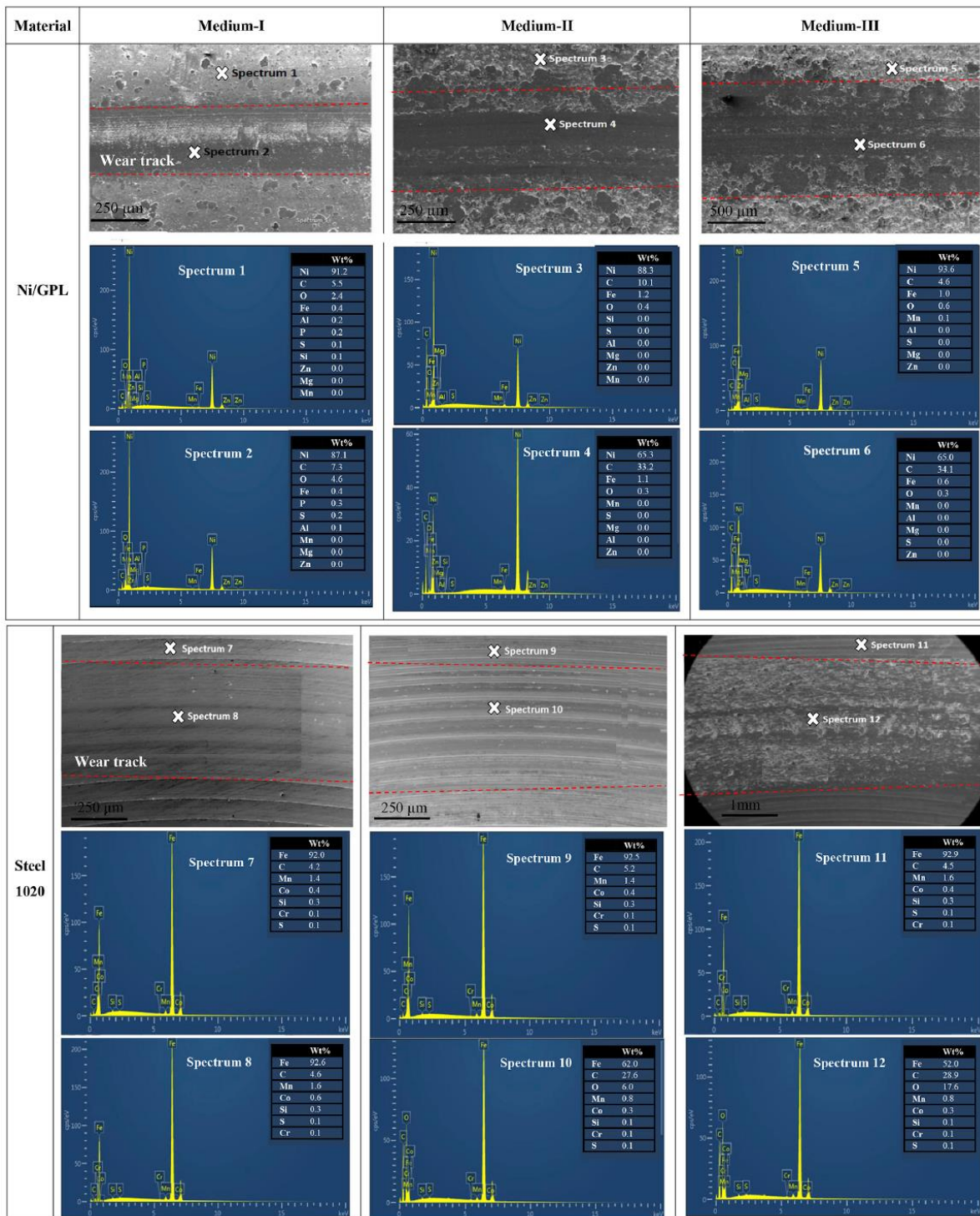
Figure 8.1: Post-test EDS micrographs for Ni/GPL and steel 1020 identifying the type of elements and their concentrations.

Another interesting EDS result is the presence of higher wt% of carbon inside the Ni/GPL wear tracks compared to steel, especially in Medium-II and III. The reason is that in the case of Ni/GPL

wear tracks, some of the carbon is coming from the breakdown of carbon chains of graphene in addition to the significant portion of carbon coming from the wear of counter carbon steel ball. The trends for synergistic wear-corrosion effect on corrosion rate ($K_{C_{W-C}}$) of both Ni/GPL and steel 1020, as shown in *Figure 8.2*(a) can be observed to constantly rise in corrosion rates right from the start of the experiment in all mediums. Compared to Ni/GPL, steel showed 18.5%, 21.5%
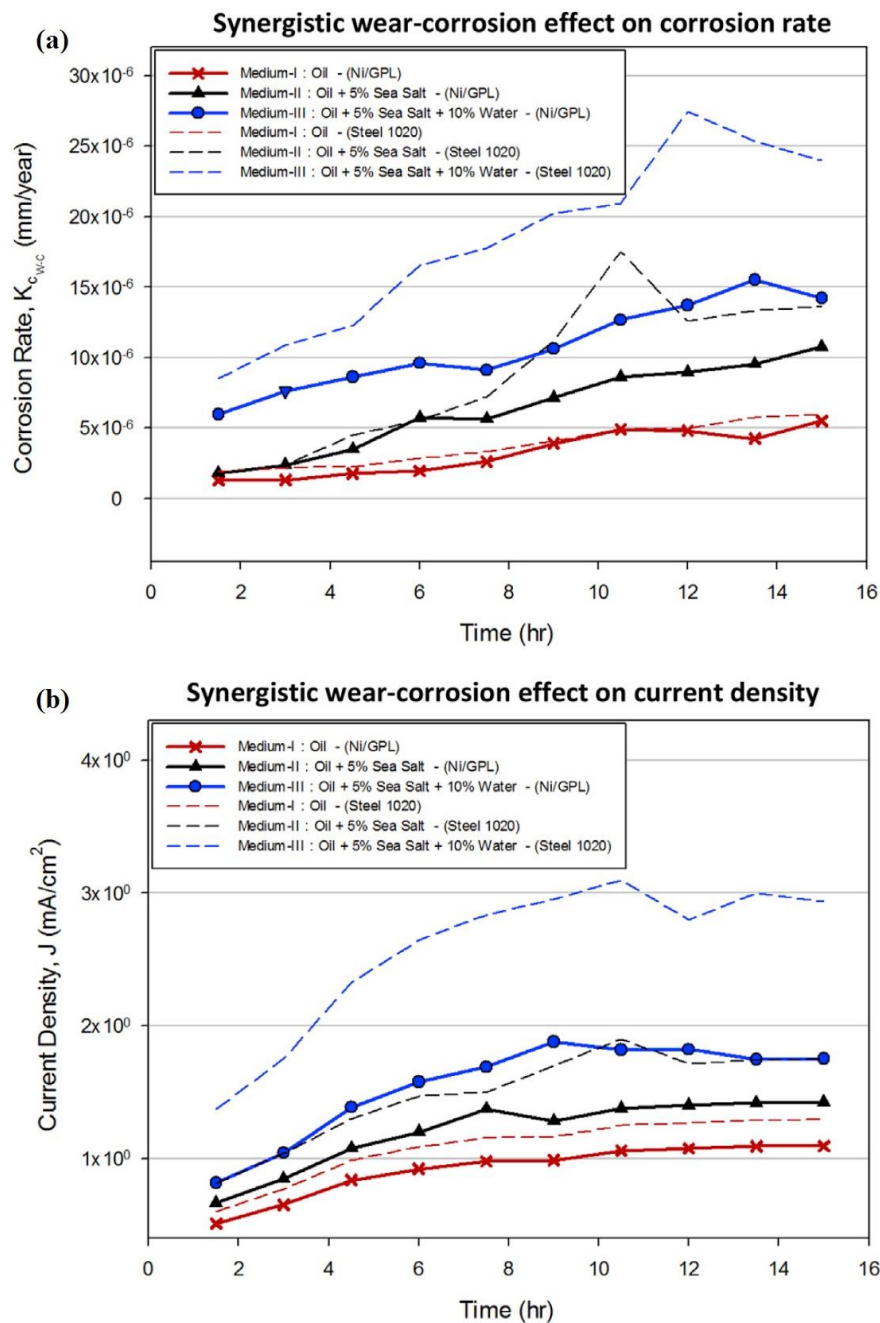
Figure 8.2: The synergistic wear-corrosion effect of both Ni/GPL and steel 1020 on (a) corrosion rates $K_{C_{W-C}}$ and (b) current densities $\overleftrightarrow{J}$.

and 67.8% higher corrosion rates in Medium-I, II and III respectively. Likewise, in *Figure 8.2*(b) the synergistic wear-corrosion effect on current densities ($\overleftrightarrow{J}$) of both Ni/GPL and steel 1020 showed that the current densities (J) stabilized after some time in all the mediums. However, similar to corrosion rates, the current densities were significantly low for Ni/GPL compared to steel. This behavior of reduction in current densities and corrosion rates of Ni/GPL is attributed to the compact and refine grain structure of Ni/GPL, which prevents oxidation (wear-corrosion) of the Ni/GPL surfaces when present at sliding contact interfaces [223].

Further, in case of steel, there were also observed periods of acceleration in corrosion rates (*Figure 8.2*(a)) and current densities (*Figure 8.2*(b)) both in Medium-II and Medium-III compared to Medium-I, which are indicative of the steel wear debris inside the wear track. However, in the case of Ni/GPL, no such accelerated periods were observed in any of the Mediums which clearly indicate that Ni/GPL remained fairly intact during testing. The significant amount of steel wear debris in Medium-II would have increased the cell medium resistance accelerating the anodic reactions. While in Medium-III, significant amount of clear corrosive compounds including iron oxide were observed because the steel wear debris rapidly reacted with the salt plus water contaminants (forming aqueous NaCl) within the oil. These corrosive compounds interfered with the sliding ball resulting in severe cavitation and starved lubrication regions (*Figure 8.3*). The
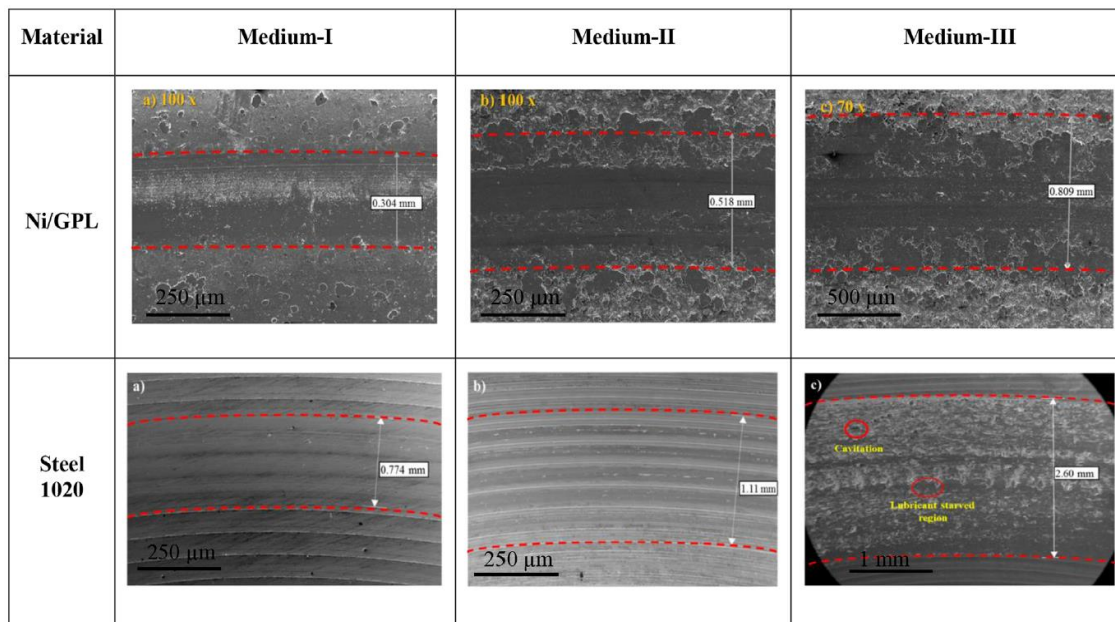
Figure 8.3: Post synergistic-test SEM images of the wear tracks widths for both Ni/GPL and steel 1020 under all the three lubricating oil conditions.

influences of lubricating oil contamination on the width of wear tracks were also analyzed by using SEM, as shown in *Figure 8.3*. It can be clearly seen that Ni/GPL exhibited 0.304 mm, 0.518mm and 0.809mm wide wear tracks in Medium I, II and III respectively which were significantly small compared to 0.774 mm, 1.11 mm and 2.6 mm steel wear tracks. Moreover, Ni/GPL did not show any visible anomalies along the wear tracks for Medium-II and III, whereas the steel wear tracks exhibited significant cavitation because of contaminants at the sliding ball interface which accelerated the synergistic wear-corrosion effects during testing.

8.3.2. *Evolution of corrosion rate without wear*

The evolution of corrosion rates (K_C) of both Ni/GPL and steel 1020 without wear showed fairly linear behavior throughout for all the mediums, as can be observed in *Figure 8.4*. For Ni/GPL, the corrosion rates for all the mediums almost overlapped, showing that Ni/GPL was minimally affected by contaminants. This behavior of Ni/GPL can be attributed to its compact, refined grain which inhibits the transport of corrosive contaminants, in turn preventing intergranular corrosion. However, the corrosion rates of steel for all the mediums, especially Medium-II and III were significantly high. It is worth noting that the corrosion rates of steel without wear did not show accelerated periods of corrosion rates as were seen previously in the case of synergistic wear-corrosion $K_{C_{W-C}}$ experiment (*Figure 8.2*(a)). This clearly indicates that the steel 'wear debris' during synergism were responsible for accelerated corrosion rates.
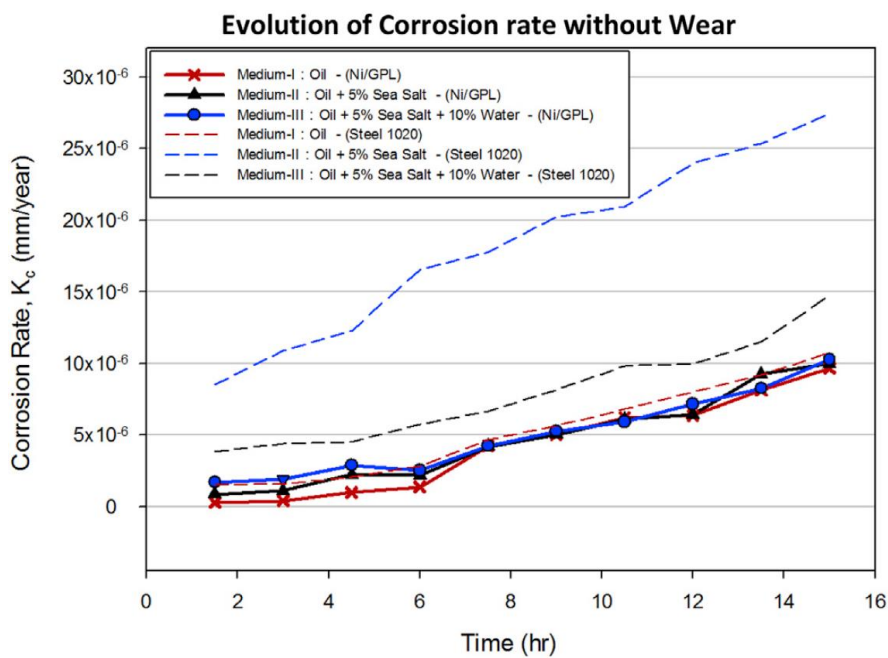
Figure 8.4: Evolution of corrosion rates K_C of both Ni/GPL and steel 1020 without wear.

8.3.3. *Evolution of wear rate without corrosion*

The wear rates (K_V) without corrosion for both Ni/GPL and steel 1020 were observed only in Medium-I as it was an uncontaminated medium. *Figure 8.5* shows the increasing trends of wear rates of Ni/GPL and steel with increasing time and Archard loading factor *W*. Where, Archard factor (also known as the total dissipated energy during wear cycles) is defined as the multiplication of normal force (P) with total sliding displacement (δ) i.e. P (N) x δ (m). Therefore, the accumulated Archard factor ($\sum W$) is written as [224]:

$$\sum W = \sum_{i=1}^{N} W_{(i)}(Nm) \; ; \; where \; W_{(i)} = 4\delta g_{(i)} P_{(i)}(Nm)$$

where $W_{(i)}$ denotes the dissipated Archard factor at *i*th wear cycle. The corresponding number of wear cycles (*i*) in *Figure 8.5* indicate that wear actually began beyond 8k cycles for both Ni/GPL and steel. After 8k cycles, the wear rates of the both materials for remaining cycles were observed to be increasing steadily with time but as obvious, during this period the wear rate of steel was quite high compared to Ni/GPL. *Figure 8.5* also shows linearly rising trends of wear volumes (V)
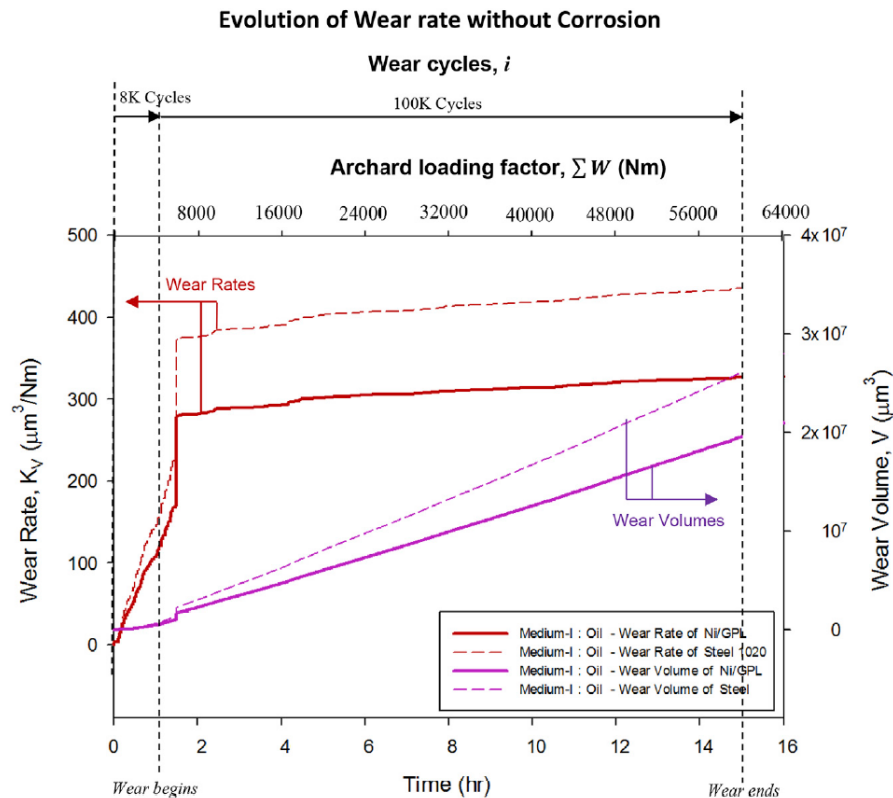
Figure 8.5: The evolution of wear rates K_V without corrosion for both Ni/GPL and steel 1020 under uncontaminated oil lubrication condition (Medium-I) only

for Ni/GPL and steel. Wear volume is measured from wear rate (K_v) and accumulated Archard factor ($\sum W$) by using a conventional Archard description as:

$$\Delta V = K_v \times \Delta \left(\sum W \right) \quad (\mu m)^3$$

Table 8.1 plots the evolution of normalized 'wear profiles' and normalized 'wear depth kinetics profiles' at various stages of wear degradation for Ni/GPL and steel. The wear profiles showed the

Table 8.1: The wear depth profiles at different *i*th wear cycles of Ni/GPL and steel in addition to a 3-D interferometric image indicating the type of wear delamination. The Table also shows the computed wear depth kinetics profiles corresponding to wear profiles at different *i*th wear cycles of Ni/GPL.

Material	Wear depth profiles, Interferometric image and wear depth kinetics profiles
Ni/GPL	

Material	Wear depth profiles, Interferometric image and wear depth kinetics profiles
Steel 1020	

Wear depth profiles

3-D Interferometric image –Micro-cutting

Wear depth kinetics profiles

"U-shaped" behavior having a maximum wear depth always at the center (x = 0). It can be seen that at i = 10,000th cycle, Ni/GPL showed the normalized wear depth = 0.19 while steel showed considerably high normalized wear depth = 0.33. The wear profiles are the moving averages of measured surface interferometric values at various cycles. One such schematic example of interferometric wear profile is shown in red at i = 10,000 for Ni/GPL.

The 3-D interferometric image for Ni/GPL and steel at i = 10,000th cycle in *Table 8.1*, clearly indicates that Ni/GPL exhibited less severe micro-plowing wear deformation compared to severe micro-cutting in steel. *Table 8.1* also displays the computed wear depth kinetics $h_{(i)}(x)$ for Ni/GPL and steel at different wear cycles computed by using corresponding wear profiles. The following incremental equation was used for the development of wear depth kinetics profiles (where Δi is a single wear cycle):

$$h_{(i)}(x) \approx \frac{\Delta h}{\Delta i} = \frac{h_{(i)}(x) - h_{(i-\Delta i)}(x)}{\Delta i}$$

A major decrease of the normalized wear depth kinetics profile corresponding to increasing cycles is observed. For example, at $i = 8000^{th}$ cycle, the normalized wear depth kinetics for Ni/GPL was 0.21 compared to steel (0.08). One more interesting thing is the evolution behavior of the normalized wear depth kinetics profile initiating with the elliptical shape decreasing to the Hertzian shape and finally becoming a quasi-flat shaped. The contact extremities in quasi-flat distribution ($i = 8000^{th}$ cycle and onwards) exhibit the type of wear deformation, for example, micro-plowing in Ni/GPL showing slightly heightened contact edges while micro-cutting in steel is showing almost full flat distribution.

8.4. Conclusions

This work analyses the synergistic wear-corrosion performance of nanocomposite coating Nickel-Graphene (Ni/GPL) under pure and contaminated lubricating oil conditions, listed in *Table 8.1* and compares it with un-coated steel 1020. The following points have been concluded from this study:

- It was observed that for both Ni/GPL and steel the synergistic wear-corrosion effect was negligible in an uncontaminated oil medium.
- In Sea water contaminated oil medium, the effect of wear-corrosion was significantly evident in steel as compared with Ni/GPL.
- Ni/GPL resulted in small wt% loss compared to steel during synergistic wear-corrosion testing.
- The Ni/GPL has compact and refined grain resulting in minimal transport of corrosive contaminants, water, and oxygen which inhibits severe cracking avoiding under coat oxidation, and grain pull-out during wear cycles.
- The evolution of corrosion rates during tribocorrosion for Ni/GPL was least as compared to steel and Ni coating.

Chapter 9: Effect of Surface energy of Ni/GPL nanocomposite coating on tribocorrosion behavior

Composite electrochemical coatings (CECs) are some of the most widely investigated coatings due to its versatility in tailoring physio-mechanical and tribological properties. The effectiveness of the CECs for tribological applications is dependent on the solid–liquid interfaces. The active and passive nature of the contact boundaries for a CEC with a solid/liquid interface is defined by the surface energy of these boundaries. Unless the effect of surface energy on the tribological properties of the CEC are understood, it is not possible to get a holistic picture on properties, such as corrosion and tribocorrosion. The present study investigates the surface energy of optimized nickel (Ni) and Ni–graphene (Ni–Gr) coatings and their effect on the dynamic friction and wear behavior. It was found that the addition of Gr to the Ni coating in small quantities could decrease the polar component of surface energy significantly than the dispersive component. The presence of Gr in the coating was able to reduce the wear while providing low friction. The Ni–Gr coating exhibited low surface energy that includes weak adhesive forces, which can prevent embedding of the wear particles during sliding.

9.1. Materials and Methods

9.1.1. *Electrodeposition*

The Ni and Ni-Gr nanocomposite was deposited on the $25 \times 25 \times 15$ mm^3 1045 steel plate by electrodeposition in their respective Ni and Ni-Gr bath solutions. The detailed material composition of the 1045 steel is given in *Table 5.1*. The constituents of Ni and Ni-Gr bath solution are given in *Table 9.1*. In addition to similar chemical composition as of Ni, Ni-Gr electrochemical bath consists of 0.1 g/L of Gr nanoplatelets [72]. The Gr nanoplates used in this study are 6-8 nm thick layers with the length ranging from 5-25 µm. The details of the bath solution are provided in several previous studies, which can vary in the concentration of solvents based on the substrate material [72, 94]. Before the deposition process, the steel samples were ground against the sandpapers of grit size 120, 240, 400, 600, 800, and 1000 to remove deep scratches and then were wet polished with diamond suspension polishing mixtures of sizes 15, 6, 3, and 0.05 µm on a polishing wheel. The polishing of steel was completed with a final polish using colloidal silica. To ensure uniformity of surface finish, each surface was profiled using a 3D optical profilometer (Rtec Instruments). The profiling of the surface ensured that an average surface roughness (S_a) of 0.1 ±

0.05 µm was obtained after the polishing. The surface roughness measurements were recorded again after the plating process.

Pure nickel plate (99.5%) was used as an anode, and a rectangular steel sample was used as a cathode in the electrochemical setup. During the electrodeposition process, the following parameters were set throughout the process: current density = 5.66 A/dm^2, On-Off pulse time = 10 ms, and duty cycle = 20%. The pH of the bath was maintained between 3.8 and 4.0 at a temperature of 40 °C. A 10% H_2SO_4 was used to decrease the pH levels as needed. The electrodeposition was carried out for 50 min. These optimized parameters are based on the author's prior work on electrodeposited Ni-Gr coatings [94]. Three samples of each coating were prepared to ensure the repeatability of the process. An average thickness of ~10 µm is obtained for all Ni and Ni-Gr coatings.

Table 9.1: Constituents of Ni and Ni-Gr plating bath solution.

Plating bath composition	Quantity (g/L)
$NiSO_4 \cdot 7H_2O$	26.26
Na_2SO_4	56.81
H_3BO_4	18.54
Graphene (Gr)	0.1

9.1.2. Surface characterization

The phase and structural analysis of the Ni and Ni-Gr coatings was performed using Raman spectroscopy. Raman spectroscopy was carried out using a Thermo Scientific DXR Raman Microscope equipped with a 5 mW 532-nm laser averaging multiple area map points taken at 100x magnification. The Raman spectroscopy provides wavelength stability with less than 1 cm^{-1} for over 12 hr period. Spectra were collected in the 1000–3500 cm^{-1} spectral region, with a grating resolution of 900 lines/mm. The exposure time was 2 s for 26 scans of 1 µm step along the line and 3 scans over 0.1 µm depth at each point.

9.1.3. Friction and wear tests

Reciprocating wear tests were performed on the 1045 steel, Ni coating, and Ni-Gr coating. The tests were performed under dry laboratory conditions (20% RH, 24 °C) with a 2N constant normal load against a ceramic ball (Silicon Nitride (SiN)) of 11.5 GPa hardness. A sliding speed of 5 mm/s was maintained for a sliding distance of 4200 m. This test was chosen over other conventional

tribological testing as it can provide better insights into the interface kinematics during the reciprocating form of sliding. The experiments were performed on a Rtec Multi-function Tribometer, equipped with a robust high-resolution capacitance load sensor which can apply the normal load and measure the resulting friction force during sliding. Each test was performed three times to ensure repeatability. After the wear tests, the wear tracks were profiled using the 3D optical profilometer to investigate the wear track, and hence the wear performance.

9.1.4. Hardness tests

Nanoindentations tests were performed on all the samples using a Triboindenter TI950 (Hysitron) equipped with Berkovic probe. A maximum force of 10 mN was applied, and the hardness values were measured over ten different locations on the sample. The study reports the average of these hardness values with their standard deviation.

9.1.5. Contact angle and surface energy measurements

The surface energy and the interfacial tension between the composite surface and the liquids were evaluated using contact angle measurements with rame-hart contact angle Goniometer. Liquids, namely, distilled water and 3.5% NaCl were used in these measurements as these liquids simulate some of the atmospheric conditions which dictate the corrosion properties of coatings and surfaces. The sessile drop method was used, with distilled water and 3.5 % NaCl as testing liquids to calculate the surface energy and its polar and dispersive components [217]. The contact angle of the steel, nickel, and nickel-graphene coated surfaces were measured using both liquids. The left and right contact angles of the sessile droplet were recorded and averaged over ten trials to find the average contact angle for each surface. All measurements had a difference in the left and right contact angles less than 2°. These steps ensured the repeatability and reliability of the contact angle measurements.

9.2. Results and Discussion

9.2.1. Raman spectroscopy

The Raman spectra for Ni and Ni-Gr coatings at 532 nm laser excited at 5 mW for the range of $100 - 3500$ cm^{-1} is shown in *Figure 9.1*. In the Raman spectra of Ni coating, there were no significant peaks observed, whereas for the Ni-Gr coating five peaks were observed at 1404 cm^{-1} (D-mode), 1583 cm^{-1} (G-mode), 1620 cm-1 (D'), 2775 cm^{-1} (2D-mode), and 3085 cm^{-1} (D+G-

mode) [225-227]. This confirms the inclusion of Gr in the electrodeposited Ni-Gr composite coating.
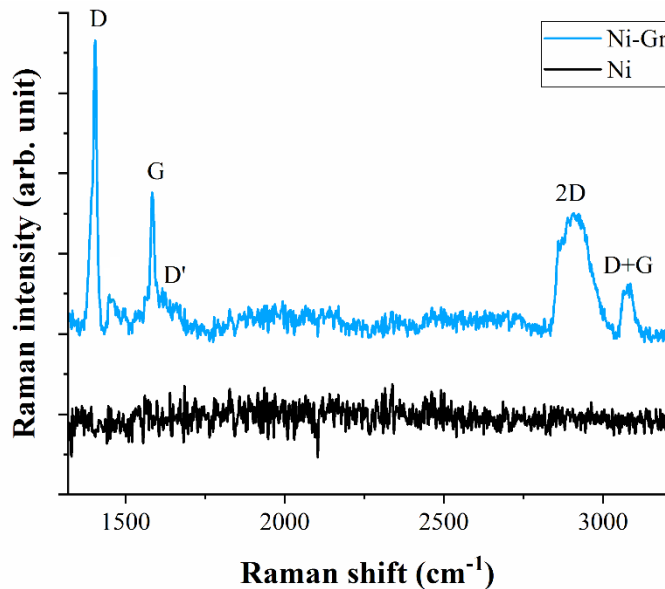
Figure 9.1: Raman spectra of Ni and Ni-Gr coating on 1045 steel surface with a 532 nm excitation laser wavelength.

The D and 2D-peak positions are dispersive in nature as they are dependent on the laser excitation energy [226]. The high intensity of the D peak indicates the presence of a large number of nucleation centers on the surface [228, 229]. The low-intensity D'-peak shows that the coating has minimal impurities or there are minor surface charges in the Gr. The 2D-band confirms the graphitic sp^2 phase, and the low intensity of the 2D-peak indicates the multi-layer nature of Gr used in the present study. The depth-based scans of 0.1 µm step on the Ni-Gr coating showed a similar intensity of G-band, as shown in *Figure 9.1*. This observation indicates the presence of Gr in the coatings below the surface. The distribution of Gr in the coating thickness should enable the coated surface to maintain consistent surface energy even after undergoing wear.

9.2.2. *Surface roughness*

Studies [141, 230] have shown that the surface roughness of the substrate can directly influence the electrodeposited coating characteristics, such as coating adhesion, and surface finish. Studies have shown that the surface roughness influences the interface toughness, which limits the coating thickness [231]. Hence, the surface roughness can be a defining factor in optimizing the coating characteristics. To understand the effect of graphene on the electrodeposit Ni-Gr coating characteristics, it is necessary to achieve consistent surface roughness on the steel substrate before

the coating as well as after the coating. The surface profiles of the polished steel substrate are shown in *Figure 9.2*a. The thickness and the average surface roughness (S_a) of the electrodeposited Ni and Ni-Gr coatings obtained with the parameters described above are illustrated in *Figure 9.2*b and *Figure 9.2*c, respectively.
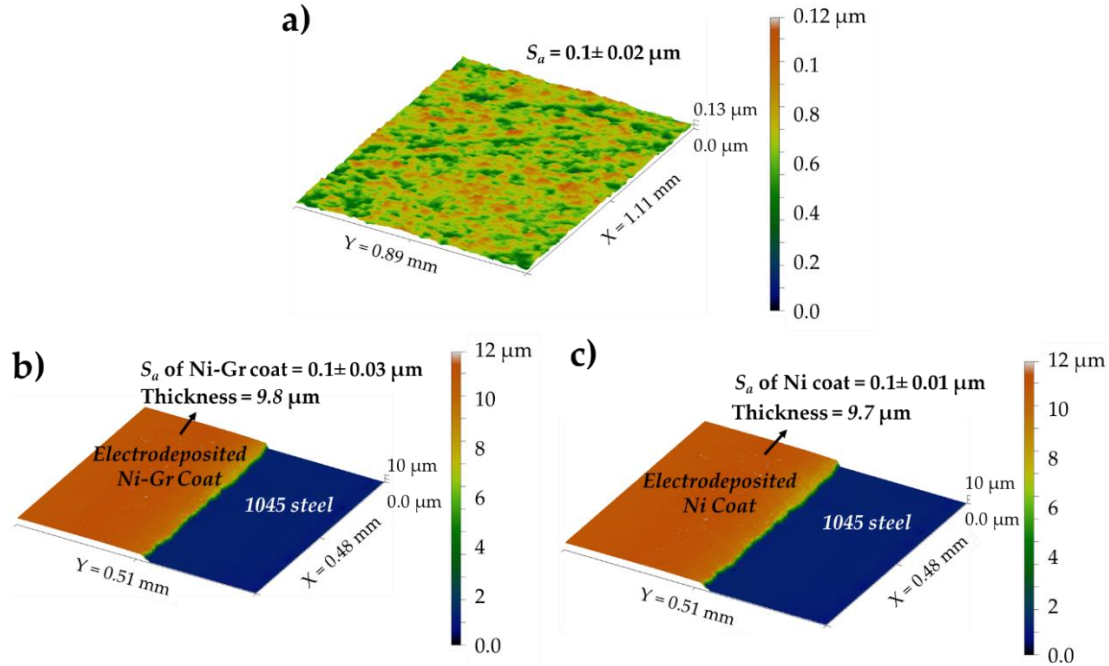
Figure 9.2: 3D surface profile and average roughness of (a) 1045 steel substrate, (b) Ni coating, and (c) Ni-Gr coating.

The Ni and Ni-Gr coating thickness as obtained are ~ 9.8 and ~ 9.7 µm, respectively. It can also be seen that the S_a of all the samples before and after the coating is within the range of 0.1 ± 0.05 µm. Hence, the comparison of these coatings for their tribo-metallurgical behavior is rational. The surface roughness and profile data indicate an excellent finish of electrodeposit coatings with a surface roughness that corresponds to the substrate surface.

9.2.3. *Surface energy of the coatings*

The surface energy of the coatings was calculated using Fowkes theory [232]. Based on Fowkes theory, the interactions between the surfaces and liquids are given as follows:

Young's equation of surface energy:

$$\sigma_S = \sigma_{SL} + \sigma_L \cos\theta \tag{1}$$

where, σ_L is the overall surface tension of the wetting liquid, σ_S is the overall surface energy of the solid, σ_{SL} is the interfacial tension between the surface and the liquids.

Also, Dupre's definition of Adhesion Energy:

$$I_{SL} = \sigma_S + \sigma_L - \sigma_{SL} \tag{2}$$

where, I_{SL} is the energy of adhesion per unit area between a liquid and a solid surface. By applying the Fowkes theory, adhesive energy between a solid-liquid can be separated into interactions between the dispersive components and between the non-dispersive (polar) components of the two phases. By separating the dispersive and polar components in the above two equations, the primary equation of the Fowkes' surface energy theory is obtained as:

$$\sqrt{(\sigma_L^D)(\sigma_S^D)} + \sqrt{(\sigma_L^P)(\sigma_S^P)} = \frac{\sigma_L(\cos\theta + 1)}{2} \tag{3}$$

where, $\sigma_L^P, \sigma_L^D, \sigma_S^P$ and σ_S^D are the polar and disperse components of the surface energy for liquid and solid. The following values were used to consider the contribution of water and NaCl solutions to the surface energy: distilled water surface tension (σ_{L1}) = 72.10 mN/m (σ_{L1}^P= 52.20 mN/m; σ_{L1}^D= 19.90 mN/m), and 3.5% NaCl (σ_{L2}) = 73.76 mN/m (σ_{L2}^P= 22.20 mN/m; σ_{L2}^D= 51.56 mN/m) [233]. The contact angle of the steel, nickel, and nickel-graphene coated surfaces were measured using both liquids. The contact angle of distilled water and 3.5% NaCl measured on 1045 steel surface, Ni coating, and Ni-Gr coating is shown in *Figure 9.3*.
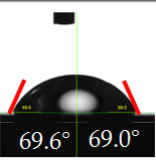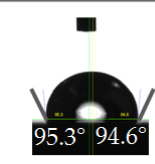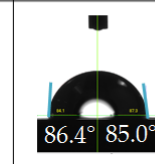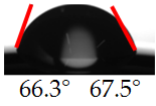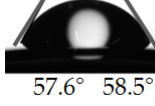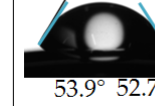
Liquid interface	1045 steel	Ni Coat	Ni-Gr Coat
Distilled water	69.6° 69.0°	95.3° 94.6°	86.4° 85.0°
3.5% NaCl	66.3° 67.5°	57.6° 58.5°	53.9° 52.7°

Figure 9.3: Image of the droplets of distilled water and 3.5% NaCl on 1045 steel, Ni coating, and Ni-Gr coatings.

The measured contact angle, as well as the calculated surface energy values of 1045 steel, Ni coating, Ni-Gr coating, are given in *Table 9.2*. These measurements were used in the Fowkes' surface energy calculations to obtain two linear equations (one equation for each liquid) correlating the dispersive (σ_S^D) and polar (σ_S^P) components of surface energy for the given solid surface. The variation in calculated surface energy values with its components for each surface are shown in *Figure 9.4*.

Table 9.2: Average contact angle of distilled water and 3.5% NaCl on 1045 steel, Ni coating, and Ni-Gr coating.

Surface	Contact angle (θ)		Surface energy (mJ/m²)		Overall surface energy (mJ/m²)	Adhesive energy (mJ/m²)	
	Distilled water	3.5% NaCl	Dispersive component	Polar component		Distilled water	3.5% NaCl
1045 steel	70.6	66.3	26.83 (26%)	77.44 (74%)	104.27 (100%)	2.97	2.58
Ni Coat	95	58.5	18.06 (12%)	129.96 (88%)	148.02 (100%)	13.52	12.75
Ni-Gr Coat	86	52.9	5.15 (20%)	20.25 (80%)	25.4 (100%)	11.92	12.53

The results indicate that Ni-Gr coating has overall surface energy, which is about 82.84 % less than the Ni coating, while 75.6% less than the steel substrate. The presence of graphene is found to decrease the polar component of surface energy significantly than the dispersive component. It can also be observed that even though Ni and Ni-Gr coating shows a hydrophobic nature, they can show about a 38% decrease in contact angle when wetted by a 3.5% NaCl solution. Thus, the dispersive and polar components impact on the surface energy is evident from these data. The contact angle does not depend on the thickness of single-, bi-, and multilayer Gr [234, 235]. Hence, small quantities of Gr present on the surface is sufficient to influence the surface energy.
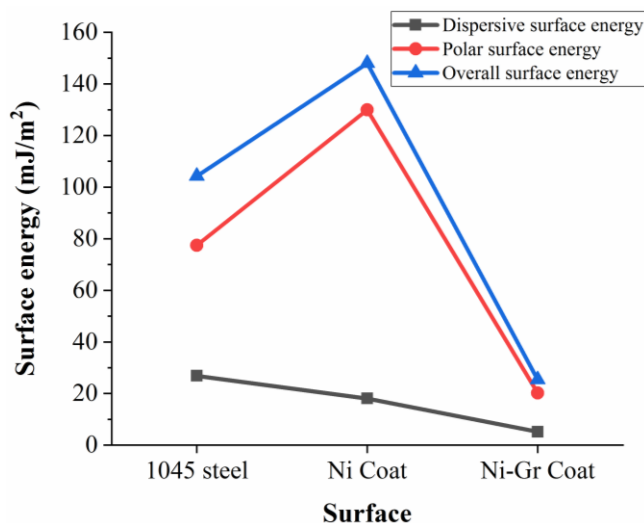
Figure 9.4: Surface energy and its components (dispersive and polar) calculated for 1045 steel, Ni Coating, and Ni-Gr coating.

According to Fowkes, dispersion interactions relate to London dispersion, arising from the electron dipole fluctuations, and the polar interactions. The low polar surface energy, in addition

to the hydrophobic nature of Ni-Gr coatings, indicates that the London dispersion forces are weaker at the coating-fluid interface [236]. This shows that even though fluids with high dispersion surface energy can wet the Ni-Gr coating, the adhesion energy between the fluid and the surface can be low as can be observed in *Figure 9.4*. This wetting property of Ni-Gr coating is significant when used in lubricated environments where high wettability with low polar surface energy surfaces is beneficial.

9.2.4. Hardness

Nanoindentations tests were performed on the 1045 steel, Ni coating, and Ni-Gr coating using a Hysitron Triboindenter TI950 with Berkovich probe. A maximum force of 10 mN was applied to measure the hardness of the substrate and coatings. The hardness of the surfaces of substrates and the coatings are given in *Table 9.3*. A maximum indentation depth of 0.283 µm was observed during the indentations. The hardness of the substrates was also compared against the hardness of the counter body, SiN ball. The surface of the counter body was over 40% harder than the Ni and Ni-Gr coatings. Considering this large difference in hardness between the surface and the counter body, the plowing effect of the counter body should lead to abrasive wear on the surface during sliding. It can be observed that the steel surface has a low hardness as compared to the coatings, while both Ni and Ni-Gr coatings had similar hardness. The increased hardness indicates that impervious and strong bonding of coating is obtained on the substrate. Also, the similar hardness of both Ni and Ni-Gr coatings shows that graphene in low volume fraction does not necessarily change the mechanical properties of the coating. Additionally, the large standard deviation (0.949) in the hardness of Ni coating as compared to the Ni-Gr coating may be due to the minor inconsistencies in the electrodeposited layers of Ni. These inconsistencies may have been minimized by the addition of Gr where the standard deviation of hardness is only 0.425. These observations indicate that Gr is a useful tribological material to modify the surface energy with enhanced structural homogeneity of the Ni-Gr electrodeposit.

Table 9.3: Hardness of steel substrate and the coatings.

Surface	H (GPa)	Std. Dev.
1045 steel	4.632	0.443
Ni Coat	6.606	0.949
Ni-Gr Coat	6.769	0.425
SiN ball	10.82	0.396

9.2.5. *Friction and wear*

Reciprocating sliding tests were performed to understand the friction and wear behavior of coating in correlation with the surface energy. The coefficient of friction and wear data were recorded by sliding SiN ceramic ball over the 1045 steel, Ni coated, and Ni-Gr coated surfaces. A normal load of 2N on the ceramic ball of 3 mm diameter was applied over a sliding distance of 4200 m. The maximum Hertzian contact pressure under the static condition at the interface of the tribo-pair, SiN and 1045 steel, was calculated to be 1432.5 MPa with an expected maximum penetration depth of 0.012 mm [237]. The evolution of the coefficient of friction (COF) during sliding is shown in *Figure 9.5* An average COF of 0.42 ± 0.06, 0.372 ± 0.09, and 0.194 ± 0.04 was observed for 1045 steel, Ni coating, and Ni-Gr coating, respectively. It can be observed that as sliding progresses, the COF increases for 1045 steel (18% increase over a distance of 4200 mm) and Ni coated surface (12% increase over a distance of 4200 mm), while it decreased by 11% for Ni-Gr coating.
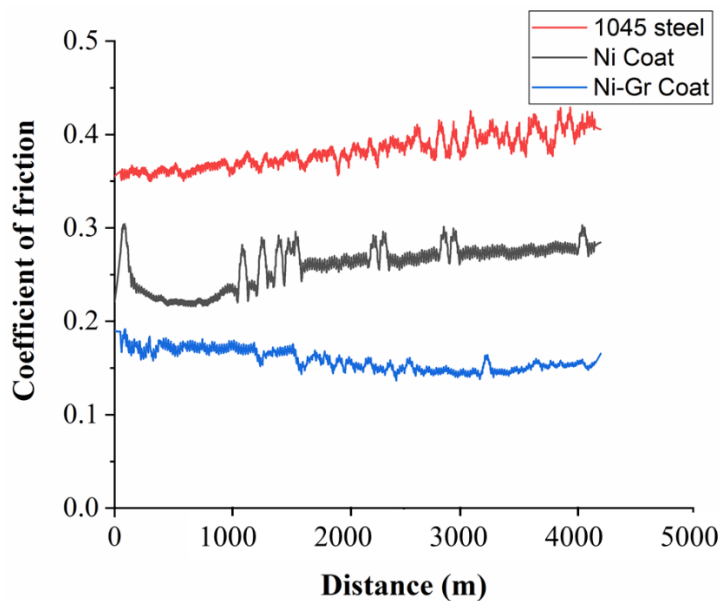
Figure 9.5: Evolution of the coefficient of friction when sliding on 1045 steel and coated surfaces.

The sliding conditions generate wear debris of varying sizes depending on the surface. In the case of 1045 steel, the wear has been shown to yield micro-sized particles which can enter the asperity interface and induce a degenerative third-body-effect [192, 238-240]. These micro-sized particles are less spherical and abrade the contact surface. Thus, the wear mechanisms under such situations would be abrasive wear. In the case of Ni coating, the slow electrodeposition leads to

high nucleation with small refined grains that allows it to generate sub-micron sized particles during wear. These sub-micron sized particles lead to more spherical that will roll off easily at the interface without abrading the surfaces, leading to a stable COF as the sliding progresses (after 2900 m). Finally, on the Ni-Gr coated surface the wear (after 2000 m of sliding) leads to the exfoliation of graphene from the coating allowing the nanosized particles to enter the asperity contact, thus reduces asperity variations. The low surface energy of Gr enables Ni-Gr coating to have minimal adhesive friction, which is a resultant of the low polar surface energy for the coating. Further, Gr is a solid lubricant that helps easy shearing and reduces COF drastically. Additionally, the low surface energy of the of Ni-Gr coating aids in reducing the adhesion of Gr at the asperity interfaces which provides for a low and consistent COF during sliding.

The wear depth observed after the reciprocating sliding tests on each surface is shown in *Figure 9.6*. The figure shows the 2D cross-section profile and 3D wear track profile after sliding a distance of 4200 m. In the present tribo-system, the wear coefficient of 1045 steel surface is 3.31×10^{-10}, Ni coating is 2.95×10^{-11}, Ni-Gr coating is 1.51×10^{-11}, and the SiN counter body is 1.93×10^{-13}. The profile of 1045 steel shown in *Figure 9.6*a indicates a wear depth of 0.36 µm with pits and embedded wear particles along the wear track. In order to further investigate the wear particle size generated during sliding on each substrate surface, the wear tracks were observed under a Scanning Electron Microscope (SEM). The SEM images of the wear particles along the wear track can be observed in *Figure 9.7*a-c. The generation of large micron-sized wear particles (*Figure 9.7*a) during sliding causes entrapment of the particles at the asperity interface, which either leads to pitting or embedding of the particle on the surface during repeated sliding. Since, steel exhibits moderately high surface energy with similar contact angles for distilled water and 3.5% NaCl, hence it can be expected to be susceptible to corrosion and tribocorrosion [23, 94].

The wear profiles on Ni and Ni-Gr coatings are shown in *Figure 9.6*b and *Figure 9.6*c, respectively. The Ni coating exhibited a wear depth of ~ 0.16 µm with large built-up edges along the wear track (*Figure 9.6*b). The build-up edges during wear on Ni coating is mainly due to the high polar surface energy of Ni. The high polar surface energy causes the adhesion of submicron-sized wear particles (*Figure 9.7*b) that leads to the formation of buildup edges over the length of sliding. The Ni-Gr coating, on the other hand, exhibits a wear track of depth < 0.1 µm and a width which is nearly 25% less than the 1045 steel or Ni coating. The wear debris along the wear track of Ni-Gr surface was much smaller than those found on the Ni surface (*Figure 9.7*c). It is clear

from the SEM images that 1045 steel substrate without any coating generates large micron-sized particles while the Ni-coat generates sub-micron sized wear particles. The Ni-Gr-coat exhibits minimal wear while generating of sub-micron to nano-sized wear particles [241]. There was no particle adhesion found on the counter body (SiN ball) as can be observed in *Figure 9.7*a-c (ball tip).
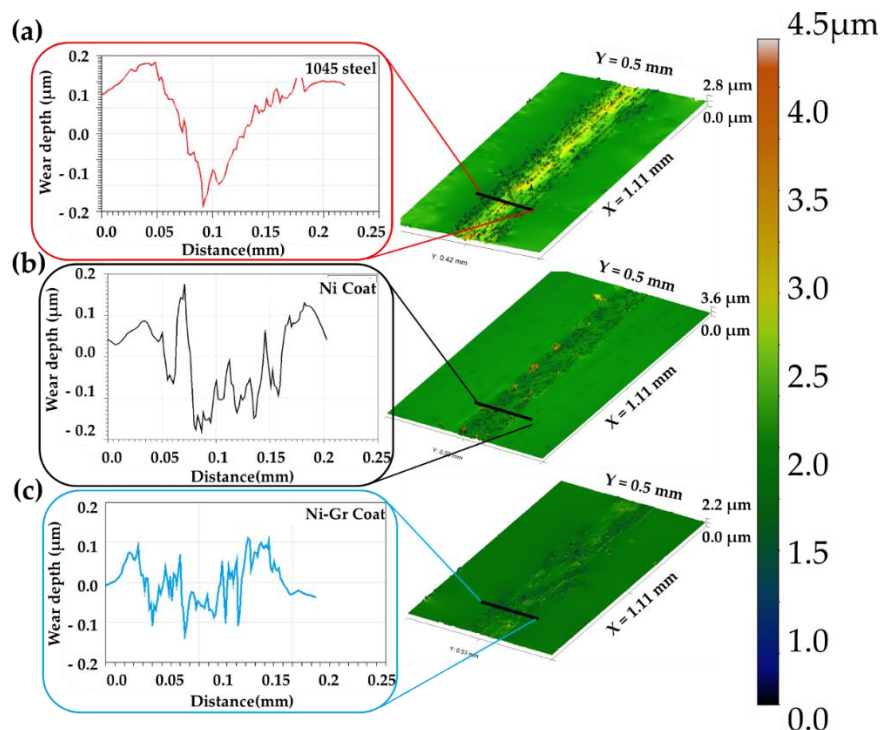
Figure 9.6: Wear depth and wear track profiles of (a) 1045 steel, (b) Ni Coating, (c) Ni-Gr coating.

Observing the wear profiles and wear particles generated during sliding on the Ni and Ni-Gr coating, it is evident that the addition of Gr to Ni matrix can reduce the wear while providing low friction. This behavior can be attributed to the low surface energy of Ni-Gr surface, which reduces the adhesive forces between the wear particles and surface. The reduced adhesive forces result in a reduction in wear particle size and its agglomeration as can be observed in *Figure 9.7*c. When the dispersion of a liquid or solid lubricant (such as Gr particle) occurs during sliding on a surface, it is restrained by weak London interactions which are enough to provide the lubrication effect. The generation of small sub-micron to nano-sized wear particles are a resultant of the low adhesive forces which prevent embedding of wear particles at the tribo-interface during sliding. Hence, as the Gr exfoliates during sliding provides a well-lubricated tribo-interface without any agglomeration of particles or built-up edges.
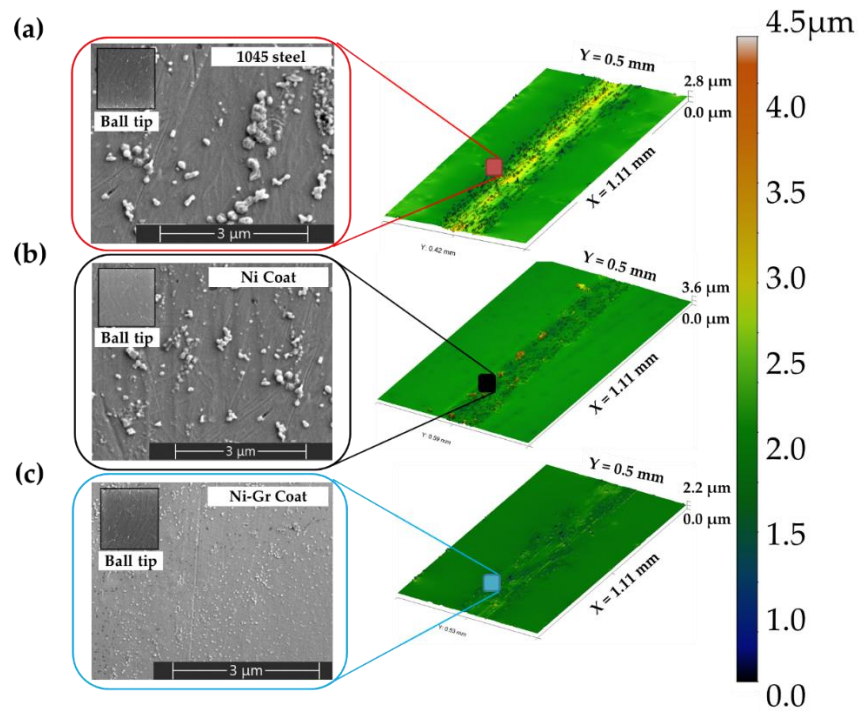
Figure 9.7: SEM images of the wear particles around the wear track of (a) 1045 steel, (b) Ni Coating, (c) Ni-Gr coating.

9.2.6. *Wear Mechanisms*

To better understand the wear mechanisms that led to the observed wear profiles and wear debris, a phenomenological model describing the generation of wear debris and their interaction at the tribo-interface is shown in *Figure 9.8*. It can be observed in *Figure 9.8*a that sliding between the counter material and 1045 steel surface generated micron-sized wear particles through two-body abrasion mechanism. These wear particles get trapped at the tribo-interface during sliding leading to three-body abrasive wear particle that further generated micron-sized irregular shaped wear debris. Such three-body wear debris tended to increase the abrading effect further, leading to deep wear tracks. Additionally, the high surface energy of the steel surface could increase the interaction of these wear particles at the tribo-interface.

When the steel surface is coated with either Ni coating or Ni–Gr composite coating the surface energy interactions between the counter body and the coated surface changes, leading to unique wear mechanisms. *Figure 9.8*b describes the wear mechanism when sliding occurs between the counter body and Ni-coated steel surface. As sliding progresses the two-body abrasion generated sub-micron spherical wear particles, which were small enough to enter the asperity valleys. Though the overall surface energy of the Ni coating was higher than the 1045 steel surface, the

dispersive surface energy of the Ni coating was lower. The low dispersive surface energy reduced the adhesive nature of the Ni wear particles. This physical nature of the wear particles in combination with the surface energy properties of the Ni coating led to reduced friction and abrasion at the tribo-interface. When sliding occurred between the counter body and Ni–Gr coated surface, the wear mechanism was similar to that observed for the Ni coating. In addition, there was also Gr exfoliation from the coating during sliding (*Figure 9.8*c). The structure of the graphene helped to easy shearing and further reduced the frictional force, wear rate, and debris formation. Hence, even a low concentration of Gr in the composite coating could enhance the tribological behavior of the surface.
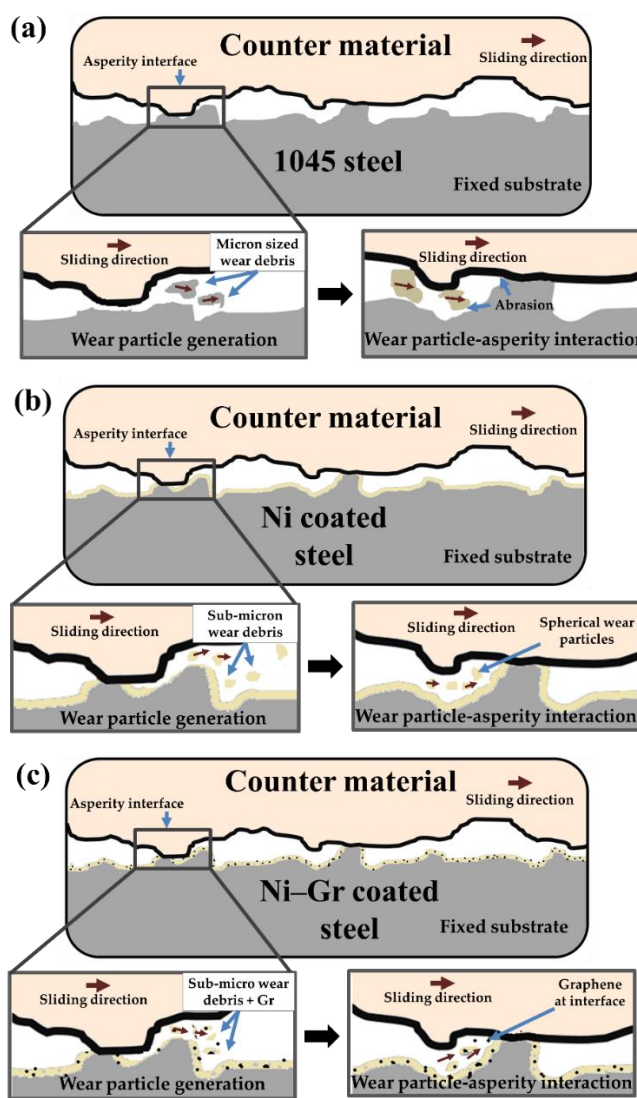
Figure 9.8: Wear mechanism model during sliding of silicon nitride counter body against (a) 1045 steel, (b) Ni coated, and (c) Ni–Gr coated surfaces.

9.2.7. *Evolution of wear rate without corrosion*

The wear rates (K_V) without corrosion for both Ni/GPL and steel 1020 were observed only in uncontaminated oil medium. *Figure 9.9* shows the increasing trends of wear rates of Ni/GPL and steel with increasing time and Archard loading factor W. Where, Archard factor (also known as the total dissipated energy during wear cycles) is defined as the multiplication of normal force (P) with total sliding displacement (δ) i.e. P (N) x δ (m). Therefore, the accumulated Archard factor ($\sum W$) is written as [224]:

$$\sum W = \sum_{i=1}^{N} W_{(i)}(Nm)\,;\ where\ W_{(i)} = 4\delta g_{(i)} P_{(i)}(Nm)$$

where $W_{(i)}$ denotes the dissipated Archard factor at *i*th wear cycle. The corresponding number of wear cycles (*i*) in *Figure 9.9* indicate that wear began beyond 8k cycles for both Ni/GPL and steel in salt and water contaminated oil. After 8k cycles, the wear rates of the both materials for remaining cycles were observed to be increasing steadily with time but as obvious, during this period the wear rate of steel was quite high compared to Ni/GPL. *Figure 9.9* also shows linearly rising trends of wear volumes (V) for Ni/GPL and steel. Wear volume is measured from wear rate (K_V) and accumulated Archard factor ($\sum W$) by using a conventional Archard description as:

$$\Delta V = K_v \times \Delta(\sum W) \quad (\mu m)^3$$

Table 9.4 plots the evolution of normalized 'wear profiles' and normalized 'wear depth kinetics profiles' at various stages of wear degradation for Ni/GPL and steel. The wear profiles showed the "U-shaped" behavior having a maximum wear depth always at the center (x = 0). It can be seen that at i = 10,000th cycle, Ni/GPL showed the normalized wear depth = 0.19 while steel showed considerably high normalized wear depth = 0.33. The wear profiles are the moving averages of measured surface interferometric values at various cycles. One such schematic example of interferometric wear profile is shown in red at i = 10,000 for Ni/GPL. The 3-D interferometric image for Ni/GPL and steel at i = 10,000th cycle in *Table 9.4*, clearly indicates that Ni/GPL exhibited less severe micro-plowing wear deformation compared to severe micro-cutting in steel. *Table 9.4* also displays the computed wear depth kinetics $h_{(i)}(x)$ for Ni/ GPL and steel at different wear cycles computed by using corresponding wear profiles. The following incremental equation was used for the development of wear depth kinetics profiles (where Δi is a single wear cycle):

$$h_{(i)}(x) \approx \frac{\Delta h}{\Delta i} = \frac{h_{(i)}(x) - h_{(i-\Delta i)}(x)}{\Delta i}$$

Evolution of Wear rate without Corrosion
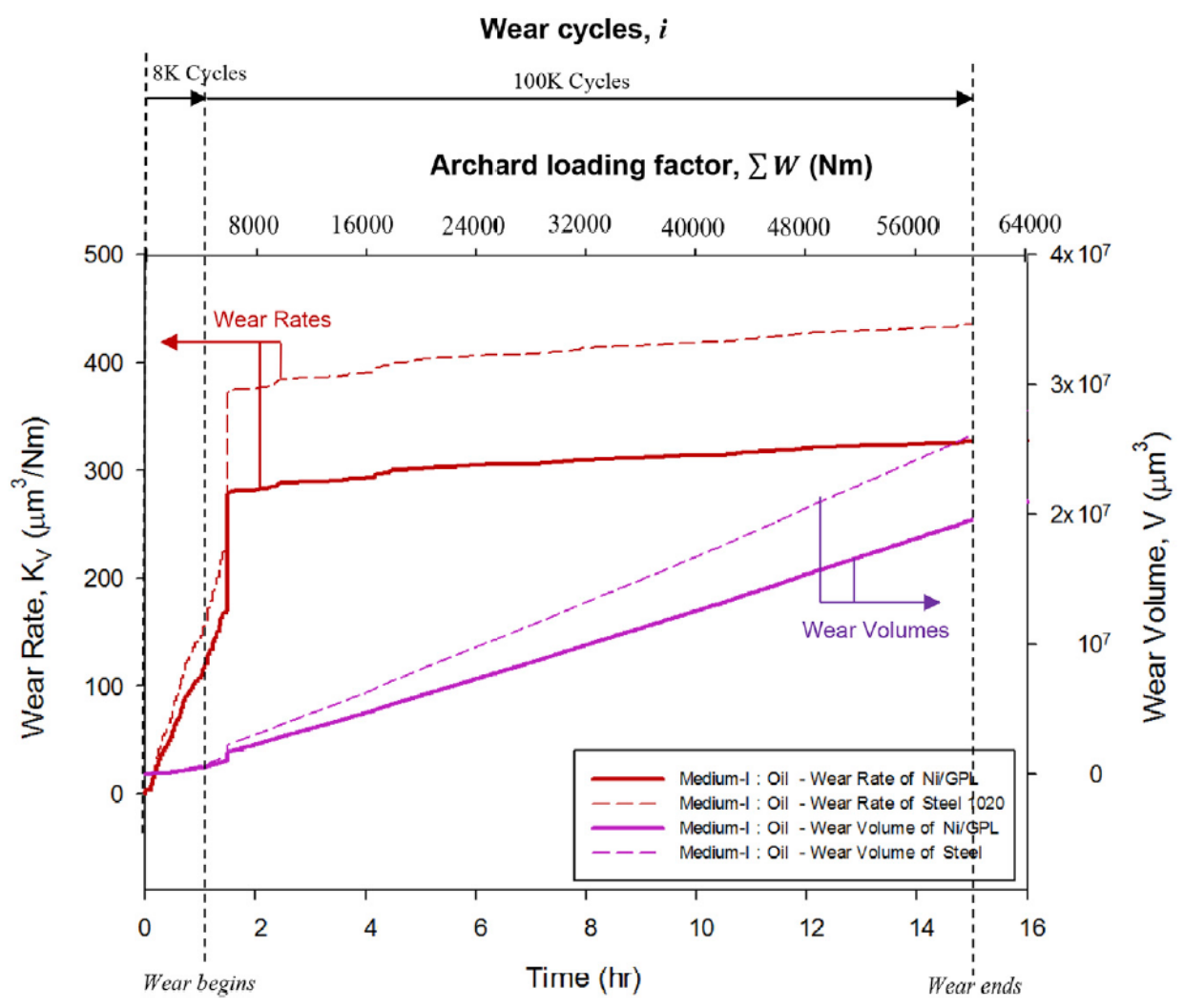
Figure 9.9: The evolution of wear rates KV without corrosion for both Ni/GPL and steel 1020 under uncontaminated oil lubrication condition.

A major decrease of the normalized wear depth kinetics profile corresponding to increasing cycles is observed. For example, at $i = 8000^{th}$ cycle, the normalized wear depth kinetics for Ni/GPL was 0.21 compared to steel (0.08). One more interesting thing is the evolution behavior of the normalized wear depth kinetics profile initiating with the elliptical shape decreasing to the Hertzian shape and finally becoming a quasi-flat shaped. The contact extremities in quasi-flat distribution ($i = 8000^{th}$ cycle and onwards) exhibit the type of wear deformation, for example, micro-plowing

in Ni/GPL showing slightly heightened contact edges while micro-cutting in steel is showing almost full flat distribution.

Table 9.4: The wear depth profiles at different ith wear cycles of Ni/GPL and steel in addition to a 3-D interferometric image indicating the type of wear delamination. The Table also shows the computed wear depth kinetics profiles corresponding to wear profiles at different ith wear cycles of Ni/GPL

Material	Wear depth profiles, Interferometric image and wear depth kinetics profiles
Ni/GPL	

Material	Wear depth profiles, Interferometric image and wear depth kinetics profiles
Steel 1020	 **Wear depth profiles** **3-D Interferometric image** –Micro-cutting **Wear depth kinetics profiles**
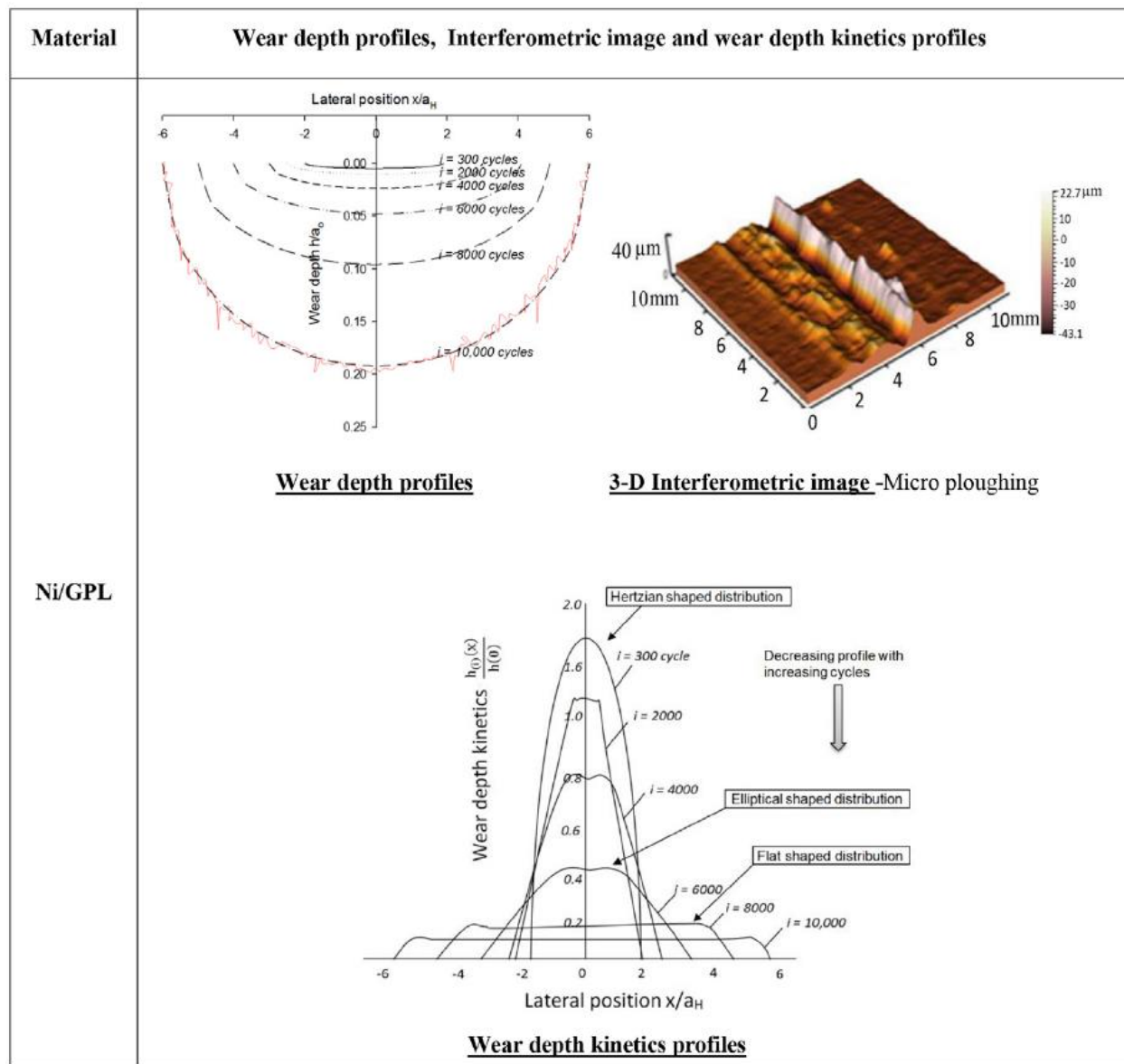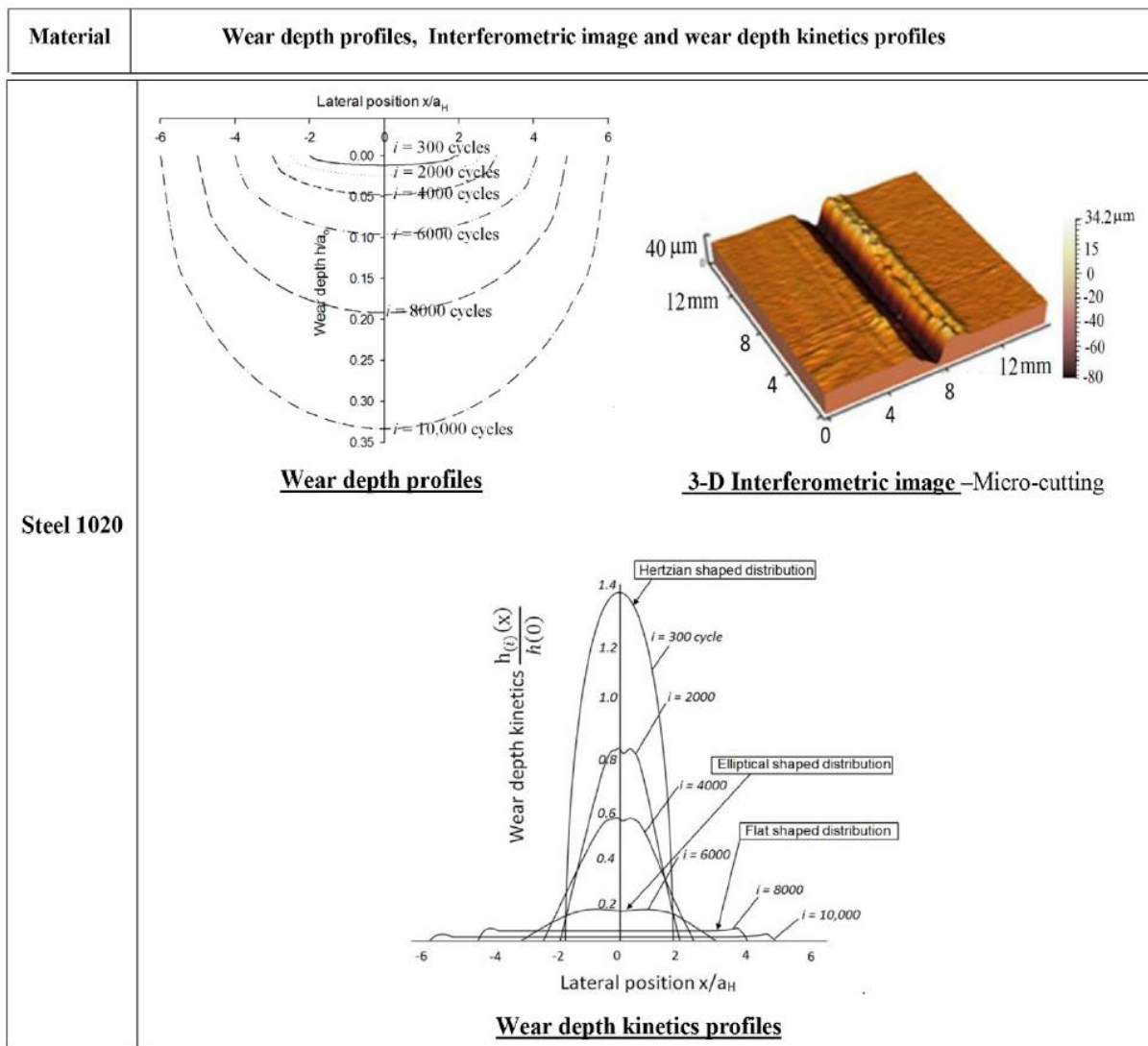
9.3. Conclusions

The following conclusions could be drawn from the present study:

- The surface roughness and profile data indicated an excellent finish of electrodeposit coatings with a surface roughness that corresponded to the substrate surface.
- Ni–Gr coating had overall surface energy, which was about 82.84% less than the Ni coating, while 75.6% less than the steel substrate.
- The presence of graphene was found to decrease the polar component of surface energy significantly than the dispersive component.

- Fluids with high dispersion surface energy could wet the Ni–Gr coating, but the adhesion energy between the fluid and the surface could be low.

- The addition of Gr to Ni matrix was found to reduce the wear while providing low friction.

- The COF increased for 1045 steel (18% increase) and the Ni coated surface (12% increase), while it decreased by 11% for the Ni–Gr coating.

- Wear on Ni–Gr coated surface led to the exfoliation of graphene from the coating allowing the nanosized particles to enter the asperity contact and reduce the COF.

- The low surface energy of Ni–Gr coating was found to decrease the adhesive forces between the wear particles and surface.

Chapter 10: Conclusions

The research conducted in this dissertation aims to present a further understanding of the effect of various surface modification techniques on the tribocorrosion behavior of steel and magnesium alloy surfaces. The first step was designing an *in-situ* tribocorrosion monitoring system for various surface, lubricant, environmental, and tribo-interface conditions. The studies then focused on understanding the mechanism of tribocorrosion and designing surfaces with improved tribocorrosion resistance. Surface engineering and functionalization methods, including LSP on steel and magnesium alloys, and nanocomposite coatings using nickel-graphene on tribocorrsion were then investigated. The environmental conditions included aqueous environments that simulated seawater conditions. The studies resulted in an understanding of the correlation between surface roughness, surface energy, wear, corrosion, and wear-corrosion synergy in defining various tribocorrosion mechanisms. The conclusions that resulted from the research are discussed in this section.

The limitations of oil-based monitoring systems were overcome by designing a stable system to measure the effects of core surface degradations. It was found during testing that the kinetic nature of the oil medium causes moderate fluctuations in the potential measurements which can be compensated by strategically aligning the reference and counter electrodes with the wear track and fluid flow. The test-rig design proves to be an effective method of monitoring wear and corrosion synergism in the oil medium. This system was used to investigate tribocorrosion behavior of LSP processed surfaces and nanocomposite coatings. These engineered surfaces were investigated for their tribocorrosion mechanisms and how effective these advanced manufacturing techniques are able to mitigate the effects of tribocorrosion.

LSP was found to enhance the surface and tribological properties and mitigate the effects of corrosion and tribocorrosion. The gradient of restructuring the asperities at various laser intensities was attributed to the magnitude of laser shock loading during LSP. The 3D surface roughness parameter*: average surface roughness, skewness, and kurtosis* were found to be the best indicator of the surface roughening effects resulting from the tribocorrosion of LSP processed surfaces. Surface treated at low laser intensity experienced the least change (9.0%) in surface roughness after tribocorrosion and the untreated surface experienced the highest change in surface roughness at 31.9%. Surfaces treated at low laser intensities showed the lowest increase in *corrosion potential* with lowest wear volume and friction during sliding. During tribocorrosion, the surface

strengthening effect of LSP had a dominating influence on wear at low laser intensities, whereas the surface roughening effect of LSP had a dominating influence on wear at higher laser intensities. Low laser intensity seems to favor better tribocorrosion resistance. The rate of surface degradation on LSP processed area due to tribocorrosion was found to depend on the interfacial surface energy of solid with the aqueous environment. The interfacial surface energy of solid influences the rates of corrosion under tribocorrosion environments. The change in surface roughness and liquid adhesion (wettability) due to LSP modifies the solid-liquid interfacial surface energy. The change in the interfacial surface energy is found to be a function of the applied laser intensity. A negligible change in the roughness factor was observed after tribocorrosion on low laser intensity treated surfaces, which showed the resilience of LSP to tribocorrosion.

The presence of graphene in nickel-graphene nanocomposite coatings was found to decrease the polar component of surface energy significantly more than the dispersive component. The addition of graphene to the nickel matrix was found to reduce the wear while providing low friction. The nanocomposite coating was found to have the lowest surface energy. Due to the low surface energy of nanocomposite coating a decrease in the adhesive forces between the wear particles and surface was observed. The optimized nano particle concentration in the coating proved to be an effective engineering technique to mitigate tribocorrosion.

Journal publications

Cited by (06/30/2020)	All	Since 2015
Citations	151	151
h-index	8	8
i10-index	8	8

1. **Siddaiah, A.**, Menezes, P.L., **2016**. Advances in Bio-inspired Tribology for Engineering Applications. Journal of Bio- and Tribo-Corrosion 2(4), 1-19.
2. **Siddaiah, A.**, Khan, A.Z., Ramachandran, R., Menezes, L.P., **2017**. Performance Analysis of Retrofitted Tribo-Corrosion Test Rig for Monitoring In Situ Oil Conditions. Materials 10(10).
3. **Siddaiah, A.**, Singh, B.K., Mastanaiah, P., **2017**. Prediction and optimization of weld bead geometry for electron beam welding of AISI 304 stainless steel. The International Journal of Advanced Manufacturing Technology 89(1), 27-43.
4. Reeves, C.J., **Siddaiah, A.**, Menezes, P.L., **2017**. A Review on the Science and Technology of Natural and Synthetic Biolubricants. Journal of Bio- and Tribo-Corrosion 3(1), 11.
5. Reeves, C.J., **Siddaiah, A.**, Menezes, P.L., **2017**. Ionic Liquids: A Plausible Future of Bio-lubricants. Journal of Bio- and Tribo-Corrosion 3(2), 18.
6. Reeves, C.J., **Siddaiah, A.**, Menezes, P.L., **2017**. Friction and wear behavior of environmentally friendly ionic liquids for sustainability of biolubricants, Journal of Tribology 141 (5), 051604, 1-11.
7. **Siddaiah, A.,** Mao, B., Menezes, P.L., Liao, Y., **2018**. Surface characterization and tribological performance of laser shock peened steel surfaces, Surface and Coatings Technology 351, 188-197.
8. Mao, B., **Siddaiah, A.,** Menezes, P.L., Liao, Y., **2018**. Surface texturing by indirect laser shock surface patterning for manipulated friction coefficient, Journal of Materials Processing Technology 257, 227-233.
9. Nazir, M. H., Khan, A.Z., Saeed, A., **Siddaiah, A.**, Menezes, P.L., **2018**. Synergistic wear-corrosion analysis and modelling of nanocomposite coatings, Tribology International, Volume 121, 30-44.
10. Reeves, C.J., **Siddaiah, A.**, Menezes, P.L., **2018**. Tribological study of imidazolium and phosphonium ionic liquid-based lubricants as additives in carboxylic acid-based natural oil: Advancements in environmentally friendly lubricants. Journal of Cleaner Production 176, 241-250.
11. **Siddaiah, A.**, Kumar, P., Henderson, A., Misra, M., Menezes, P.L., **2019**. Surface Energy and Tribology of Electrodeposited Ni and Ni–Graphene Coatings on Steel, Lubricants, 7, https://doi.org/10.3390/lubricants7100087.
12. Zhang, X., Mao, B., **Siddaiah, A.,** Menezes, P.L., Liao, Y., **2019**. Direct Laser Shock Surface Patterning of an AZ31B Magnesium Alloy: Microstructure Evolution and Friction Performance, Journal of Materials Processing Technology, Volume 275, 116333.
13. **Siddaiah, A.**, Kasar, A.K., Manoj, A., Menezes, P.L., **2019**. In-Situ Fretting Wear Analysis of Electrical Connectors for Real System Applications, Journal of Manufacturing and Materials Processing 3 (2), 47, 1-12.

14. Kasar, A.K., **Siddaiah, A.**, Ramachandran, R., Menezes, P.L., **2019**. Tribocorrosion Performance of Tool Steel for Rock Drilling Process, Journal of Bio-and Tribo-Corrosion 5 (2), 44, 1-8.

15. Mao, B., **Siddaiah, A.,** Zhang, X., Menezes, P.L., Liao, Y., **2019**. The influence of surface pre-twinning on the friction and wear performance of an AZ31B Mg alloy, Applied Surface Science, Volume 480, 998-1007.

16. **Siddaiah, A.**, Kasar, A.K., Manoj, A., Menezes, P.L., **2019**. Influence of environmentally friendly multiphase lubricants on the friction and transfer layer formation during sliding against textured surfaces, Journal of Cleaner Production 209, 1245-1251.

17. **Siddaiah**, A., Mao, B., Liao, Y., & Menezes, P. L. **2020**. Effect of Laser Shock Peening on the Wear–Corrosion Synergistic Behavior of an AZ31B Magnesium Alloy. Journal of Tribology, 142(4).

18. Mao, B., **Siddaiah**, A., Liao, Y., & Menezes, P. L. **2020**. Laser surface texturing and related techniques for enhancing tribological performance of engineering materials: A review. Journal of Manufacturing Processes, 53, 153-173.

19. **Siddaiah**, A., Mao, B., Kasar, K.A., Liao, Y., & Menezes, P. L. **2020**. Influence of laser shock peening on the surface energy and tribocorrosion properties of an AZ31B Mg alloy. Wear, Under review.

20. Sikdar, S., **Siddaiah**, A., & Menezes, P. L. **2020**. Conversion of waste plastic to oils for tribological applications. Lubricants, Under review.

Conference publications

1. **Siddaiah, A.**, Kasar, A.K., Menezes, P.L., **2018**, Investigation and Fabrication of Multi-Functional Nanoparticle Surface Coatings for Wear-Corrosion Synergistic Resistance, 73rd STLE Annual Meeting and Exhibition, May 20th-24th, Minneapolis, Minnesota, USA.
2. Menezes, P.L., **Siddaiah, A.**, Kasar, A.K., **2018**, Influence of Machining Angle and Solid Lubricants in a Bio-Lubricant Medium, 73rd STLE Annual Meeting and Exhibition, May 20th-24th, Minneapolis, Minnesota, USA.
3. Kasar, A.K., **Siddaiah, A.**, Menezes, P.L., **2018**, Development of Alumina-Based Self-Lubricating Materials for High-Temperature Application, 73rd STLE Annual Meeting and Exhibition, May 20th-24th, Minneapolis, Minnesota, USA.
4. **Siddaiah, A.,** Kumar, P., Misra, M., Menezes, P. L., **2019**, Effect of Tribocorrosion on the Bond Strength of Electrodeposited Ni-graphene Composite Surface Coatings on AZ31B Mg Alloy, Technical Meeting and Exhibition at Materials Science & Technology Conference - 2019, Sep. 29th – Oct 4th, Portland, Oregon, USA.
5. **Siddaiah, A.,** Kumar, P., Du. J., Menezes, P. L., Misra, M., **2019**, Wear-corrosion Synergism Behavior of Molybdenum-Rhenium-Tellurium Alloys for Structural Application in Molten Salt Reactor, Technical Meeting and Exhibition at Materials Science & Technology Conference - 2019, Sep. 29th – Oct 4th, Portland, Oregon, USA.
6. **Siddaiah, A.,** Kumar, P., Akram. J., Menezes, P. L., Misra, M., **2019**, Tribocorroison Behavior of Inconel 718 Fabricated by Laser Powder Bed Fusion Based Additive Manufacturing, Technical Meeting and Exhibition at Materials Science & Technology Conference - 2019, Sep. 29th – Oct 4th, Portland, Oregon, USA.
7. Mao, B., **Siddaiah, A.,** Zhang, X., Li, B., Menezes, P. L., Liao, Y., **2019**, Improving the Tribological Performance of Magnesium Alloys by Laser Shock Peening, Technical Meeting and Exhibition at Materials Science & Technology Conference - 2019, Sep. 29th – Oct 4th, Portland, Oregon, USA.
8. Kumar, P., **Siddaiah, A.,** Kasar, A.K., Akram. J., Menezes, P. L., Misra, M., **2019**, Wear-corrosion Synergism Behavior of Additive Manufactured Ti-6Al-4V Alloy, Technical Meeting and Exhibition at Materials Science & Technology Conference - 2019, Sep. 29th – Oct 4th, Portland, Oregon, USA.
9. Kumar, P., Vadlamani, B., **Siddaiah, A.,** Kalvala, P., Menezes, P. L., Daroonparvar, R., Kay, C., Misra, M., **2019**, Microstructure Evaluation and Corrosion Behavior of Cold Spray Deposited Tantalum Coating, Technical Meeting and Exhibition at Materials Science & Technology Conference - 2019, Sep. 29th – Oct 4th, Portland, Oregon, USA.

References

[1] Batchelor AW, Stachowiak GW. Predicting synergism between corrosion and abrasive wear. Wear. 1988;123:281-91.

[2] Iwabuchi A, Lee JW, Uchidate M. Synergistic effect of fretting wear and sliding wear of Co-alloy and Ti-alloy in Hanks' solution. Wear. 2007;263:492-500.

[3] Iwabuchi A, Tsukamoto T, Shimizu T, Yashiro H. The Mechanism of Corrosive Wear of an Austenitic Stainless Steel in an Aqueous Electrolyte Solution. Tribology Transactions. 1998;41:96-102.

[4] Kurre SK, Garg R, Pandey S. A review of biofuel generated contamination, engine oil degradation and engine wear. Biofuels. 2017;8:273-80.

[5] Manoj K, Parboti Shankar M, Nirendra Mohan M. Advancement and current status of wear debris analysis for machine condition monitoring: a review. Industrial Lubrication and Tribology. 2013;65:3-11.

[6] Sazzad BS, Fazal MA, Haseeb ASMA, Masjuki HH. Retardation of oxidation and material degradation in biodiesel: a review. RSC Advances. 2016;6:60244-63.

[7] Roberts A, Brooks R, Shipway P. Internal combustion engine cold-start efficiency: A review of the problem, causes and potential solutions. Energy Conversion and Management. 2014;82:327-50.

[8] Zhu X, Zhong C, Zhe J. Lubricating oil conditioning sensors for online machine health monitoring – A review. Tribology International. 2017;109:473-84.

[9] Zahid R, Hassan MBH, Varman M, Mufti RA, Kalam MA, Zulkifli NWBM, et al. A Review on Effects of Lubricant Formulations on Tribological Performance and Boundary Lubrication Mechanisms of Non-Doped DLC/DLC Contacts. Critical Reviews in Solid State and Materials Sciences. 2016:1-28.

[10] Singh P, Goel V, Chauhan SR. Impact of dual biofuel approach on engine oil dilution in CI engines. Fuel. 2017.

[11] Cipris D, Walsh AT. Lubricant oil monitoring system, sensor for monitoring lubricant oil quality and method of manufacturing sensor for monitoring lubricant oil quality. Google Patents; 1988.

[12] Zhu J, He D, Bechhoefer E. Survey of lubrication oil condition monitoring, diagnostics, and prognostics techniques and systems. Journal of Chemical Science and Technology. 2013;2:100-15.

[13] Flanagan IM, Jordan JR, Whittington HW. Wear-debris detection and analysis techniques for lubricant-based condition monitoring. Journal of Physics E: Scientific Instruments. 1988;21:1011.

[14] Fassel VA, Peterson CA, Abercrombie FN, Kniseley RN. Simultaneous determination of wear metals in lubricating oils by inductively-coupled plasma atomic emission spectrometry. Analytical Chemistry. 1976;48:516-9.

[15] Zhu X, Du L, Zhe J. A 3×3 wear debris sensor array for real time lubricant oil conditioning monitoring using synchronized sampling. Mechanical Systems and Signal Processing. 2017;83:296-304.

[16] Du L, Zhe J, Carletta J, Veillette R, Choy F. Real-time monitoring of wear debris in lubrication oil using a microfluidic inductive Coulter counting device. Microfluidics and Nanofluidics. 2010;9:1241-5.

[17] Du L, Zhu X, Han Y, Zhe J. High Throughput Wear Debris Detection in Lubricants Using a Resonance Frequency Division Multiplexed Sensor. Tribology Letters. 2013;51:453-60.

[18] Liu Y, Liu Z, Xie Y, Yao Z. Research on an on-line wear condition monitoring system for marine diesel engine. Tribology International. 2000;33:829-35.

[19] Ruqiang Y, Gao RX. Complexity as a measure for machine health evaluation. IEEE Transactions on Instrumentation and Measurement. 2004;53:1327-34.

[20] Nazir MH, Khan ZA. A review of theoretical analysis techniques for cracking and corrosive degradation of film-substrate systems. Engineering Failure Analysis. 2017;72:80-113.

[21] Nazir MH, Saeed A, Khan Z. A comprehensive predictive corrosion model incorporating varying environmental gas pollutants applied to wider steel applications. Materials Chemistry and Physics. 2017;193:19-34.

[22] Mattei L, Di Puccio F, Piccigallo B, Ciulli E. Lubrication and wear modelling of artificial hip joints: A review. Tribology International. 2011;44:532-49.

[23] Siddaiah A, Khan AZ, Ramachandran R, Menezes LP. Performance Analysis of Retrofitted Tribo-Corrosion Test Rig for Monitoring In Situ Oil Conditions. Materials. 2017;10.

[24] Madsen BW. Measurement of erosion-corrosion synergism with a slurry wear test apparatus. Wear. 1988;123:127-42.

[25] Watson SW, Friedersdorf FJ, Madsen BW, Cramer SD. Methods of measuring wear-corrosion synergism. Wear. 1995;181-183:476-84.

[26] Landolt D, Mischler S, Stemp M. Electrochemical methods in tribocorrosion: a critical appraisal. Electrochimica Acta. 2001;46:3913-29.

[27] Wood RJK, Sun D, Thakare MR, de Frutos Rozas A, Wharton JA. Interpretation of electrochemical measurements made during micro-scale abrasion-corrosion. Tribology International. 2010;43:1218-27.

[28] García I, Drees D, Celis JP. Corrosion-wear of passivating materials in sliding contacts based on a concept of active wear track area. Wear. 2001;249:452-60.

[29] Vieira AC, Rocha LA, Papageorgiou N, Mischler S. Mechanical and electrochemical deterioration mechanisms in the tribocorrosion of Al alloys in NaCl and in NaNO3 solutions. Corrosion Science. 2012;54:26-35.

[30] Bermúdez M-D, Jiménez A-E, Sanes J, Carrión F-J. Ionic Liquids as Advanced Lubricant Fluids. Molecules. 2009;14:2888.

[31] Parsaeian P, Ghanbarzadeh A, Wilson M, Van Eijk MCP, Nedelcu I, Dowson D, et al. An experimental and analytical study of the effect of water and its tribochemistry on the tribocorrosive wear of boundary lubricated systems with ZDDP-containing oil. Wear. 2016;358:23-31.

[32] Mathew MT, Runa MJ, Laurent M, Jacobs JJ, Rocha LA, Wimmer MA. Tribocorrosion behavior of CoCrMo alloy for hip prosthesis as a function of loads: A comparison between two testing systems. Wear. 2011;271:1210-9.

[33] Bratu F, Benea L, Celis J-P. Tribocorrosion behaviour of Ni–SiC composite coatings under lubricated conditions. Surface and Coatings Technology. 2007;201:6940-6.

[34] Stachowiak G, Batchelor AW. Engineering tribology. Fourth ed. Kidlington, Oxford, United Kingdom: Butterworth-Heinemann; 2013. p. 11-49.

[35] Siddaiah A, Menezes PL. Advances in Bio-inspired Tribology for Engineering Applications. Journal of Bio- and Tribo-Corrosion. 2016;2:1-19.

[36] Fairand BP, Clauer AH. Laser generation of high-amplitude stress waves in materials. Journal of Applied Physics. 1979;50:1497-502.

[37] Clauer AH, Fairand BP. Interaction of laser-induced stress waves with metals. In: Metzbower E, editor. Applications of Lasers in Materials Processing. Washington, DC, USA: ASM International, Materials Park, OH, 229; 1979.

[38] Ahmad B, Fitzpatrick ME. The effect of laser shock peening on hardness and microstructure in a welded marine steel. The Journal of Engineering: Institution of Engineering and Technology; 2015.

[39] Peyre P, Fabbro R. Laser shock processing: a review of the physics and applications. Optical and Quantum Electronics. 1995;27:1213-29.

[40] Siddaiah A, Mao B, Liao Y, Menezes PL. Surface characterization and tribological performance of laser shock peened steel surfaces. Surface and Coatings Technology. 2018;351:188-97.

[41] Bobzin K, Bartels T. Industrial tribology: Tribosystems, friction, wear and surface engineering, lubrication. John Wiley & Sons; 2011. p. 429.

[42] Fairand BP, Wilcox BA, Gallagher WJ, Williams DN. Laser shock-induced microstructural and mechanical property changes in 7075 aluminum. Journal of Applied Physics. 1972;43:3893-5.

[43] Clauer A, Fairand B, Wilcox B. Pulsed laser induced deformation in an Fe-3 Wt Pct Si alloy. Metallurgical Transactions A. 1977;8:119-25.

[44] Clauer AH, Fairand BP, Wilcox BA. Laser shock hardening of weld zones in aluminum alloys. Metallurgical Transactions A. 1977;8:1871-6.

[45] Montross CS, Wei T, Ye L, Clark G, Mai Y-W. Laser shock processing and its effects on microstructure and properties of metal alloys: a review. International Journal of Fatigue. 2002;24:1021-36.

[46] Peyre P, Fabbro R, Merrien P, Lieurade HP. Laser shock processing of aluminium alloys. Application to high cycle fatigue behaviour. Materials Science and Engineering: A. 1996;210:102-13.

[47] Yakimets I, Richard C, Béranger G, Peyre P. Laser peening processing effect on mechanical and tribological properties of rolling steel 100Cr6. Wear. 2004;256:311-20.

[48] Zhang R, Hou X, Zhou X, Gao H, Mankoci S, Qin H, et al. Effects of Laser Shock Peening on the Wear and Degradation Behaviors of Magnesium Alloys. 2016:V002T01A5.

[49] Ding K, Ye L. Laser shock peening. In: Publishing W, editor. Laser shock peening: Performance and process simulation. CRC Press LLC, 6000 Broken Sound Parkway, NW, Suite 300, Boca Raton, Florida 33487, USA.: Woodhead Publishing Limited and CRC Press LLC; 2006. p. 7-43.

[50] Gujba KA, Medraj M. Laser Peening Process and Its Impact on Materials Properties in Comparison with Shot Peening and Ultrasonic Impact Peening. Materials. 2014;7.

[51] Shukla P, Nath S, Wang G, Shen X, Lawrence J. Surface property modifications of silicon carbide ceramic following laser shock peening. Journal of the European Ceramic Society. 2017;37:3027-38.

[52] Lu JZ, Wu LJ, Sun GF, Luo KY, Zhang YK, Cai J, et al. Microstructural response and grain refinement mechanism of commercially pure titanium subjected to multiple laser shock peening impacts. Acta Materialia. 2017;127:252-66.

[53] Kulkarni A, Chettri S, Prabhakaran S, Kalainathan S. Effect of Laser Shock Peening Without Coating on Surface Morphology and Mechanical Properties of Nickel-200. Mechanics, Materials Science & Engineering MMSE Journal Open Access. 2017;9.

[54] Nalla RK, Altenberger I, Noster U, Liu GY, Scholtes B, Ritchie RO. On the influence of mechanical surface treatments—deep rolling and laser shock peening—on the fatigue behavior of Ti–6Al–4V at ambient and elevated temperatures. Materials Science and Engineering: A. 2003;355:216-30.

[55] Jost P. Economic impact of tribology. Proc Mechanical Failures Prevention Group. 1976:117-39.

[56] Camargo PHC, Satyanarayana KG, Wypych F. Nanocomposites: synthesis, structure, properties and new application opportunities. Materials Research. 2009;12:1-39.

[57] Srivastava M, William Grips VK, Rajam KS. Influence of SiC, Si3N4 and Al2O3 particles on the structure and properties of electrodeposited Ni. Materials Letters. 2008;62:3487-9.

[58] Thiemig D, Bund A, Talbot JB. Influence of hydrodynamics and pulse plating parameters on the electrocodeposition of nickel–alumina nanocomposite films. Electrochimica Acta. 2009;54:2491-8.

[59] Low CTJ, Wills RGA, Walsh FC. Electrodeposition of composite coatings containing nanoparticles in a metal deposit. Surface and Coatings Technology. 2006;201:371-83.

[60] Möller A, Hahn H. Synthesis and characterization of nanocrystalline Ni/ZrO2 composite coatings. Nanostructured Materials. 1999;12:259-62.

[61] Karimpoor AA, Erb U, Aust KT, Palumbo G. High strength nanocrystalline cobalt with high tensile ductility. Scripta Materialia. 2003;49:651-6.

[62] Gyftou P, Stroumbouli M, Pavlatou EA, Asimidis P, Spyrellis N. Tribological study of Ni matrix composite coatings containing nano and micro SiC particles. Electrochimica Acta. 2005;50:4544-50.

[63] Gül H, Kılıç F, Aslan S, Alp A, Akbulut H. Characteristics of electro-co-deposited Ni–Al2O3 nano-particle reinforced metal matrix composite (MMC) coatings. Wear. 2009;267:976-90.

[64] Sadeghinezhad E, Mehrali M, Saidur R, Mehrali M, Tahan Latibari S, Akhiani AR, et al. A comprehensive review on graphene nanofluids: Recent research, development and applications. Energy Conversion and Management. 2016;111:466-87.

[65] Rasheed AK, Khalid M, Rashmi W, Gupta TCSM, Chan A. Graphene based nanofluids and nanolubricants – Review of recent developments. Renewable and Sustainable Energy Reviews. 2016;63:346-62.

[66] Saurín N, Sanes J, Bermúdez M-D. New Graphene/Ionic Liquid Nanolubricants. Materials Today: Proceedings. 2016;3:S227-S32.

[67] Gusain R, Mungse HP, Kumar N, Ravindran TR, Pandian R, Sugimura H, et al. Covalently attached graphene-ionic liquid hybrid nanomaterials: synthesis, characterization and tribological application. Journal of Materials Chemistry A. 2016;4:926-37.

[68] Bandeira P, Monteiro J, Baptista AM, Magalhães FD. Influence of oxidized graphene nanoplatelets and [DMIM][NTf2] ionic liquid on the tribological performance of an epoxy-PTFE coating. Tribology International. 2016;97:478-89.

[69] Zhao J, He Y, Wang Y, Wang W, Yan L, Luo J. An investigation on the tribological properties of multilayer graphene and MoS2 nanosheets as additives used in hydraulic applications. Tribology International. 2016;97:14-20.

[70] Ramón-Raygoza ED, Rivera-Solorio CI, Giménez-Torres E, Maldonado-Cortés D, Cardenas-Alemán E, Cué-Sampedro R. Development of nanolubricant based on impregnated multilayer graphene for automotive applications: Analysis of tribological properties. Powder Technology. 2016;302:363-71.

[71] Blanco D, González R, Viesca JL, Fernández-González A, Bartolomé M, Battez AH. Antifriction and antiwear properties of an ionic liquid with fluorine-containing anion used as lubricant additive. Tribology Letters. 2017;65:66.

[72] Kumar CMP, Venkatesha TV, Shabadi R. Preparation and corrosion behavior of Ni and Ni–graphene composite coatings. Materials Research Bulletin. 2013;48:1477-83.

[73] Algul H, Tokur M, Ozcan S, Uysal M, Cetinkaya T, Akbulut H, et al. The effect of graphene content and sliding speed on the wear mechanism of nickel–graphene nanocomposites. Applied Surface Science. 2015;359:340-8.

[74] Berlia R, Punith Kumar MK, Srivastava C. Electrochemical behavior of Sn-graphene composite coating. RSC Advances. 2015;5:71413-8.

[75] Jiang K, Li J, Liu J. Electrochemical codeposition of graphene platelets and nickel for improved corrosion resistant properties. RSC Advances. 2014;4:36245-52.

[76] Lee S-K, Jang HY, Jang S, Choi E, Hong BH, Lee J, et al. All Graphene-Based Thin Film Transistors on Flexible Plastic Substrates. Nano Letters. 2012;12:3472-6.

[77] Rafiee MA, Lu W, Thomas AV, Zandiatashbar A, Rafiee J, Tour JM, et al. Graphene Nanoribbon Composites. ACS Nano. 2010;4:7415-20.

[78] Siddaiah A, Kasar AK, Manoj A, Menezes PL. Influence of environmental friendly multiphase lubricants on the friction and transfer layer formation during sliding against textured surfaces. Journal of Cleaner Production. 2019;209:1245-51.

[79] Omrani E, Menezes LP, Rohatgi KP. Effect of Micro- and Nano-Sized Carbonous Solid Lubricants as Oil Additives in Nanofluid on Tribological Properties. Lubricants. 2019;7.

[80] Siddaiah A, Kumar P, Henderson A, Misra M, Menezes LP. Surface Energy and Tribology of Electrodeposited Ni and Ni–Graphene Coatings on Steel. Lubricants. 2019;7.

[81] Kasar AK, Menezes PL. Synthesis and recent advances in tribological applications of graphene. The International Journal of Advanced Manufacturing Technology. 2018;97:3999-4019.

[82] Kasar AK, Xiong G, Menezes PL. Graphene-Reinforced Metal and Polymer Matrix Composites. JOM. 2018;70:829-36.

[83] Tabandeh-Khorshid M, Omrani E, Menezes PL, Rohatgi PK. Tribological performance of self-lubricating aluminum matrix nanocomposites: Role of graphene nanoplatelets. Engineering Science and Technology, an International Journal. 2016;19:463-9.

[84] Dorri Moghadam A, Omrani E, Menezes PL, Rohatgi PK. Mechanical and tribological properties of self-lubricating metal matrix nanocomposites reinforced by carbon nanotubes (CNTs) and graphene – A review. Composites Part B: Engineering. 2015;77:402-20.

[85] Bahrololoom ME, Sani R. The influence of pulse plating parameters on the hardness and wear resistance of nickel–alumina composite coatings. Surface and Coatings Technology. 2005;192:154-63.

[86] Chen L, Wang L, Zeng Z, Zhang J. Effect of surfactant on the electrodeposition and wear resistance of Ni–Al 2 O 3 composite coatings. Materials Science and Engineering: A. 2006;434:319-25.

[87] Lajevardi SA, Shahrabi T. Effects of pulse electrodeposition parameters on the properties of Ni–TiO 2 nanocomposite coatings. Applied Surface Science. 2010;256:6775-81.

[88] Li J, An Z, Wang Z, Toda M, Ono T. Pulse-reverse electrodeposition and micromachining of graphene–nickel composite: an efficient strategy toward high-performance microsystem application. ACS applied materials & interfaces. 2016;8:3969-76.

[89] Yaghoubinezhad Y, Afshar A. Design of Experiments for Pulse Reverse Electrodeposition of Graphene Oxide toward Hydrogen Evolution Reaction. ECS Journal of Solid State Science and Technology. 2015;4:M7-M17.

[90] Ren Z, Meng N, Shehzad K, Xu Y, Qu S, Yu B, et al. Mechanical properties of nickel-graphene composites synthesized by electrochemical deposition. Nanotechnology. 2015;26:065706.

[91] Szeptycka B, Gajewska-Midzialek A, Babul T. Electrodeposition and corrosion resistance of Ni-graphene composite coatings. Journal of Materials Engineering and Performance. 2016;25:3134-8.

[92] Bajwa RS, Khan Z, Bakolas V, Braun W. Water-lubricated Ni-based composite (Ni–Al2O3, Ni–SiC and Ni–ZrO2) thin film coatings for industrial applications. Acta Metallurgica Sinica (English Letters). 2016;29:8-16.

[93] Bajwa R, Khan Z, Nazir H, Chacko V, Saeed A. Wear and Friction Properties of Electrodeposited Ni-Based Coatings Subject to Nano-enhanced Lubricant and Composite Coating. Acta Metallurgica Sinica (English Letters). 2016;29:902-10.

[94] Nazir MH, Khan ZA, Saeed A, Siddaiah A, Menezes PL. Synergistic wear-corrosion analysis and modelling of nanocomposite coatings. Tribology International. 2018;121:30-44.

[95] Matsui M, Kakishima H. Improvement of tribological performance of steel by solid lubricant shot-peening in dry rolling/sliding contact wear tests. Wear. 2006;260:669-73.

[96] Adamović D, Babic M, Jeremic B. Shot peening, influence on tribological, characteristics of surfaces. ICSP-7, Warsaw, Poland. 1999:350-8.

[97] Amanov A, Penkov OV, Pyun Y-S, Kim D-E. Effects of ultrasonic nanocrystalline surface modification on the tribological properties of AZ91D magnesium alloy. Tribology International. 2012;54:106-13.

[98] Amanov A, Pyun Y-S, Sasaki S. Effects of ultrasonic nanocrystalline surface modification (UNSM) technique on the tribological behavior of sintered Cu-based alloy. Tribology International. 2014;72:187-97.

[99] Avril L, Courant B, Hantzpergue JJ. Tribological performance of α-Fe(Cr)-Fe2B-FeB and α-Fe(Cr)-h-BN coatings obtained by laser melting. Wear. 2006;260:351-60.

[100] Dutta Majumdar J, Galun R, Mordike BL, Manna I. Effect of laser surface melting on corrosion and wear resistance of a commercial magnesium alloy. Materials Science and Engineering: A. 2003;361:119-29.

[101] Totolin V, Rodríguez Ripoll M, Jech M, Podgornik B. Enhanced tribological performance of tungsten carbide functionalized surfaces via in-situ formation of low-friction tribofilms. Tribology International. 2016;94:269-78.

[102] Mao B, Siddaiah A, Menezes PL, Liao Y. Surface texturing by indirect laser shock surface patterning for manipulated friction coefficient. Journal of Materials Processing Technology. 2018;257:227-33.

[103] Wang F, Yao Z, Deng Q. Experimental study on laser shock processing of brass. Journal of University of Science and Technology Beijing, Mineral, Metallurgy, Material. 2007;14:529-32.

[104] Wang H, Ning C, Huang Y, Cao Z, Chen X, Zhang W. Improvement of abrasion resistance in artificial seawater and corrosion resistance in NaCl solution of 7075 aluminum alloy processed by laser shock peening. Optics and Lasers in Engineering. 2017;90:179-85.

[105] Lim H, Kim P, Jeong H, Jeong S. Enhancement of abrasion and corrosion resistance of duplex stainless steel by laser shock peening. Journal of Materials Processing Technology. 2012;212:1347-54.

[106] Petan L, Ocaña JL, Grum J. Effects of Laser Shock Peening on the Surface Integrity of 18 % Ni Maraging Steel. Strojniški vestnik - Journal of Mechanical Engineering; Vol 62, No 5 (2016): Strojniški vestnik - Journal of Mechanical EngineeringDO - 105545/sv-jme20153305. 2016.

[107] Petan L, Ocaña JL, Grum J. Influence of laser shock peening pulse density and spot size on the surface integrity of X2NiCoMo18-9-5 maraging steel. Surface and Coatings Technology. 2016;307, Part A:262-70.

[108] Ren XD, Zhou WF, Liu FF, Ren YP, Yuan SQ, Ren NF, et al. Microstructure evolution and grain refinement of Ti-6Al-4V alloy by laser shock processing. Applied Surface Science. 2016;363:44-9.

[109] Menezes PL, Kishore, Kailas SV. Effect of surface roughness parameters and surface texture on friction and transfer layer formation in tin–steel tribo-system. Journal of Materials Processing Technology. 2008;208:372-82.

[110] Menezes PL, Kishore, Kailas SV. Influence of roughness parameters and surface texture on friction during sliding of pure lead over 080 M40 steel. The International Journal of Advanced Manufacturing Technology. 2008;43:731-43.

[111] Menezes PL, Kishore, Kailas SV. Influence of roughness parameters on coefficient of friction under lubricated conditions. Sadhana. 2008;33:181-90.

[112] Menezes PL, Kishore, Kailas SV. Influence of surface texture and roughness parameters on friction and transfer layer formation during sliding of aluminium pin on steel plate. Wear. 2009;267:1534-49.

[113] Lundberg J. Influence of surface roughness on normal-sliding lubrication. Tribology international. 1995;28:317-22.

[114] Menezes PL, Kishore, Kailas SV. On the effect of surface texture on friction and transfer layer formation—A study using Al and steel pair. Wear. 2008;265:1655-69.

[115] Menezes PL, Kishore, Kailas SV. Studies on friction and transfer layer: role of surface texture. Tribology Letters. 2006;24:265-73.

[116] Menezes PL, Kishore, Kailas SV. Influence of surface texture on coefficient of friction and transfer layer formation during sliding of pure magnesium pin on 080 M40 (EN8) steel plate. Wear. 2006;261:578-91.

[117] Mao B, Siddaiah A, Zhang X, Li B, Menezes PL, Liao Y. The influence of surface pre-twinning on the friction and wear performance of an AZ31B Mg alloy. Applied Surface Science. 2019;480:998-1007.

[118] Ge M-Z, Xiang J-Y. Effect of laser shock peening on microstructure and fatigue crack growth rate of AZ31B magnesium alloy. Journal of Alloys and Compounds. 2016;680:544-52.

[119] Zhang R, Zhou X, Gao H, Mankoci S, Liu Y, Sang X, et al. The effects of laser shock peening on the mechanical properties and biomedical behavior of AZ31B magnesium alloy. Surface and Coatings Technology. 2018;339:48-56.

[120] Brady MP, Rother G, Anovitz LM, Littrell KC, Unocic KA, Elsentriecy HH, et al. Film Breakdown and Nano-Porous $Mg(OH)_2$ Formation from Corrosion of Magnesium Alloys in Salt Solutions. Journal of The Electrochemical Society. 2015;162:C140-C9.

[121] Mordike BL, Ebert T. Magnesium: Properties — applications — potential. Materials Science and Engineering: A. 2001;302:37-45.

[122] Ambat R, Aung NN, Zhou W. Studies on the influence of chloride ion and pH on the corrosion and electrochemical behaviour of AZ91D magnesium alloy. Journal of Applied Electrochemistry. 2000;30:865-74.

[123] Gao L, Zhang C, Zhang M, Huang X, Sheng N. The corrosion of a novel Mg–11Li–3Al–0.5RE alloy in alkaline NaCl solution. Journal of Alloys and Compounds. 2009;468:285-9.

[124] Wu TC, Ho YH, Joshi SS, Rajamure RS, Dahotre NB. Microstructure and corrosion behavior of laser surface-treated AZ31B Mg bio-implant material. Lasers in medical science. 2017;32:797-803.

[125] Danford MD, Mendrek MJ, Mitchell ML, Torres PD. The Corrosion Protection of Magnesium Alloy AZ31B. 1997.

[126] Azzi M, Klemberg-Sapieha J-E. Tribocorrosion test protocols for sliding contacts. Tribocorrosion of Passive Metals and Coatings: Elsevier; 2011. p. 222-38.

[127] Siddaiah A, Mao B, Liao Y, Menezes PL. Effect of laser shock peening on the wear-corrosion synergistic behavior of AZ31B magnesium alloys. Journal of Tribology. 2019:1-22.

[128] Ge M-Z, Xiang J-Y, Yang L, Wang JT. Effect of laser shock peening on the stress corrosion cracking of AZ31B magnesium alloy in a simulated body fluid. Surface and Coatings Technology. 2017;310:157-65.

[129] van Oss CJ, Chaudhury MK, Good RJ. Monopolar surfaces. Advances in colloid and interface science. 1987;28:35-64.

[130] Van Oss CJ, Chaudhury MK, Good RJ. Interfacial Lifshitz-van der Waals and polar interactions in macroscopic systems. Chemical Reviews. 1988;88:927-41.

[131] Wang H, Huang Y, Zhang W, Ostendorf A. Investigation of multiple laser shock peening on the mechanical property and corrosion resistance of shipbuilding 5083Al alloy under a simulated seawater environment. Appl Opt. 2018;57:6300-8.

[132] Dai F, Zhou J, Lu J, Luo X. A technique to decrease surface roughness in overlapping laser shock peening. Applied Surface Science. 2016;370:501-7.

[133] Ta VD, Dunn A, Wasley TJ, Li J, Kay RW, Stringer J, et al. Laser textured surface gradients. Applied Surface Science. 2016;371:583-9.

[134] Dai FZ, Zhang ZD, Zhou JZ, Lu JZ, Zhang YK. Analysis of surface roughness at overlapping laser shock peening. Surface Review and Letters. 2016;23:1650012.

[135] Ta DV, Dunn A, Wasley TJ, Kay RW, Stringer J, Smith PJ, et al. Nanosecond laser textured superhydrophobic metallic surfaces and their chemical sensing applications. Applied Surface Science. 2015;357, Part A:248-54.

[136] Ta VD, Dunn A, Wasley TJ, Li J, Kay RW, Stringer J, et al. Laser textured superhydrophobic surfaces and their applications for homogeneous spot deposition. Applied Surface Science. 2016;365:153-9.

[137] Ho Y-H, Vora HD, Dahotre NB. Laser surface modification of AZ31B Mg alloy for bio-wettability. Journal of Biomaterials Applications. 2014;29:915-28.

[138] Epperlein N, Menzel F, Schwibbert K, Koter R, Bonse J, Sameith J, et al. Influence of femtosecond laser produced nanostructures on biofilm growth on steel. Applied Surface Science $V 418. 2017:420-4.

[139] Singh A, Patel DS, Ramkumar J, Balani K. Single step laser surface texturing for enhancing contact angle and tribological properties. The International Journal of Advanced Manufacturing Technology. 2019;100:1253-67.

[140] Romoli L, Moroni F, Khan MMA. A study on the influence of surface laser texturing on the adhesive strength of bonded joints in aluminium alloys. CIRP Annals - Manufacturing Technology. 2017;66:237-40.

[141] Góral A, Lityńska-Dobrzyńska L, Kot M. Effect of Surface Roughness and Structure Features on Tribological Properties of Electrodeposited Nanocrystalline Ni and Ni/Al2O3 Coatings. Journal of Materials Engineering and Performance. 2017;26:2118-28.

[142] Allahyarzadeh MH, Aliofkhazraei M, Rezvanian AR, Torabinejad V, Sabour Rouhaghdam AR. Ni-W electrodeposited coatings: Characterization, properties and applications. Surface and Coatings Technology. 2016;307:978-1010.

[143] Ali E. Solid Lubricants and Self-Lubricating Films. Modern Tribology Handbook, Two Volume Set: CRC Press; 2000.

[144] Donnet C, Erdemir A. Historical developments and new trends in tribological and solid lubricant coatings. Surface and Coatings Technology. 2004;180–181:76-84.

[145] Omrani E, Rohatgi PK, Menezes PL. Tribology and Applications of Self-Lubricating Materials: CRC Press; 2017.

[146] Zhaodi Ren and Nan Meng and Khurram Shehzad and Yang Xu and Shaoxing Qu and Bin Yu and JKL. Mechanical properties of nickel-graphene composites synthesized by electrochemical deposition. Nanotechnology. 2015;26:065706.

[147] Wang C, Brown GO, Burris DL, Korley LTJ, Epps TH. Coating Architects: Manipulating Multiscale Structures To Optimize Interfacial Properties for Coating Applications. ACS Applied Polymer Materials. 2019.

[148] Jokari-Sheshdeh M, Mahboubi F, Dehghani K. Structure and tribological behavior of diamond-like carbon coatings deposited on the martensitic stainless steel: The influence of gas composition and temperature. Diamond and Related Materials. 2018;81:77-88.

[149] Tysoe WT. 17 Surface Chemistry at the Tribological Interface. Surfactants in Tribology. 2016;2:437.

[150] Emerson JA, Garabedian NT, Burris DL, Furst EM, Epps TH. Exploiting Feedstock Diversity To Tune the Chemical and Tribological Properties of Lignin-Inspired Polymer Coatings. ACS Sustainable Chemistry & Engineering. 2018;6:6856-66.

[151] Tripathi M, Awaja F, Paolicelli G, Bartali R, Iacob E, Valeri S, et al. Tribological characteristics of few-layer graphene over Ni grain and interface boundaries. Nanoscale. 2016;8:6646-58.

[152] Speight JG. Handbook of petroleum product analysis. Second ed. Hoboken, New Jersey, USA: John Wiley & Sons; 2015. p. 26-44.

[153] Sanjeev K, Manoj K. Assessing remaining useful life of lubricant using Fourier transform infrared spectroscopy. Journal of Quality in Maintenance Engineering. 2016;22:202-14.

[154] Zaharia CV, Niculescu R, Iorga V, Ducu C, Clenci A, Aron B. Diagnosing the Operation of a Locomotive Diesel Engine Based on the Analysis of Used Oil in the Period Between Two Technical Revisions. In: Chiru A, Ispas N, editors. CONAT 2016 International Congress of Automotive and Transport Engineering. Cham: Springer International Publishing; 2017. p. 319-27.

[155] Lara RF, Azcarate SM, Cantarelli MÁ, Orozco IM, Caroprese ME, Savio M, et al. Lubricant quality control: A chemometric approach to assess wear engine in heavy machines. Tribology International. 2015;86:36-41.

[156] Terhune JH, Gordon GM. Corrosive impurity sensor. Google Patents; 1986.

[157] Kondo K, Hattori T, Atsumi K, Nishida M. Machine oil deterioration detection. Google Patents; 1987.

[158] Cipris D, Palanisamy TG, Walsh AT. Lubricant oil monitoring system and method of monitoring lubricant oil quality. Google Patents; 1988.

[159] Yasutomi S, Maeda Y, Maeda T. Kinetic approach to engine oil. 1. Analysis of lubricant transport and degradation in engine system. Industrial & Engineering Chemistry Product Research and Development. 1981;20:530-6.

[160] Yasutomi S, Maeda Y, Maeda T. Kinetic approach to engine oil. 2. Antioxidant decay of lubricant in engine system. Industrial & Engineering Chemistry Product Research and Development. 1981;20:536-40.

[161] Yan XP, Zhao CH, Lu ZY, Zhou XC, Xiao HL. A study of information technology used in oil monitoring. Tribology International. 2005;38:879-86.

[162] Wu T, Wu H, Du Y, Kwok N, Peng Z. Imaged wear debris separation for on-line monitoring using gray level and integrated morphological features. Wear. 2014;316:19-29.

[163] Wu T, Peng Y, Wu H, Zhang X, Wang J. Full-life dynamic identification of wear state based on on-line wear debris image features. Mechanical Systems and Signal Processing. 2014;42:404-14.

[164] Feng S, Fan B, Mao J, Xie Y. Prediction on wear of a spur gearbox by on-line wear debris concentration monitoring. Wear. 2015;336:1-8.

[165] Peng Y, Wu T, Wang S, Peng Z. Oxidation wear monitoring based on the color extraction of on-line wear debris. Wear. 2015;332:1151-7.

[166] Peng Y, Wu T, Wang S, Peng Z. Wear state identification using dynamic features of wear debris for on-line purpose. Wear. 2017;376:1885-91.

[167] Fan B, Li B, Feng S, Mao J, Xie Y-B. Modeling and experimental investigations on the relationship between wear debris concentration and wear rate in lubrication systems. Tribology International. 2017;109:114-23.

[168] Yuan W, Dong G, Chin KS, Hua M. Tribological assessment of sliding pairs under damped harmonic excitation loading based on on-line monitoring methods. Tribology International. 2016;96:225-36.

[169] Gajewski J, Vališ D. The determination of combustion engine condition and reliability using oil analysis by MLP and RBF neural networks. Tribology International. 2017;115:557-72.

[170] Wang W, Hussin B. Plant residual time modelling based on observed variables in oil samples. Journal of the Operational Research Society. 2009;60:789-96.

[171] Lee J, Sung NW, Huh KY. Prediction of soot particle size distribution for turbulent reacting flow in a diesel engine. International Journal of Engine Research. 2011;12:181-9.

[172] Gong Y, Guan L, Feng X, Wang L, Yu X. In-situ lubricating oil condition sensing method based on two-channel and differential dielectric spectroscopy combined with supervised hierarchical clustering analysis. Chemometrics and Intelligent Laboratory Systems. 2016;158:155-64.

[173] Zhou J, Xiong Y, Gong Y, Liu X. Analysis of the oxidative degradation of biodiesel blends using FTIR, UV–Vis, TGA and TD-DES methods. Fuel. 2017;202:23-8.

[174] Ulrich C, Petersson H, Sundgren H, Björefors F, Krantz-Rülcker C. Simultaneous estimation of soot and diesel contamination in engine oil using electrochemical impedance spectroscopy. Sensors and Actuators B: Chemical. 2007;127:613-8.

[175] Kuhn AT. Corrosion of Co-Cr alloys in aqueous environments. Biomaterials. 1981;2:68-77.

[176] Assi F, Suter T, Böhni H. A new electrochemical technique to study tribocorrosion at the micrometric scale. Tribotest. 1999;6:17-28.

[177] Ponthiaux P, Wenger F, Drees D, Celis JP. Electrochemical techniques for studying tribocorrosion processes. Wear. 2004;256:459-68.

[178] Schwartz ES, Smolenski DJ, Keersmaekers JD, Traylor CM, Wallo GJ. Automatic engine oil change indicator system. Google Patents; 1989.

[179] Inoue R. Oil degradation warning system. Google Patents; 1989.

[180] Sawatari T, Nakamura M, Sugiura T. Automotive engine oil monitoring system. Google Patents; 1987.

[181] Imajo M, Kawakita T. Oil degradation warning system. Google Patents; 1989.

[182] Raffa JM, Cwik TT, Aronow MF, Little WA, Meitzler AH, Misangyi PW, et al. Engine oil monitoring system having an in-vehicle display of the current status of the oil. Google Patents; 1995.

[183] Alsenz RH. Oil monitoring system. Google Patents; 1997.

[184] Sarangapani J. Method for determining the condition of engine oil based on TBN modeling. Google Patents; 1999.

[185] Donald JEM, Schwartz ES, Hamparian N, Jacek M, Stempnik JM, Fletcher SJ. Oil life monitor for diesel engines. Google Patents; 2001.

[186] Khan ZA, Saeed A, Gregory O, Ghafoor A. Biodiesel Performance within Internal Combustion Engine Fuel System: A Review. Tribology in Industry. 2016;38:197-213.

[187] Fatima N, Minami I, Holmgren A, Marklund P, Larsson R. Surface chemistry of wet clutch influenced by water contamination in automatic transmission fluids. Tribology International. 2016;96:395-401.

[188] Zhao H, Morina A, Neville A, Vickerman R. Tribochemistry on Clutch Friction Material Lubricated by Automatic Transmission Fluids and the Link to Frictional Performance. Journal of Tribology. 2013;135:041801--11.

[189] Zhao H, Neville A, Morina A, Vickerman R, Durham J. Improved anti-shudder performance of ATFs—Influence of a new friction modifier and surface chemistry. Tribology International. 2012;46:62-72.

[190] Mertens WG, Zuzich F. Automatic transmission gear materials and associated problems. SAE International; 1956.

[191] Clark KS, Singh T, Buffa RP, Gayney JM, Cousins WL, Xie Z, et al. General Motors Front Wheel Drive Seven Speed Dry Dual Clutch Automatic Transmission. SAE Int J Engines. 2015;8:1379-90.

[192] Coronado JJ. Abrasive Size Effect on Friction Coefficient of AISI 1045 Steel and 6061-T6 Aluminium Alloy in Two-Body Abrasive Wear. Tribology Letters. 2015;60:40.

[193] Zhao X, Liu J, Zhu B, Luo Z, Miao H. Effects of lubricants on friction and wear of Ti(CN)1045 steel sliding pairs. Tribology International. 1997;30:177-82.

[194] Menezes PL, Ingole SP, Nosonovsky M, Kailas SV, Lovell MR. Tribology for scientists and engineers: Springer; 2013.

[195] Menezes PL, Kailas SV. Role of surface texture and roughness parameters on friction and transfer film formation when UHMWPE sliding against steel. Biosurface and Biotribology. 2016;2:1-10.

[196] Menezes PL, Kishore, Kailas SV. Effect of Roughness Parameter and Grinding Angle on Coefficient of Friction When Sliding of Al–Mg Alloy Over EN8 Steel. Journal of Tribology. 2006;128:697-704.

[197] Fabbro R, Fournier J, Ballard P, Devaux D, Virmont J. Physical study of laser-produced plasma in confined geometry. Journal of applied physics. 1990;68(2):775-84.

[198] Prabhakaran S, Kulkarni A, Vasanth G, Kalainathan S, Shukla P, Vasudevan VK. Laser shock peening without coating induced residual stress distribution, wettability characteristics and enhanced pitting corrosion resistance of austenitic stainless steel. Applied Surface Science. 2018;428:17-30.

[199] Trdan U, Porro JA, Ocaña JL, Grum J. Laser shock peening without absorbent coating (LSPwC) effect on 3D surface topography and mechanical properties of 6082-T651 Al alloy. Surface and Coatings Technology. 2012;208:109-16.

[200] Dai FZ, Geng J, Tan WS, Ren XD, Lu JZ, Huang S. Friction and wear on laser textured Ti6Al4V surface subjected to laser shock peening with contacting foil. Optics & Laser Technology. 2018;103:142-50.

[201] Hu T, Hu L, Ding Q. Effective solution for the tribological problems of Ti-6Al-4V: Combination of laser surface texturing and solid lubricant film. Surface and Coatings Technology. 2012;206:5060-6.

[202] Sánchez-Santana U, Rubio-González C, Gomez-Rosas G, Ocaña JL, Molpeceres C, Porro J, et al. Wear and friction of 6061-T6 aluminum alloy treated by laser shock processing. Wear. 2006;260:847-54.

[203] Kappes M, Iannuzzi M, Carranza RM. Pre-Exposure Embrittlement and Stress Corrosion Cracking of Magnesium Alloy AZ31B in Chloride Solutions. Corrosion. 2014;70:667-77.

[204] Jafari S, Harandi SE, Singh Raman RK. A Review of Stress-Corrosion Cracking and Corrosion Fatigue of Magnesium Alloys for Biodegradable Implant Applications. JOM. 2015;67:1143-53.

[205] Espallargas N, Johnsen R, Torres C, Muñoz AI. A new experimental technique for quantifying the galvanic coupling effects on stainless steel during tribocorrosion under equilibrium conditions. Wear. 2013;307:190-7.

[206] Williams G, Neil McMurray H. Localized Corrosion of Magnesium in Chloride-Containing Electrolyte Studied by a Scanning Vibrating Electrode Technique. Journal of The Electrochemical Society. 2008;155:C340-C9.

[207] McNulty RE, Hanawalt JD. Some corrosion characteristics of high purity magnesium alloys. Transactions of The Electrochemical Society. 1942;81:423-33.

[208] Song W, Martin HJ, Hicks A, Seely D, Walton CA, Lawrimore Ii WB, et al. Corrosion behaviour of extruded AM30 magnesium alloy under salt-spray and immersion environments. Corrosion Science. 2014;78:353-68.

[209] Curioni M. The behaviour of magnesium during free corrosion and potentiodynamic polarization investigated by real-time hydrogen measurement and optical imaging. Electrochimica Acta. 2014;120:284-92.

[210] Cano ZP, Kish JR, McDermid JR. On the Evolution of Cathodic Activity during Corrosion of Magnesium Alloy AZ31B in a Dilute NaCl Solution. Journal of The Electrochemical Society. 2016;163:C62-C8.

[211] Cano ZP, Danaie M, Kish JR, McDermid JR, Botton GA, Williams G. Physical characterization of cathodically-activated corrosion filaments on magnesium alloy AZ31B. Corrosion. 2014;71:146-59.

[212] Samaniego A, Llorente I, Feliu Jr S. Combined effect of composition and surface condition on corrosion behaviour of magnesium alloys AZ31 and AZ61. Corrosion Science. 2013;68:66-71.

[213] Mischler S. Triboelectrochemical techniques and interpretation methods in tribocorrosion: A comparative evaluation. Tribology International. 2008;41:573-83.

[214] Cao S, Guadalupe Maldonado S, Mischler S. Tribocorrosion of passive metals in the mixed lubrication regime: theoretical model and application to metal-on-metal artificial hip joints. Wear. 2015;324-325:55-63.

[215] Zhang Y, You J, Lu J, Cui C, Jiang Y, Ren X. Effects of laser shock processing on stress corrosion cracking susceptibility of AZ31B magnesium alloy. Surface and Coatings Technology. 2010;204:3947-53.

[216] Qiao H, Zhao J, Gao Y. Experimental investigation of laser peening on TiAl alloy microstructure and properties. Chinese Journal of Aeronautics. 2015;28:609-16.

[217] Rapp BE. Chapter 22 - Measuring Surface Tension and Free Surface Energy. In: Rapp BE, editor. Microfluidics: Modelling, Mechanics and Mathematics. Oxford: Elsevier; 2017. p. 453-65.

[218] Bargir S, Dunn S, Jefferson B, Macadam J, Parsons S. The use of contact angle measurements to estimate the adhesion propensity of calcium carbonate to solid substrates in water. Applied Surface Science. 2009;255:4873-9.

[219] Wenzel RN. Resistance of solid surfaces to wetting by water. Industrial & Engineering Chemistry. 1936;28:988-94.

[220] Wenzel RN. Surface Roughness and Contact Angle. The Journal of Physical and Colloid Chemistry. 1949;53:1466-7.

[221] Prince M, Thanu AJ, Gopalakrishnan P. Improvement in wear and corrosion resistance of AISI 1020 steel by high velocity oxy-fuel spray coating containing Ni-Cr-B-Si-Fe-C. High Temperature Materials and Processes. 2012; p. 149.

[222] Jabbar A, Yasin G, Khan WQ, Anwar MY, Korai RM, Nizam MN, et al. Electrochemical deposition of nickel graphene composite coatings: effect of deposition temperature on its surface morphology and corrosion resistance. RSC Advances. 2017;7:31100-9.

[223] Aneja KS, Böhm HLM, Khanna AS, Böhm S. Functionalised graphene as a barrier against corrosion. FlatChem. 2017;1:11-9.

[224] Kalin M, Vižintin J, Novak S, Dražič G. Wear mechanisms in oil-lubricated and dry fretting of silicon nitride against bearing steel contacts. Wear. 1997;210:27-38.

[225] Pimenta MA, Dresselhaus G, Dresselhaus MS, Cançado LG, Jorio A, Saito R. Studying disorder in graphite-based systems by Raman spectroscopy. Physical Chemistry Chemical Physics. 2007;9:1276-90.

[226] Ferrari AC, Meyer JC, Scardaci V, Casiraghi C, Lazzeri M, Mauri F, et al. Raman Spectrum of Graphene and Graphene Layers. Physical Review Letters. 2006;97:187401.

[227] Gupta A, Chen G, Joshi P, Tadigadapa S, Eklund. Raman Scattering from High-Frequency Phonons in Supported n-Graphene Layer Films. Nano Letters. 2006;6:2667-73.

[228] Childres I, Jauregui LA, Park W, Cao H, Chen YP. Raman spectroscopy of graphene and related materials. New developments in photon and materials research. 2013;1.

[229] Yu Q, Jauregui LA, Wu W, Colby R, Tian J, Su Z, et al. Control and characterization of individual grains and grain boundaries in graphene grown by chemical vapour deposition. Nature materials. 2011;10:443.

[230] Kong ANG, Gong B-K, Wang G, Cui H-W. Influence of surface roughness of substrate on the properties of Ni–Co–Fe electrodeposition coating on copper. Surface Review and Letters. 2017;25:1850120.

[231] Nazir MH, Khan Z. Maximising the interfacial toughness of thin coatings and substrate through optimisation of defined parameters. International Journal of Computational Methods and Experimental Measurements. 2015;3:316-28.

[232] Fowkes FM. Attractive forces at interfaces. Industrial & Engineering Chemistry. 1964;56:40-52.

[233] Busscher HJ, Van Pelt AWJ, De Boer P, De Jong HP, Arends J. The effect of surface roughening of polymers on measured contact angles of liquids. Colloids and Surfaces. 1984;9:319-31.

[234] Lin J, Wang L, Chen G. Modification of Graphene Platelets and their Tribological Properties as a Lubricant Additive. Tribology Letters. 2011;41:209-15.

[235] Shin YJ, Wang Y, Huang H, Kalon G, Wee ATS, Shen Z, et al. Surface-Energy Engineering of Graphene. Langmuir. 2010;26:3798-802.

[236] French RH. Origins and applications of London dispersion forces and Hamaker constants in ceramics. Journal of the American Ceramic Society. 2000;83:2117-46.

[237] Puttock MJ, Thwaite EG. Elastic compression of spheres and cylinders at point and line contact. In: Puttock MJ, Thwaite EG, (Australia) NSL, editors. Elastic compression of spheres and cylinders at point and line contact. Commonwealth Scientific and Industrial Research Organization, Melbourne: Commonwealth Scientific and Industrial Research Organization; 1969. p. 64, p11.

[238] Hurricks PL. The mechanism of fretting — A review. Wear. 1970;15:389-409.

[239] Siddaiah A, Kasar KA, Khosla V, Menezes LP. In-Situ Fretting Wear Analysis of Electrical Connectors for Real System Applications. Journal of Manufacturing and Materials Processing. 2019;3.

[240] Reeves CJ, Menezes PL, Lovell MR, Jen T-C. The Size Effect of Boron Nitride Particles on the Tribological Performance of Biolubricants for Energy Conservation and Sustainability. Tribology Letters. 2013;51:437-52.

[241] Menezes PL, Ingole SP, Nosonovsky M, Kailas SV, Lovell MR. Tribology for scientists and engineers. Tribology for scientists and engineers: Springer; 2013. p. 9-28.